MIT/WHOI

Massachusetts Institute of Technology
Woods Hole Oceanographic Institution

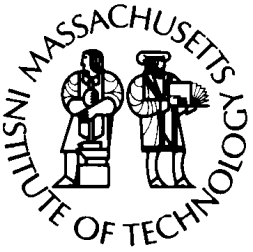

Joint Program in Oceanography/ Applied Ocean Science and Engineering

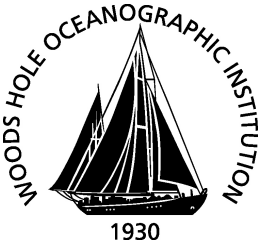

DOCTORAL DISSERTATION

Lagrangian dispersion and deformation in submesoscale flows

by

Sebastian Essink

June 2019

Lagrangian Dispersion and Deformation in Submesoscale Flows

by

Sebastian Essink

B.Sc., University of Hamburg (2012)

Submitted to the Joint Program in Oceanography/Applied Ocean Science & Engineering in partial fulfillment of the requirements for the degree of

Doctor of Philosophy

at the

MASSACHUSETTS INSTITUTE OF TECHNOLOGY

and the

WOODS HOLE OCEANOGRAPHIC INSTITUTION

June 2019

Author .....
Joint Program in Oceanography/Applied Ocean Science & Engineering
Massachusetts Institute of Technology
& Woods Hole Oceanographic Institution
April 25, 2019

Certified by .....
Dr. Amala Mahadevan
Senior Scientist
Woods Hole Oceanographic Institution
Thesis Supervisor

Accepted by ....
Prof. Glenn Flierl
Chairman, Joint Committee for Physical Oceanography
Massachusetts Institute of Technology
Woods Hole Oceanographic Institution

Lagrangian Dispersion and Deformation in Submesoscale Flows

by

Sebastian Essink

Submitted on April 25, 2019 to the Joint Program in Oceanography/Applied Ocean Science & Engineering, Massachusetts Institute of Technology & Woods Hole Oceanographic Institution in partial fulfillment of the requirements for the degree of Doctor of Philosophy

Abstract

Submesoscale currents, with horizontal length scales of 1-20 km, are an important element of upper ocean dynamics. These currents play a crucial role in the horizontal and vertical redistribution of tracers, the cascade of tracer variance to smaller scales, and in linking the mesoscale circulation with the dissipative scales. This thesis investigates submesoscale flows and their properties using Lagrangian trajectories of observed and modeled drifters.

We analyze statistics of observed drifter pairs to characterize turbulent dispersion at submeso-scales. Contrary to theoretical expectations, we find that nonlocal velocity gradients associated with mesoscale eddies dominate the separation of drifters even at the kilometer scale. At submeso-scales, we observe energetic motions, such as near-inertial oscillations, that contribute to the energy spectrum but are inefficient at dispersion.

Using trajectories in a model of submesoscale turbulence, we find that, if drifters have a vertical separation, vertical shear dominates the dispersion and conceals horizontal dispersion regimes from drifter observations. Particularly in submesoscale flows, vertical shear is orders of magnitude larger than horizontal gradients in velocity. Since conventional drifters in the ocean are not affected by vertical shear, it is likely that drifter-derived diffusivity underestimates the diffusivity that a tracer would experience.

Lastly, we test and apply cluster-based methods, using three or more drifters, to estimate the velocity gradient tensor. Since velocity gradients become large at submesoscales, the divergence, strain, and vorticity control the evolution and deformation of clusters of drifters. Observing the velocity gradients using drifters, enables us to further constrain the governing dynamics and decipher submesoscale motions from inertia-gravity waves.

These insights provide a Lagrangian perspective on submesoscale flows that illuminates scales that are challenging to observe from other platforms. We reveal observational and theoretical challenges that need to be overcome in future investigations.

Thesis Supervisor: Dr. Amala Mahadevan
Title: Senior Scientist
Woods Hole Oceanographic Institution

Acknowledgments

I owe my sincere gratitude to my advisor, Amala Mahadevan, who took me on as a guest student and has supported me ever since. I learned how to be a scientist and a better person from Amala and thank her for all her trust and patience. It was a privilege to be part of her group and I simply would not be here if it was not for her.

I thank my committee, Melissa Omand, Mick Follows, Karl Helfrich, and Joe LaCasce for fruitful discussions, support, and guidance to finish my thesis. I also thank Irina Rypina for valuable discussions and for chairing my defense.

I am thankful that I was part of the Mahadevan Lab (including Cheetah) where we shared a lot of curiosity and learned a lot from each other. Most importantly, though, I have found many friends in this group and will miss our group meetings, dinners, and cruises.

Thanks to my fellow students and postdocs at WHOI and MIT. I very was fortunate to have a great cohort around me and, in particular, want to thank my PO classmates, Gualtiero, Sam, Julie, and Bryce for being great friends and companions.

I am thankful for my friends in Woods Hole and Cambridge who have made me feel at home. And finally, I owe endless gratitude to my friends at home, my parents, and my brother, who have always been there for me, even if not physically, and supported me unconditionally.

My doctoral studies in the WHOI/MIT Joint Program were funded by the National Science Foundation (OCE-I434788) and the Office of Naval Research (N00014-13-1-0451, Grant N00014-16-1-2470).

CONTENTS

LIST OF FIGURES

LIST OF TABLES

Chapter 1

INTRODUCTION

The transport and dispersion of properties in the ocean have been of great interest in physical oceanography for decades (e.g., Richardson and Stommel, 1948). On a global scale, the ocean currents transport heat and salt as part of the meridional overturning circulation, whereas, on regional and small scales, oceanic currents are responsible for the dispersion of pollutants (e.g., Rypina et al., 2013; Poje et al., 2014), organisms (e.g., Rypina et al., 2014b; Pineda et al., 2007), nutrients and carbon. The trajectories of fluid parcels, therefore, contain valuable information about the flow field and help to understand the environmental and socio-economic impact.

Transport problems are most naturally approached in the Lagrangian framework by observing properties of the ocean following fluid parcels, rather than measuring them at a fixed point in space. This approach has the advantage that Lagrangian observations not only provide the instantaneous properties at one time and location, but also encapsulate the fluid parcel's history (Bennett, 2006). Dispersion problems, such as the dispersal of a larvae away from a spawning region, can therefore be addressed by studying the evolution of trajectories over time. These trajectories map out the circulation and inform about the fate of the larvae. In a turbulent fluid like the ocean, however, trajectories and their fate depend dramatically on the initial condition, so that, in practice, ensemble averages over many trajectories are needed to represent the flow field with statistical significance.

Unlike individual trajectories, pairs of synchronous trajectories hold information about the motion relative to the center of mass. The spreading of a continuous tracer about the center of mass is equivalent to pair dispersion (Batchelor, 1953; LaCasce, 2008). Turbulent flows have the property of quickly separating neighboring fluid parcels - this concept has been characterized for decades by a relative diffusivity with which pairs of particles spread around their center of mass. Relative diffusivity relates to the average rate of change of squared separation, the relative dispersion, and, therefore, describe how a patch of pollutant grows with time.

In a turbulent flow with a given kinetic energy spectrum $E \sim k^{-\alpha}$, relative dispersion and relative diffusivity can be theoretically predicted. In general, relative dispersion is either local, for $1 < \alpha < 3$, or nonlocal, for $\alpha \geq 3$. The characteristic difference between the two dispersion regimes is the size of the eddies relative to the separation of particle pairs. Local dispersion is then the increase in relative dispersion by eddies that are of similar size as the separation itself. Nonlocal dispersion, however, is the increase in relative dispersion by eddies much larger than the separation. For a dynamical typical model of the ocean, e.g., the quasi-geostrophic turbulence (Charney, 1971), this means that nonlocal

dispersion is expected below the deformation radius, $L_D = NH/f$, where $\alpha = 3$, and local dispersion above the deformation radius, where $\alpha = 5/3$, given that there is an inverse energy cascade.

At scales where the energy spectrum is unresolved by satellite observations and difficult to observed from other platforms, for example at scales of $\mathcal{O}(1 - 20\ km)$, pair dispersion has been used to infer the dominate dynamics. At these scales, it has been postulated that the energy spectrum flattens, e.g., to $\alpha = 5/3$ in surface quasi-geostrophy (QG; Blumen, 1978), to $\alpha = 2$ in frontogenetic flows (Hoskins and Bretherton, 1972) or becomes dominated by the internal wave spectrum (Garrett and Munk, 1972), before energy eventually reaches the viscous, dissipative scales. For pair dispersion, this flattening is equivalent to a local dispersion regime. However, pair dispersion observation have been unsuccessful in observing this regime. Observations in the Gulf of Mexico using near-surface drifter observations describe a local regime at the submeso-scale (Poje et al., 2014, 2017), however, it is possibly reflecting near-inertial energy.

How the energy spectrum behaves at these scales is still focus of active research; recent work has shown that the answer varies strongly in time and space (e.g., Callies et al., 2015). Additionally, if the energy spectra whitens below the deformation radius, it is unclear to what extent the steep spectra in the mesoscale range, at which theory predicts nonlocal dispersion, affect pairs at the smallest scales. Chapter 2 of this dissertation characterizes turbulent dispersion at scales from 1 to 100 km and tests the hypothesis of whitening energy spectra using a drifter data collected in the Bay of Bengal.

One of the dynamical frameworks for flat spectra at submesoscale is frontogenesis (Hoskins and Bretherton, 1972; Stone, 1966), the intensification of lateral buoyancy gradients and acceleration of geostrophic flow. In the presence of a surface boundary, the acceleration of the geostrophic flow can not be balance by a three-dimensional ageostrophic circulation, such that the front keeps intensifying. Since buoyancy gradients are strongest at the surface, using thermal wind, the strongest shear will also be near the surface. The surface energy spectra with $\alpha = 2$ is constant across the mixed layer (ML), where buoyancy gradients are uniform and decays exponentially below if stratification is constant. For realistic stratificuation, velocities decays faster than exponential below the mixed layer (LaCasce, 2012). Similarly, in surface QG (Blumen, 1978; Held et al., 1995), potential vorticity (PV) anomalies are formed by gradients in surface buoyancy. These surface PV anomalies are the forcing terms for the three-dimensional velocity field. In surface QG, the PV anomalies decay faster than exponentially with depth away from the surface (LaCasce

and Wang, 2015), generating a flow that is surface intensified as well.

Submesoscale flows like those described above possess a surface-intensified vertical structure, often homogeneous across the ML, and decaying exponentially below (Klein et al., 2008). Since submesoscale flows draw their energy from buoyancy fronts, they develop narrow jets that are further intensified by frontogenesis. Fully developed submesoscale turbulence is then typically associated with sharp gradients in surface properties, filaments, fronts, and eddies. Since the vertical shear S scales with the lateral buoyancy gradients, $M^2 = |b_z|$, it becomes extremely large at these submesoscale features, reaching $\mathcal{O}(100f)$. For comparison, lateral velocity gradients, such as the lateral strain and shear, that scale with the Rossby number R_0 are $\mathcal{O}(f)$ at submesoscale fronts.

Turbulent dispersion at submesoscale is therefore not only expected to change character as the kinetic energy spectrum changes with depth (Scott, 2006), but it will also be affected by the strong vertical shear in the horizontal velocity itself. Although drifters drogued at a fixed depth do not separate vertically, it has been shown in numerous dye experiments that the vertical shear plays an essential role in the dispersion of tracers (e.g., Steinbuck et al., 2011). Chapter 3 of this thesis investigates the importance of vertical shear for the horizontal dispersion, relative to the lateral velocity gradients that drive horizontal turbulent dispersion. In particular, this chapter uses depth-keeping numerical drifters deployed at different depth and investigates the markedly different character of dispersion if drifter pairs have a vertical separation.

To describe the evolution of a fluid parcel in the ocean, pair statistics are not sufficient as they are not able to capture the rotation and deformation imparted by the velocity field. From drifter and dye experiments in the ocean (e.g., D'Asaro et al., 2018), we know that initially homogeneously distributed patches of tracer are stretched and elongated rapidly by the currents and result in a soup filaments and eddies. While the streching into filaments is consistent with non-local disperison, which can be identified from pair dispersion, what is missed by two-dimensional tracers is the vertical motion which occurs in covergences.

At submesoscales, the velocity gradients become significantly larger, such that the vertical component of the relative vorticity, $\zeta = \hat{k}\nabla \times \mathbf{u} = v_x - u_y$, the lateral strain $\gamma = \sqrt{(u_x - v_y)^2 + (v_x + u_y)^2}$, comprised of shearing and normal strain, and the horizontal divergence, $\delta = \nabla \mathbf{u} = u_x + v_y$, become $\mathcal{O}(f)$. These terms are all responsible for the deformation of fluid parcels and help to further constrain their evolution in the two-dimensional velocity field.

Chapter 4 is aiming to develop and assess the tools to estimate velocity gradients from Lagrangian observations. Since submesoscale occupy narrow regions and evolve fast, estimates of velocity gradients at the smallest scales are sparse. Shipboard measurements only measure the velocity along-track, such that only one component of the velocity gradients can be computed.

This dissertation is devoted to advance our understanding of the evolution fluid parcels subject to the continuum of oceanic velocities. We focus specially on the submesoscale range, in which vertical shear and horizontal deformations becomes large and, therefore, play an important role for the dispersion and deformations.

1.1 Submesoscale dynamics

Submesoscale motions occupy the range of scales of $\mathcal{O}(1-20\ km)$ that bridges the well-described mesoscale circulation, the continuum of inertial-gravity waves and the three-dimensional turbulence. Although ubiquitous in the ocean, generated in the surface and bottom boundary layers as well as by topographic wakes, submesoscale turbulence has only been studied as a distinct set of dynamics for the last few decades. With the ascent of improved satellite technology, faster *in-situ* sampling, autonomous vehicles, as well as high-resolution radar, however, submesoscale currents have been observed in many regions of the ocean.

With horizontal length scales L of $\mathcal{O}$(1 km), vertical scales of $\mathcal{O}$(10 m), and time scales $\mathcal{O}$(hours - days), submesoscale flows are challenging to observe with contemporary technology. Ships and gliders are generally too slow and provide two-dimensional measurements and satellites are too coarse. Further complicating is the fact that submesoscale flows share the same spatio-temporal band with processes like tides, near-inertial waves, and Langmuir turbulence. The submesoscale signal can, thus, often be concealed, especially when measured from stationary Eulerian platforms. Dynamically, submesoscale dynamics emerge where the influence of stratification and rotation begins to wane. Submesoscale fronts and eddies are often associated with Rossby numbers R_0 of order one, expressing the deviation from geostrophically-controlled flow. Likewise, Froude numbers $Fr = S/N$, where $S = \partial \mathbf{u}/\partial z$ is the vertical shear, are not asymptotically small, such that submesoscales can be characterized by order one Burger numbers $Bu = (R_0/Fr)^2$.

Due to their impact on stratification and vertical transport, submesoscale currents are particularly interesting for the vertical structure of the upper ocean. Frontogenesis, eddies,

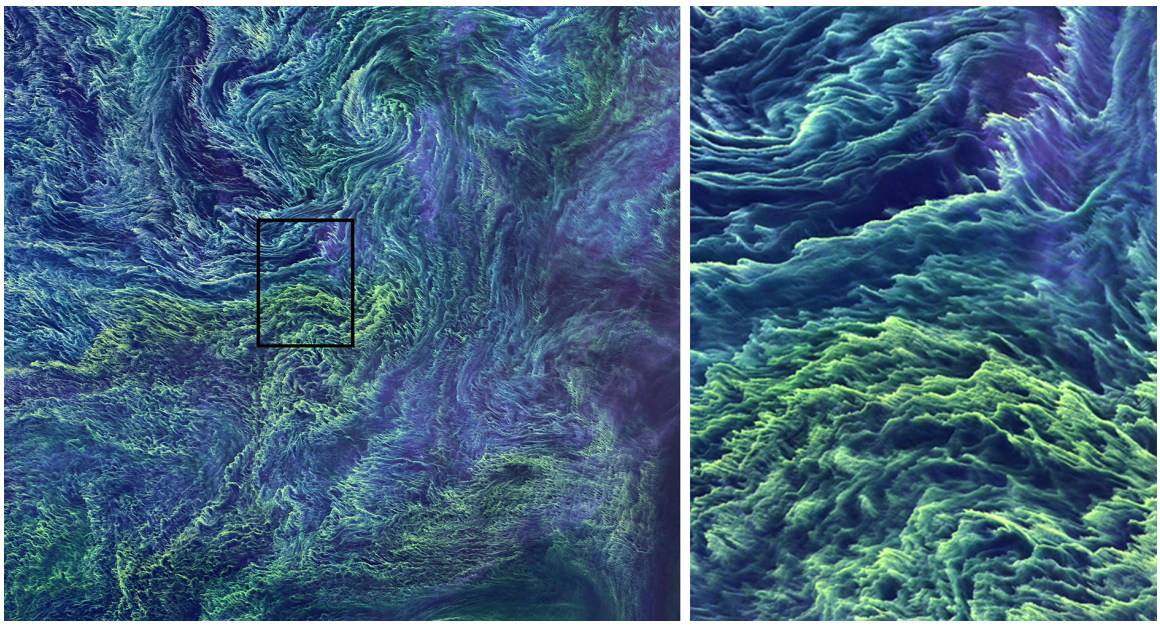

Figure 1-1: False-color image recorded by the Operational Land Imager on Landsat 8 capturing a cyanobacteria bloom in the Baltic Sea on August 11, 2015. Left panel shows a 100 km wide region, right panel is zoomed in onto the black rectangle, which is 10 km wide. Swirling, elongated structures in cyanobacteria span an enormous range of scales, smallest features are a few hundred meters wide.

and ageostrophic motions can generate vertical velocity that is much larger than associated with mesoscale eddies, facilitating a communication of the mixed layer with the pycnocline. Furthermore, submesoscale eddies that are generated by baroclinic instability of buoyancy fronts, have the tendency to slump over isopycnals and, thus, restratify the water column. Vertical fluxes and restratification have particularly important consequences for biological productivity since nutrients, which are abundant at depth, are fluxed into the euphotic zone, as well as for the export of organic carbon out of the surface ocean into the interior.

In satellite imagery of chlorophyll and temperature, however, it was their rich horizontal structure that propelled submesoscales into scientific focus. Submesoscale turbulence is characterized by a soup of sharp gradients in properties, often linearly elongated in to filaments and fronts, and convergent regions that generate sharp edges and changes in water mass properties over only a few tens of meters (Figure 1-1).

The patterns in ocean color reveal variability at scales smaller than 10 km. While currents at these scales, the submesoscales, play an important role in stirring chlorophyll, there are a range of biological and physical processes that contribute to create this distribution. Interestingly, biological time scales, e.g., the doubling time of plankton ($\mathcal{O}$(1 day)), are similar to the submesoscale time scales with $\mathcal{O}$(1h–days). It is therefore conceivalbe

that physical and biological process ineract at submesoscales.

Furthermore, horizontal convergences can be identified by sharp edges in the chlorophyll concentration that could not be generated by horizontal mixing. Those are indicative of a three-dimensional circulation and a departure from geostrophic dynamics that are thought to occur at submesoscales. The image also suggests that surface wind and surface waves play a role and creating structure below 1 km. Parallel streaks can be found that have been created by wind blowing out of the same direction.

1.2 Lagrangian observations

Lagrangian instruments can be categorized into floats and drifters (e.g., LaCasce, 2008; Davis, 1991). Floats sink to a target density (or depth) and follow it. Isopycnal floats have the ability to change their buoyancy to follow water of fixed density and are therefore closer to truly Lagrangian. Drifters have surface buoys and a subsurface drogue that dictates them to follow the water at a fixed depth. Since constant-depth floats or drifters will generally not track isopycnals and, therefore, not conserve water properties along their trajectories.

Lagrangian observations have a long history that dates back to the time well before acoustic tracking and GPS technology was available. Vegetables, dye, wood, smoke, and other current followers have been improvised to map the path of fluid or air parcels, to understand the diffusivity of the ocean and atmosphere, and to infer the energy spectrum from the dispersion of materials. Swallow (1971) was pioneer to use acoustically tracked floats that could provide continuous time estimates of their position. The advent of satellite-tracked drifters and floats revolutionized the way we think about the ocean. It enabled us to map the currents where ships cannot measure and operate in a highly economical way.

In the past decades, Lagrangian observations gain new attention because it is possible to sample sub-kilometer ranges with 5-minute temporal resolution that are otherwise impossible to observe. High-resolution drifter observations enable us to estimate the energy spectrum at scales, that even high resolution shipboard measurements cannot match. Drifter release strategies allow us to study pairs that are initially close, oftentimes less than 100 m, and track how they separate over periods of days to weeks.

Recently, since drifters become more readily available, large numbers of drifters were deployed in the same regions, allowing for studies that involve multiple drifters at a

time (Poje et al., 2014). Cluster experiments like these give information about the two-dimensional structure of the velocity field, and the relative deformation of swarms of drifters by the velocity. By using more than three drifters, it is theoretically possible to estimate the two-dimensional velocity gradient tensor.

In this thesis, Surface Velocity Program (SVP) drifter data is used that was collected in the Bay of Bengal. The SVP drifters have a surface buoy just beneath which a thermistor and conductivity probe is located and are drogued at 15 m depth (Figure 1-2). Temperature and salinity measurements are therefore not necessarily sampling the same water mass as the drogue.

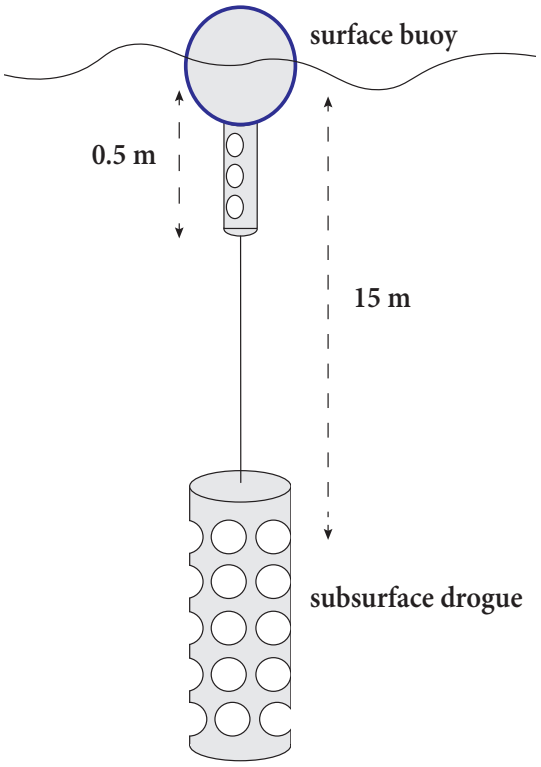

Figure 1-2: Schematic of SVP drifters used used in this thesis. Thermistor and conductivity probe are located in below the buoy.

Lagrangian analysis, simulating drifters in a numerical or satellite-derived flow field, has gained much attention (van Sebille et al., 2018). It allows detailed studies of the sensitivity to parameters like the initial conditions, pair separations, and small-scale parameterization. As characteristic for turbulence, individual trajectories are highly sensitive to the initial condition, so that observations in the ocean are often biased by the choice of location and deployment strategy. These obstacles can be overcome in numerical models to gain a statistically robust description of the Lagragian properties.

1.3 Bay of Bengal

In this dissertation, we use data that was collected during an extensive survey of the northern Bay of Bengal that was part of the Air-Sea Interaction Regional Initiative (ASIRI) funded by the Office of Naval Research. With the goal of understanding upper ocean dynamics in the context of the monsoon, ASIRI entails a series of scientific cruises to sample the upper ocean hydrography, velocity field, and turbulence in high spatial and

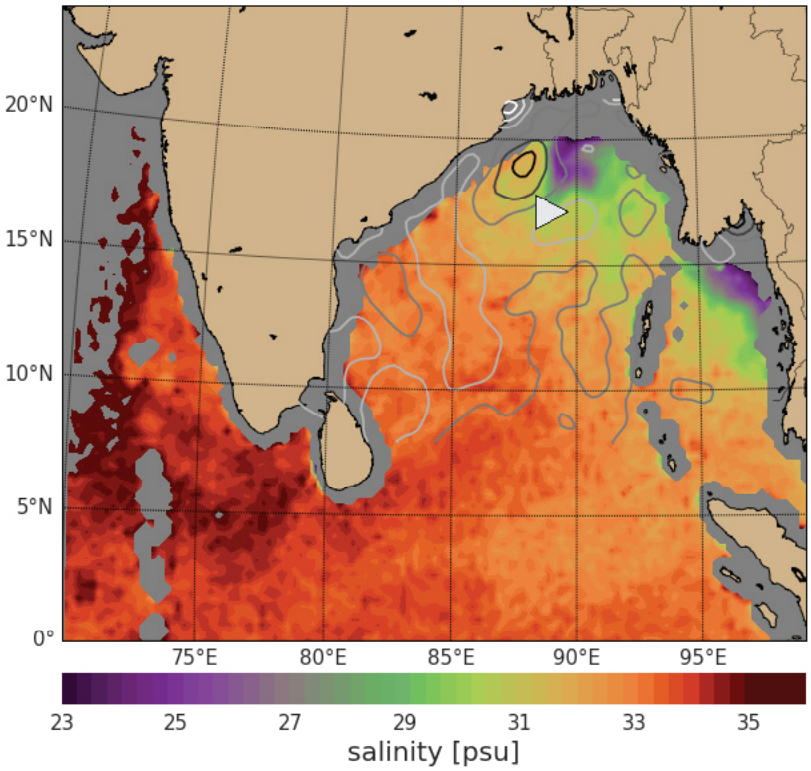

Figure 1-3: Snapshot of Sea Surface Salinity (SSS) measured by the Soil Moisture Active-Passive (SMAP) satellite mission in the Bay of Bengal on August 15, 2015. Freshwater enters the Bay of Bengal coming from the major river Ganges and Bhramaputra in the north and Iriwady in the east. Contours show the Sea Level Anomaly (SLA) from AVISO.

temporal resolution and to combine it with meteorological observation.

The Bay of Bengal is located in the northern Indian ocean neighboring the most densely populated countries on the planet (Figure 1-3). It is strongly affected by monsoonal rainfall and river runoff, receiving enormous quantities of freshwater in the monsoon season (July to September) that act like a buoyant, insulating cap on the water column. The mixed layer is shallow in the north of the bay (<10 m) overlaying a strong pycnocline that isolates the ventilated layers from the interior. An oxygen minimum zone is evidence for the slow communication of the surface layer with the water masses below.

Special focus within ASIRI was cast on lateral density fronts that were generated by the north-south salinity gradient and stirred into sharp gradients by the mesoscale circulation. Those buoyancy gradients are intensified by frontogenesis and host a range of submesoscale instabilities, such as baroclinic instability and symmetric instabilities, that are thought to occur in regions of freshwater-controlled density fronts. Submesoscale turbulence is a candidate that provides a mechanism for freshwater to be dispersed laterally

and for freshwater variance to be stirred towards smaller scales, where it can ultimately be mixed. Furthermore, submesoscale processes are candidates for modulating the sea surface temperature, which is the most important oceanic parameter controlling air-sea fluxes.

1.4 Thesis outline

This thesis utilizes drifter observations, numerical simulations, and theory to better understand the evolution of parcels of fluid in submesoscale turbulence and to use Lagrangian data and tools to better constrain Lagrangian properties of submesoscale flows.

- In Chapter 2, observed pairs of drifters are used to characterize the turbulent dispersion in the Bay of Bengal. With a focus on the submesoscale range of motions, we compare the pair dispersion regimes to theoretical expectations and to simulated drifters advected by satellite-derived, geostrophic currents.
- In Chapter 3, a numerical simulation and Lagrangian particle tracking is used to understand the impact of vertical shear on the horizontal dispersion.
- In Chapter 4, we use clusters of drifters (N>3) to evaluate methods to estimate the velocity gradient and related kinematic properties such as the vertical vorticity, divergence, and lateral strain. We use numerical simulations to study the sensitivity of estimates to cluster geometry and then apply the method to drifter data.

I summarize in Chapter 5, detailing the major conclusions of this dissertation and their implications for Lagrangian observations of submesoscale flows.

Chapter 2

CAN WE DETECT SUBMESOSCALE MOTIONS IN DRIFTER PAIR DISPERSION?

Abstract

A cluster of 45 drifters deployed in the Bay of Bengal is tracked for a period of 4 months. Pair dispersion statistics, from observed drifter trajectories and simulated trajectories based on surface geostrophic velocity, are analyzed as a function of drifter separation and time. Pair dispersion suggests non-local dynamics at submeso-scales of 1-20 km, likely controlled by the energetic mesoscale eddies present during the observations. Second-order velocity structure functions and their Helmholtz decomposition, however, suggest local dispersion and divergent horizontal flow at scales below 5 km. This inconsistency cannot be explained by inertial oscillations alone, as has been reported in recent studies, and is likely related to other non-dispersive processes that impact structure functions but do not enter pair dispersion statistics. At scales comparable to the deformation radius L_D, which is approximately 60 km, we find dynamics in agreement with Richardson's law and observe local dispersion in both the pair dispersion statistics and the analysis of second order velocity structure functions.

This chapter is in revision for the Journal of Physical Oceanography with co-authors V Hormann, LH Centurioni, and A Mahadevan. SE performed the research and wrote the manuscript under the supervision of AM. VH and LC planned and collected the drifter dataset.

2.1 Introduction

A better understanding of the Lagrangian transport of tracers, energy, and enstrophy in the ocean is relevant to a wide range of problems. It helps describe, for example, how pollutants (e.g., Rypina et al., 2013; Poje et al., 2014), freshwater (e.g., Mahadevan, 2016) or biological organisms (e.g., Rypina et al., 2014b) disperse, and how energy and enstrophy cascade across scales. The two-dimensional Lagrangian statistics of the near-surface oceanic flow and its associated transport can be explored using pairs of drifters, which float at the surface while being advected by the flow a few meters below.

In a turbulent ocean, the separation of pairs of drifters can theoretically be predicted when the kinetic energy spectrum is known (LaCasce, 2008, 2016) and, furthermore, depends on the separation distance r. On scales above about 100 m, the vertical velocity makes a negligible contribution to the kinetic energy, which is dominated by the horizontal velocity. The horizontal pair dispersion, defined as the mean square separation of pairs of drifters, describes how a group of drifters disperses around its center of mass. If energy spectra are steep, like the $E \sim k^{-3}$ observed in the enstrophy-cascading range of two-dimensional turbulence (Charney, 1971; Nastrom et al., 1986), where the horizontal wavenumber is defined as $k = (k_x^2 + k_y^2)^{1/2}$, the pair dispersion is dominated by the largest eddy in that range and termed *non-local* (Bennett, 1984). If energy spectra are flatter, like the $E \sim k^{-5/3}$ observed in the energy-cascading ranges of two-dimensional and three-dimensional turbulence (Charney, 1971; Kraichnan, 1967), the pair dispersion is dominated by eddies with length scales similar to the pair separation distance and termed *local* (Bennett, 1984; Richardson, 1926).

In the presence of two inertial spectral ranges, pairs of drifters transition from one dispersion regime to another as their separation distances grow (LaCasce, 2008). As an illustration, consider a two-dimensional, quasi-geostrophic model often used to represent mesoscale dynamics in the ocean. At small separations, initially, in the enstrophy-cascading range, drifters disperse non-locally until they reach the scale at which energy is injected (often through baroclinic instability at the first baroclinic deformation radius L_D, which we estimate as 60 km for our observations (Chelton et al., 1998)). Subsequently, in the energy-cascading range, they disperse locally. Unlike in the atmosphere (Nastrom et al., 1986; Er-El and Peskin, 1981), the kinetic energy spectrum in the ocean and its inertial ranges are not well documented. Sub-deformation scale dynamics are not thoroughly understood, are often dominated by ageostrophic, divergent motions (Bühler et al., 2014;

Callies and Ferrari, 2013; D'Asaro et al., 2018), and vary significantly in time and space (Callies et al., 2015).

At submeso-scales, considered as length scales of 0.1–20 km in our observations, a transition from non-local to local dispersion is likely to occur: The two-dimensional, quasi-geostrophic flow, with energy spectra of $E \sim k^{-3}$ intensifies at surface fronts and breaks down into smaller eddies and filaments, with energy spectra of $E \sim k^{-2}$ or $E \sim k^{-5/3}$. In this range, energetic eddies and filaments are reported in observations (Shcherbina et al., 2013; Gon et al., 2018), as well as in numerical simulations (Thomas et al., 2008), which are likely energized by surface frontogenesis (Lapeyre and Klein, 2006b; Hoskins, 1982; Stone, 1966) and mixed layer baroclinic instabilities (Boccaletti et al., 2007; Fox-Kemper et al., 2008). Conceptually, in regions where submesoscale flows and fronts are energetic, pair dispersion is expected to be local and then transitions to a non-local regime at larger scales in the enstrophy-cascading range of two-dimensional turbulence. Studying the dispersion at submesoscales is complicated, however, by the multitude of processes that reign the same spatiotemporal band. A careful characterization is thus needed to discern them among inertial oscillations, tides, Langmuir turbulence, and the mesoscale circulation.

The Bay of Bengal, the location of this study (Figure 2-1), hosts energetic submesoscale dynamics which are evident in observations (e.g., Ramachandran et al., 2018) and in numerical simulations (e.g., Sarkar et al., 2016). These likely occur at freshwater-dominated density fronts, which are generated by massive seasonal freshwater fluxes, mainly from major rivers in the north, and intense precipitation during the southwest monsoon. The shallow freshwater cap affects the evolution of the sea-surface temperature (SST) (Jaeger and Mahadevan, 2018) and the upper ocean's heat content (Shroyer et al., 2016; Mahadevan, 2016), both of which can alter the air-sea fluxes and, hence, affect the monsoon dynamics. The Air-Sea Interaction Regional Initiative (ASIRI; Lucas et al., 2014; Wijesekera et al., 2016) aims to understand the upper ocean dynamics in the Bay of Bengal by extensive high-resolution measurements and modeling to eventually improve the monsoon forecasts.

The primary objectives of this study are to characterize the near-surface dispersion in the Bay of Bengal (specifically the dispersion of pairs of drifters) and to identify the dominant dispersion regime at submeso-scales.

We use high-resolution data from a large cluster of drifters deployed as part of ASIRI in the Bay of Bengal (Hormann et al., 2016) to characterize the near-surface dispersion. Close pairs of drifters that report their position with high temporal resolution allow studying the submeso-scale range of motions, which is challenging to observe synoptically with

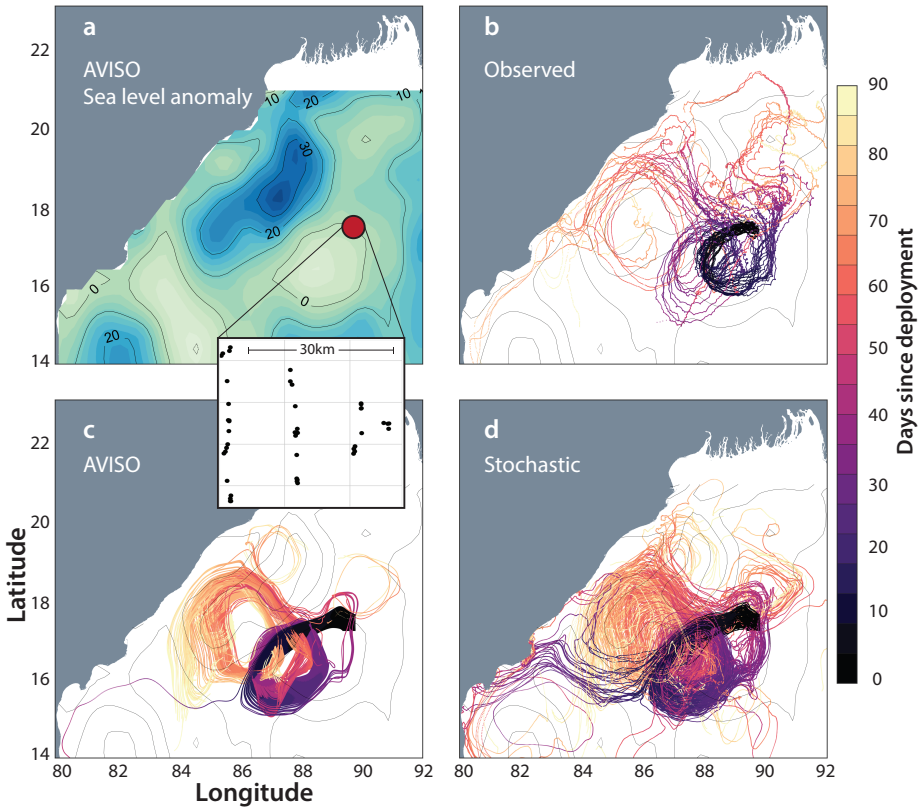

Figure 2-1: a) AVISO-derived sea-level anomaly in the northern Bay of Bengal on the day of the drifter release (September 2, 2015), with the drifter-release location indicated in red and the initial drifter positions overlaid. b), c), d) Trajectories of the b) observed drifters, c) AVISO-advected and d) stochastic drifters (AVISO-advected with stochastic closure at small scales), respectively. Color denotes time after deployment with darker colors indicating early times after deployment.

shipboard measurements because of the fast evolution of kilometer-scale features within timescales of hours to days. We compare the statistics of separations and velocities of drifter pairs to the theoretical predictions of local and non-local dispersion. Trajectories are low-pass filtered to determine the impact of inertial oscillations and small-scale processes on the dispersion statistics. For comparison, we simulate drifter trajectories using the satellite-derived, geostrophic flow field in the same region and contrast statistics from simulated, 'AVISO-advected', drifters to the observed drifters. To identify the dispersion by spatially uncorrelated motions, we add a stochastic closure to the AVISO-advected drifters at small scales which is correlated in time.

In what follows, Section 2.2 introduces the drifter dataset collected in the Bay of Bengal, the simulated drifter experiment based on satellite-derived flow fields, and the metrics used to characterize the near-surface dispersion. Section 2.3 presents the results for complementary dispersion statistics and compares drifter statistics to theoretical expectations. Section 2.4 offers a discussion of the results followed by a conclusion in Section 2.5.

2.2 Data and approach

2.2.1 Drifter deployments

We launched 46 surface drifters (one of which failed after deployment) during an extensive measurement campaign in the Bay of Bengal in September 2015 as part of ASIRI (Wijesekera et al., 2016; Hormann et al., 2016). The drifters were Surface Velocity Program (SVP) drifters (Niiler, 2001; Maximenko et al., 2013) that consist of a buoy and a holey-sock drogue at 15 m depth. SVP drifters are part of the Global Drifter Program (Niiler, 2001; Maximenko et al., 2013; Centurioni, 2018) that aims to map the near-surface circulation of the global ocean, and to provide SST and sea-level pressure data. These data are important for calibration and validation of satellite-derived SST datasets (e.g. Zhang et al., 2009) and for numerical weather prediction (Centurioni et al., 2017; Horányi et al., 2017).

Drifters were released at the edge of a mesoscale cyclonic eddy and across a strong salinity and density front (Figure 2-1a,b). With the goal of resolving motions over a wide range of length scales, we deployed drifters such that pair separations ranged from 0.5 km to 30 km. We achieved this by deploying 10 clusters of 4 drifters (Hormann et al., 2016) as shown in the inset in Figure 2-1. Each cluster of 4 drifters was deployed at almost the same time and provides six drifter pairs with a minimum separation of less than 1 km.

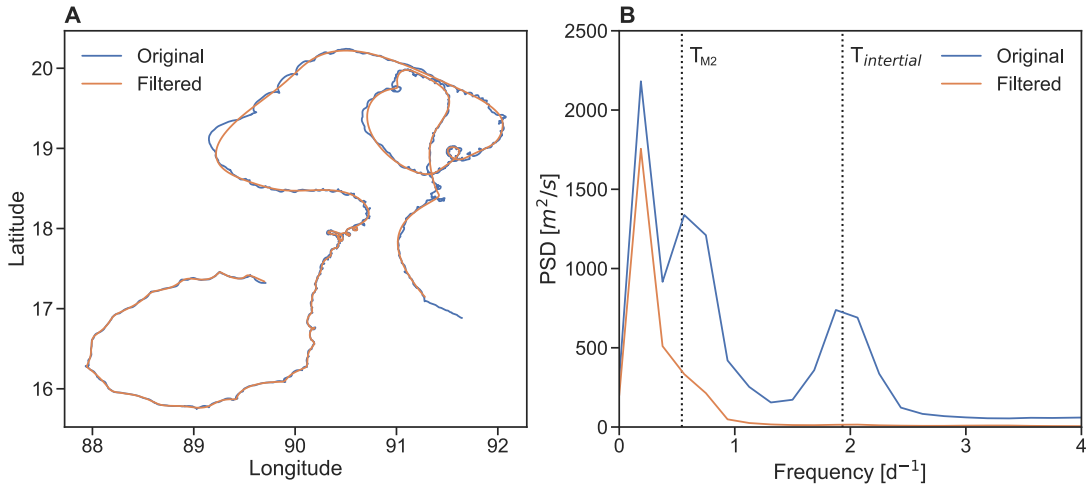

Figure 2-2: A) Example trajectory for one drifter experiencing inertial oscillations. Unfiltered and low-pass filtered trajectories are indicated in blue and red, respectively. B) Mean velocity power spectral density, before (blue) and after (orange) low-pass filtering with a cutoff of 1.5 times the inertial period. Dotted lines indicate the inertial and M2 tidal frequencies. The inertial and tidal spectral peaks seen in the original data (blue) are removed from the processed data by filtering (orange).

The entire array of 10 clusters, with an inter-cluster separation of 5 km, was deployed over a period of 48 hours.

During the first month after deployment, drifters reported their positions every 5 minutes (Hormann et al., 2016) giving a particularly high temporal resolution. After that, drifters reported every 30 minutes.

A conservative estimate of the position error is 50 m, which is likely a function of the region, sea state, and GPS coverage. The position data were quality controlled to remove erroneous GPS fixes and median-filtered with a 1-hour window to remove spurious events of acceleration. The velocity data of each drifter were then calculated by centered differencing. We bin the data to a 30 min grid for the first month and a 1 h grid after that by taking the median value of all points in this period. For the 90 days considered in this study, all drogues stayed attached, thus ensuring that they followed 15 m depth currents with an accuracy of ~ 0.01 m s^{-1} in winds up to 10 m s^{-1} (Niiler et al., 1995).

Since the drifters have a high temporal resolution, they resolve the timescales of processes such as near-inertial oscillations and tides, and Langmuir turbulence. We assume that the effect of wind and surface waves on the drifter positions is small since their drogues are at 15 m depth and the Stokes' drift is a second-order effect on the drifter displacement (Niiler et al., 1995). The Lagrangian frequency spectra of the observed drifters show high energy density at the inertial frequency and the M2 tidal frequency (Figure 2-2;

c.f., Hormann et al., 2016), however, substantially less than at sub-inertial frequencies. For the subsequent analysis, we low-pass filter the position data with a 5th-order Butterworth filter and a cut-off frequency of two-thirds the inertial period, $T_{inertial}$ (Figure 2-2). The velocity is then recomputed by finite differencing. This filtering removes both inertial oscillations and motions at the tidal frequencies (Figure 2-2). By applying the filter in the forward and backward direction, edge-effects are minimized. This low-pass filtered data set allows us to separate the effect of near-inertial motions on the dispersion statistics.

2.2.2 AVISO-advected drifters

As a reference dataset for the large-scale, geostrophic circulation, we simulate drifters that are advected by satellite-derived, geostrophic currents U_{geo} computed from the daily, delayed-time AVISO sea level anomaly (Figure 2-1c; Le Traon et al., 1998; Ducet et al., 2000). The sea level anomaly product is gridded to $\frac{1}{4}^{\circ}$, which is about half the local deformation radius L_D.

We trace the trajectories of the AVISO-advected drifters by time-integrating the currents using a 4th-order Runge-Kutta scheme and an hourly time step (Figure 2-1c). This time step is well below the temporal resolution of AVISO; the geostrophic velocities U_{geo} are therefore interpolated linearly in time. Cubic spatial interpolation is used to find the velocity at each drifter position.

In order to compare with the observed trajectories, we release the AVISO-advected drifters in the same region in the Bay of Bengal and at the same time as the real drifters. Since we are interested in pairs of drifters, we initialize pairs of drifters with fixed initial separation creating a grid of N drifters and adding a second grid offset by a distance r_0, where separation r_0 is the minimum distance that a pair of drifters is separated. We simulate 200 AVISO-advected drifters, which provide a combination of 19,900 drifter pairs at every time step, at least 100 of which have the minimum initial separation.

2.2.3 Stochastic drifters

Lagrangian trajectories of fluid parcels are significantly altered by small-scale processes that influence the dispersion properties, e.g., how fast they spread from their source region or for how long they are trapped in a flow feature.

First-order stochastic models give reasonably realistic results when modeling drifter trajectories in the ocean (Griffa et al., 1995; LaCasce, 2010; Koszalka et al., 2009; Haza et al., 2012). As opposed to zeroth-order models, which are stochastic in the drifter positions,

first-order models are stochastic in the velocity. The first-order stochastic model velocities u_i include an exponentially-fading memory of the past velocity (first term on right-hand side in Equation 2.1) and a noise increment $d\omega$ of a continuous Wiener process W(t) (second term on right-hand side in Equation 2.1). The new drifter position x_i along a trajectory is then found by integrating the following stochastic differential equation for the x-component (and analogously for the y-component) of the position:

$$du_i = -\frac{1}{T_L} u_i dt + \sqrt{\frac{2}{T_L}} \nu d\omega \tag{2.1}$$

$$dx_i = (u_i + U_{geo}) dt \tag{2.2}$$

where U_{geo} is the background, AVISO-derived current, $\nu = \langle u_i^2 \rangle^{1/2}$ the mean square single particle velocity, which can be interpreted as the turbulent velocity fluctuations, and T_L the e-folding time of the memory loss.

We take T_L to be the Lagrangian timescale estimated at 1 day from the velocity autocorrelation of the high-pass filtered drifter trajectories (with cutoff frequency $\frac{2}{3} T_{inertial}$). As Koszalka et al. (2009) suggest, we then tune the amplitude of the noise such that the relative dispersion matches the observed relative dispersion. We arrive at a value of $\nu = 0.02$ m/s for the turbulent velocity fluctuation, which is similar to the value found by Haza et al. (2012).

The tuning parameters of the first-order model are the Lagrangian decorrelation time scale and the amplitude of the velocity fluctuations - both are estimated from the observed Lagrangian trajectories. The Lagrangian decorrelation time scale is estimated from the velocity autocorrelation of the ensemble of drifters. The velocity fluctuations are estimated from the single particle diffusivity.

We use the first-order stochastic model to account for the subgrid processes and superpose it onto the AVISO-derived background currents U_{geo} (Figure 2-1d). The resulting stochastic trajectories deviate significantly from deterministic AVISO-advected trajectories due to small-scale perturbations that displace drifters enough to leave geostrophic streamlines. The AVISO-advected drifters lack this small-scale variability. Furthermore, the added stochastic component du_i to the mean flow is uncorrelated in space.

In the following sections, we will refer to three different datasets as 1) the observed drifters, 2) the AVISO-advected drifters, and 3) the stochastic drifters, which are the AVISO-advected drifters with stochastic noise.

2.2.4 Dispersion metrics and structure functions

Relative dispersion

A common metric for the dispersion of two particles is the mean square separation, known as relative dispersion D^2 (e.g., Richardson and Stommel, 1948; LaCasce, 2008; Lumpkin and Elipot, 2010), where the separation is the magnitude of the separation vector $r = |\mathbf{r}|$. Relative dispersion is the ensemble average of r^2 over all pairs that are closer than a small distance δ at an instant during the drift.

Here we use original ($r < \delta$ initially) and chance pairs ($r < \delta$ at a later time during the drift) (LaCasce, 2008). Thanks to the dense initial deployment of drifters, the majority of drifter pairs are original pairs (about 92%). Relative dispersion is then defined as the variance of pair separation distances of the selected N pairs

$$D^2(t) = \frac{1}{N} \sum_{i \neq j}^{N} \|\vec{x}_i(t) - \vec{x}_j(t)\|^2. \tag{2.3}$$

Trajectories are sorted such that they begin with the time of minimum separation. The time is thus relative to the time of minimum separation $t = t - t_0$. The relative diffusivity is defined as the rate of change of the relative dispersion

$$\kappa_{rel}(t) = \frac{1}{2} \frac{d}{dt} D^2(t) \tag{2.4}$$

and is often binned as a function of separation r.

Relative dispersion D^2 strongly depends on the correlation between velocities of pairs of drifters (LaCasce and Ohlmann, 2003; Koszalka et al., 2009). The early-time and the long-time limits are trivial. At early times, when pair separations are small, pair velocities differ approximately by a linear shear. The pair velocity correlation is thus constant, and pairs spread like t^2. At large separations, when pair separations reach the scale of the energy-containing eddies, pair velocities become uncorrelated, and the relative dispersion resembles a random walk with constant particle diffusivity. This diffusivity asymptotes to twice the diffusivity with which a single particle spreads around its initial location. The ensemble-average single particle diffusivity is also called absolute diffusivity (LaCasce and Bower, 2000; Kirwan et al., 1978).

At intermediate scales, however, the relative dispersion can be predicted from turbulence scaling laws given the energy spectrum, $E \sim k^{-\alpha}$ and is often referred to as turbulent dispersion. It can then be shown that in a non-local dispersion regime with

$\alpha \geq 3$, here referred to as the Lundgren regime, we expect the relative dispersion to grow exponentially in time (Lundgren, 1981; Lin, 1972). In a local regime with $1 < \alpha < 3$, we expect relative dispersion to grow as a power law $D^2 \sim t^{\frac{4}{(3-\alpha)}}$ (Foussard et al., 2017). If $\alpha = \frac{5}{3}$, relative dispersion grows like $D^2 \sim t^3$, subsequently termed Richardson dispersion (Richardson, 1926; Morel and Larceveque, 1974). Similarly, we expect scaling laws to hold for the relative diffusivity. For a self-similar energy spectrum of the form $E \sim k^{-\alpha}$, it can be shown that $\kappa_{rel} \sim r^{\frac{(\alpha+1)}{2}}$ (Bennett, 1984; LaCasce, 2008). This scaling law reproduces $\kappa_{rel} \sim r^{4/3}$, Richardson 4/3-law (Richardson, 1926), for $\alpha = \frac{5}{3}$, and $\kappa_{rel} \sim r^2$ for $\alpha = 3$.

We estimate the 95% confidence interval of the relative dispersion and diffusivity by bootstrapping. For each time, the population of available pairs is sampled 1000 times with replacement and the statistics are computed on each subsample. The confidence interval is then determined from the distribution of values that the subsamples generate.

Finite-size Lyapunov exponent

Since pair dispersion is not only a function of the velocity field, but also of the pair separation itself, it is necessary to adopt metrics that invoke distance as their independent variable. Distance-averaged statistics treat the positions and velocities as Eulerian point measurements on an unstructured grid. Although Eulerian and Lagrangian statistics should be equivalent, sparse drifter trajectories often yield different results between time-averaged and distance-averaged metrics.

The Lyapunov exponent is a measure of the rate of divergence of neighboring trajectories. It is widely used to identify trajectories that separate exponentially fast (Artale et al., 1997; Aurell et al., 1999) and is a technique borrowed from the dynamical systems approaches to study coherent structures in the flow (Haller, 2015). To compute the Finite-Size Lyapunov exponent (FSLE; e.g., LaCasce and Ohlmann, 2003; LaCasce, 2008), we create an array of distance classes $r_n = r_0\epsilon^n$, $n = 1, 2, 3 \ldots$, where $\epsilon = \sqrt{2}$ is an arbitrary constant, and record the time T_n that each pair takes to separate by a finite distance r_n. The FSLE λ_n are then determined by

$$\lambda_n = \log(\epsilon)\frac{1}{\langle T_n \rangle} \tag{2.5}$$

where $\langle \cdot \rangle$ is the ensemble average over all pairs. Contrary to the relative dispersion, all drifter pairs regardless of their initial separation are taken into account.

In theory, Lyapunov exponents are used to study exponential growth of pair separations. If the FSLE is constant over a range of distance classes, the e-folding timescale is constant,

which is equivalent to an exponential growth of pair separations. However, FSLEs are also useful to study growth of separations that is not exponential; we can use scaling arguments to relate the FSLE power law exponent β to the mean square separation D^2 as $D^2 \sim t^{-2/\beta}$.

Previous studies have shown that FSLEs are sensitive to the temporal evolution of the data (LaCasce and Ohlmann, 2003; Poje et al., 2010), as well as the implementation of the method (Lumpkin and Elipot, 2010; Haza et al., 2008). If the temporal resolution is not high enough, FSLEs underestimate the maximum Lyapunov exponent and miss transitions between regimes. Similarly, the quality of drifter data affects the estimate, as small-scale noise in the position data contaminates the FSLE at scales that are up to 6 times larger than the noise scale (Haza et al., 2014).

Here, we use the method of fastest crossing (e.g., Lumpkin and Elipot, 2010; Haza et al., 2008) to determine T_n. While the method of first crossings (e.g., LaCasce, 2008) only accounts for the first time a pair's separation grows from one distance class to the next, we break up the time series of pair separation into monotonically increasing segments and record every incident that a pair crosses a distance class. By counting every crossing, we increase the number of data points per distance class and alleviate the problem of small numbers of pairs. Furthermore, our half-hourly pair separations never exactly coincide with the edges of distance bins. As suggested by Haza et al. (2008), we linearly interpolate the time it would take to exactly reach the bin edge, thus, increasing the accuracy of crossing times and compensating for the limited temporal resolution of the data.

We estimate the 95% confidence interval of the FSLE by bootstrapping. For each separation bin, we generate 1000 subsets of the available crossing times by randomly resampling the data with replacement. For each subset, the FSLE is computed with the method described above. The confidence interval is then determined from the distribution of values that the subset generate.

Pair separation PDF

Richardson (1926) was the first to distinguish dispersion regimes by studying pair separation probability density functions (PDFs) $p(r, t)$ in what he called 'distance-neighbor functions'. These describe the probability that a pair released with initial separation r_0 will have separation r at time t. PDFs and their statistics are powerful because they illuminate the pair dispersion process (Sullivan, 1971) and encapsulate conventional pair dispersion statistics; the second moment of the pair separation PDF, for instance, is the

relative dispersion. By comparing PDFs to the theoretically expected solutions for a given flow field, we can distinguish between different turbulent dispersion regimes (LaCasce, 2010; Beron-Vera and LaCasce, 2016; Bennett, 1984; Graff et al., 2015).

In theory, if the energy spectrum $E(k)$ is known, we can derive a scaling prediction for the diffusion coefficient κ_2. Using the initial condition $p(r, t = 0)$, we can then describe the evolution of the pair separation PDFs with a Fokker-Planck equation (e.g. Beron-Vera and LaCasce, 2016; Bennett, 2006):

$$\frac{\partial p}{\partial t} = \frac{1}{r}\frac{\partial}{\partial r}\left(r\kappa_2 \frac{\partial p}{\partial r}\right). \tag{2.6}$$

For uncorrelated, normally-distributed drifter velocities, the diffusion parameter κ_2 is constant and equal to twice the single-particle diffusivity. In this case, the pair separation PDF resembles a Rayleigh distribution (Beron-Vera and LaCasce, 2016). In turbulent flow, however, drifter velocities are correlated and we can find solutions for the Fokker-Planck equation as a function of time and separation. For a given energy spectrum, e.g., the those associated with the (Richardson, 1926) regime and the (Lundgren, 1981) regime, the diffusivity κ_2 can be determined. Good summaries and derivations can be found in LaCasce (2010) and Bennett (2006).

To compare our data to the theoretical PDFs of the Lundgren, Richardson, and Rayleigh regimes, we first estimate κ_2 for each of the regimes. In the Richardson regime, the relative diffusivity is $\kappa_2 = \beta r^{4/3}$, where β is related to the third root of the energy dissipation rate (Graff et al., 2015; LaCasce, 2010; Beron-Vera and LaCasce, 2016). We find β by fitting the theoretical prediction for the relative dispersion to the data. These fits are only computed over the initial period until separations are ten times as large as the initial separation r_0. Analogously, in the Lundgren regime, the relative diffusivity is $\kappa_2 = r^2/T$, where T is related to the third root of the enstrophy dissipation rate (Graff et al., 2015; Beron-Vera and LaCasce, 2016; LaCasce, 2010). T is found similarly, by fitting the theoretical prediction of relative dispersion to our data for scales $r < 10r_0$. For the Rayleigh regime, the diffusion parameter is $\kappa_2 = \langle r^2 \rangle / 2t$, which is twice the single particle diffusivity. We determine κ_2 from the mean of the relative dispersion for $t >$20 days.

Using κ_2, theoretical predictions can be made for the pair separation PDFs and their moments. The PDF for Richardson dispersion is self-similar with a kurtosis that asymptotes to 5.6 in the long-time limit. The PDF for non-local dispersion is log-normal and becomes more peaked with time; consequently, its kurtosis grows exponentially with time. The

PDF for uncorrelated velocities has a kurtosis of 2 for a Rayleigh distribution (Bennett, 1987; Beron-Vera and LaCasce, 2016).

Structure functions

The variance of the pair velocity differences $\delta u = \langle \|\mathbf{u}_i - \mathbf{u}_j\| \rangle$ is defined as the second-order velocity structure function $S_2 = \langle \delta u^2 \rangle$. Separating the velocity $\mathbf{u}$ into its longitudinal ($\mathbf{u}_l = \frac{r \cdot \mathbf{u}}{|r|} \hat{l}$) and transverse ($\mathbf{u}_t = \frac{(r \times \mathbf{u}) \cdot \hat{k}}{|r|} \hat{t}$) components (where $\hat{l}$ and $\hat{t}$ are unit vectors in the longitudinal and transverse direction, respectively) (Bühler et al., 2014; Balwada et al., 2016; Babiano et al., 1990), we define the longitudinal (S_l) and transverse (S_t) structure functions as

$$S_l(r) = \langle \|\mathbf{u}_{l_i} - \mathbf{u}_{l_j}\|^2 \rangle \tag{2.7}$$

$$S_t(r) = \langle \|\mathbf{u}_{t_i} - \mathbf{u}_{t_j}\|^2 \rangle, \tag{2.8}$$

where $\langle \cdot \rangle$ denotes the average over separation distances of all distinct drifter combinations i, j, and r is the magnitude of the separation vector. Here, we take the average of the squared velocity difference for the computation of the structure function.

In theory, the second-order velocity structure function is related to the energy spectrum by a Hankel-Fourier transform (Bennett, 1984; LaCasce, 2016)

$$S_2(r) = 2 \int_0^\infty E(k)(1 - J_0(kr) dk) \tag{2.9}$$

where J_0 is the zeroth-order Bessel function.

Due to the difficulty of observing the energy spectrum in the ocean, it has been used to understand the distribution of energy across scales. As LaCasce (2016) points out, however, the calculation of energy spectra from drifter-derived structure functions is not practicable. Particularly at large scales, where a limited number of pairs is available and only a few realizations of the flow are sampled, the transformation to energy density produces large uncertainties. Nonetheless, structure functions give valuable information about the distribution of energy as a function of scale (Balwada et al., 2016). In particular, they are able to reproduce the scale-dependent transitions from one inertial subranges to another in the energy spectrum.

Examining the asymptotic limits of this integral (Equation 2.9) offers illuminating

physical insights (Bennett, 1984; Balwada et al., 2016; Babiano et al., 1990):

$$S_2(r) = \frac{r^2}{2} \int_0^{2/r} k^2 E(k) dk + 2 \int_{2/r}^{\infty} E(k) dk, \tag{2.10}$$

where r is the pair separation distance, $E(k)$ the kinetic energy spectrum, and k is the total wavenumber. In the limit of $r \to 0$, structure functions are dominated by the enstrophy provided by velocity gradients of the largest eddies in the flow. In the limit of $r \to \infty$, structure functions are dominated by the energy of eddies of the same scale as r.

We can predict the power law behavior of structure function from Equation 2.10. Given a self-similar energy spectrum $E(k) \sim k^{-\alpha}$, the structure functions scale like $S_2 \sim r^{\alpha-1}$ (Bennett, 1984). In a non-local regime with $\alpha = 3$, the structure function will scale like r^2. In a local regime with $\alpha = 5/3$, the structure function will scale like $r^{2/3}$.

The longitudinal and transverse components of the structure function are not independent. Assuming that the structure functions have a power law dependence $S_2 \sim r^m$, a purely non-divergent flow will lead to a ratio of $S_t/S_l = m + 1$, and a purely irrotational flow will lead to $S_t/S_l = 1/m + 1$ (Balwada et al., 2016).

Helmholtz decomposition

As for every vector field, we can decompose the velocity vector into divergent and rotational components $\vec{u} = -\nabla \times (\vec{k}\psi) + \nabla\phi$. Performing a Helmholtz decomposition of the velocity structure function (Bühler et al., 2014; Lindborg, 2014), we can separate rotational S_r and divergent S_d components of the relative velocity and further characterize the flow field. We compute the divergent and rotational structure functions as

$$S_d(r) = S_l(r) - \int_0^r \frac{1}{r}(S_t - S_l) dr \tag{2.11}$$

$$S_r(r) = S_t(r) + \int_0^r \frac{1}{r}(S_t - S_l) dr. \tag{2.12}$$

In a two-dimensional, quasi-geostrophic regime, we expect the flow to be nearly non-divergent. In this case the rotational component of the structure function will be $S_r > S_d$. In an unbalanced wave-continuum, e.g. with a Garrett-and-Munk spectrum, we expect the divergent component to become important. For internal waves the ratio of S_r/S_d depends on wave frequency and inertial frequency (Bühler et al., 2014). Near-inertial oscillations are expected to have $S_r/S_d = 1$. Furthermore, the divergent and rotational components help to identify the scales at which dynamics transition from one regime to another.

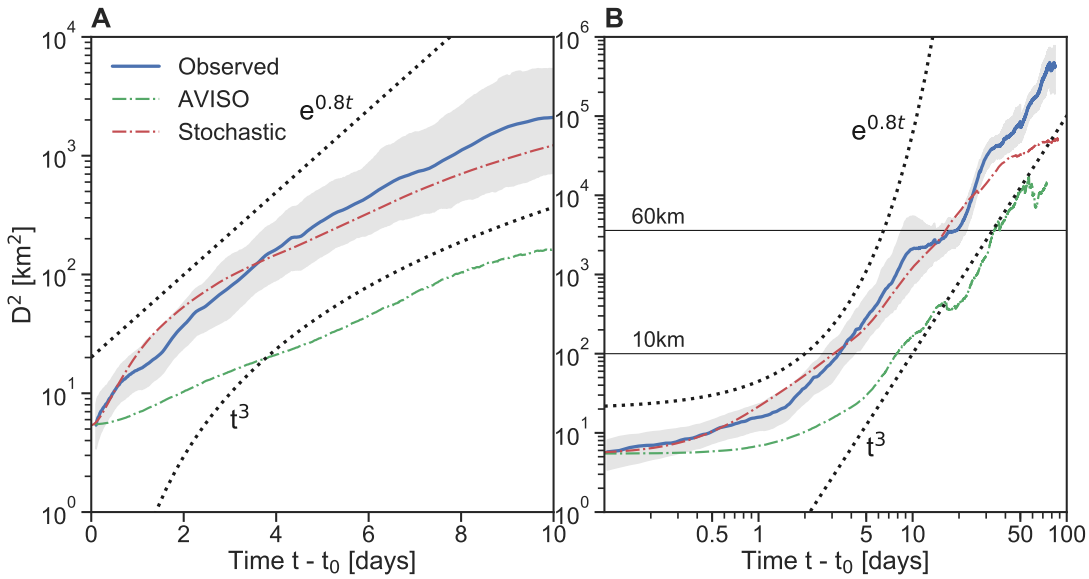

Figure 2-3: Relative dispersion D^2 as a function of time, plotted for the first 10 days (A) on a semilog axis, and the full record (B) on log-log axes. The blue, green, and red curves denote the observed, AVISO-advected and, stochastic (AVISO-advected with stochastic closure) drifter trajectories, respectively. The shaded area is the bootstrapped 95% confidence interval of the relative dispersion. Theoretical power laws are indicated by black dotted lines.

2.3 Results

In this section, we characterize the dispersion in the upper ocean using the pair dispersion statistics and structure functions described above. We focus on the early-time and small-scale behavior that falls into the spatiotemporal regime of submeso-scale motions.

2.3.1 Relative dispersion

The observed relative dispersion D^2 calculated from the drifter array shows two distinct regimes (Figure 2-3). During the first 4 days when separations are small ($r < 10$ km), relative dispersion grows exponentially with an e-folding timescale of about 1.25 d. As separations reach the deformation radius $L_D = 60$ km, they transition approximately to a t^3 power law. The initial exponential growth is as expected for non-local dispersion, as is the cubic power law growth for local dispersion.

At long times, $t >$100 days, relative dispersion does not flatten to linear growth. Linear growth is expected for constant relative if pair separations grow larger than the dominant eddy size ($\approx$ 100 km) and become uncorrelated (Figure 2-4). A possible explanation is that the Indian coast prevents drifters from spreading isotropically and drifters become

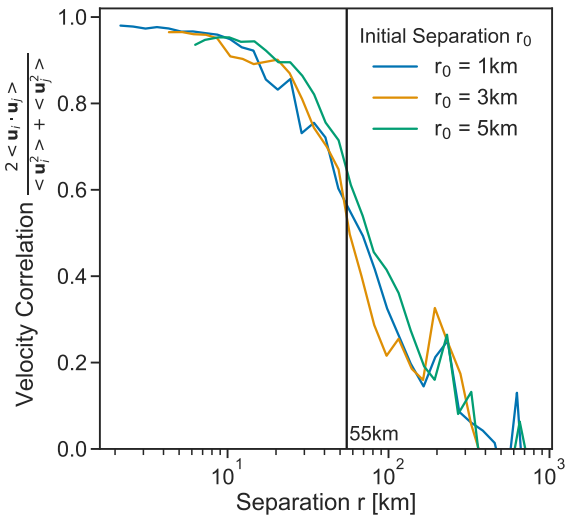

Figure 2-4: Normalized pair velocity correlation normalized by the single particle velocity variance for three different initial separation: $0 \leq r_0 < 2$ km (blue), $2 \leq r_0 < 4$ km (orange), $4 \leq r_0 < 6$ km (green). The black line indicates an estimate for the decorrelation scale, where the correlation has fallen off by 1/e from its maximum.

entrained into the boundary current (Figure 2-1). Furthermore, dispersion calculated for large separations above 100 km has uncertainty, as only a small number of drifter pairs is available at this scale.

The simulated, AVISO-advected drifters are explicitly advected with geostrophic currents that lack variability at scales smaller than $1/4^\circ$. AVISO-advected drifters are able to reflect the overall drift pattern of the observed drifters. Their trajectories, however, are significantly smoother and their rates of dispersion are slower than for the observed drifters. After the same period of drift, AVISO-advected drifters stay much more coherent and spread over a much smaller area than the observed drifter trajectories (Figure 2-1).

Estimates of relative dispersion further illustrate the difference between the AVISO-drifters and the observed drifters (Figure 2-3). Since the AVISO energy spectrum is steep, likely $\alpha \gg 3$, non-local dispersion and exponential growth is expected. For the first 10 days, the AVISO relative dispersion grows exponentially, however, with a small growth parameter. Since the AVISO-derived currents lack variability below 1/4 degree (about 30 km), the dispersion at small scales is dominated by mesoscale shear. After ten days, however, the AVISO drifters approximately follow a t^3 power law. Interestingly, the AVISO drifters show the same plateau in relative dispersion as the observed drifters after about 5-10 days, possibly, a synoptic feature that traps drifters the same way as in the observations (Figure 2-3B).

Using a maximum likelihood estimator, we fit an exponential function to the AVISO relative dispersion by determining and find that an exponential function is a good approximation. This is in agreement with the theoretical expectation, given that AVISO altimetry lacks variability below 1/4 degree and with a steep associated kinetic energy spectrum ($\alpha >> 3$). However, the e-folding timescale with which the AVISO relative dispersion grows is significantly smaller than for the relative dispersion of the observed drifters.

The stochastic drifters that include superposed noise in addition to the AVISO currents improve both the qualitative trajectories (Figure 2-1), as well as the relative dispersion estimates. Generally, the stochastic noise increases the magnitude of relative dispersion compared to the AVISO drifters, such that the behavior is closer to the observed drifters. During the first 4 days, however, stochastic drifters show different behavior than the observed drifters. Their relative dispersion grows more rapidly, possibly like t^2 or t^2. The late-time behavior is within 95% of the observed drifters and shows a t^2. An alternative explanation for this behavior is the result of random motion in the mesoscale shear which produces the same relative dispersion as Richardson dispersion (Bennett, 1987).

The relative diffusivity κ_{rel} is noisier than the relative dispersion because it is the time-derivative of relative dispersion. In our data, we locally encounter zero and negative slope of D^2, suggesting converging pairs of drifters for which the κ_{rel} is not well defined. Here, we calculate the derivative of the mean square separation, focusing on diffusivity that is larger than zero and only using those values that consist of at least 20 data points.

In Figure 2-5, the relative diffusivity is shown as a function of pair separation. For the observed drifters, a r^2 dependence is evident at separations below the deformation radius L_D. Although the variability is large, a transition is expected at L_D, where the relative diffusivity starts to flatten to a $r^{4/3}$ power law. As already pointed out in the relative dispersion results, the diffusivity does not saturate at the largest, observed scales suggesting that a regime of constant relative diffusivity is not reached. This would be expected if $r > L_D$ and the combined effect of multiple eddies is sampled. The theoretical expectations for non-local energy spectra $\alpha \geq 3$ is that the diffusivity grows like r^2. For a local energy spectrum with $1 < \alpha \leq 3$, the theoretical prediction is $r^{\frac{(\alpha+1)}{2}}$. For $\alpha = 5/3$, specifically, the diffusivity grows like $r^{4/3}$, Richardson's 4/3 law. The observations lie in an envelope in between the local and non-local regime, curve fitting suggests, however, that it more closely follows a r^2 power law.

The AVISO drifters and stochastic drifters show a similar behavior but with lower overall diffusivity. The stochastic noise increases the diffusivity compared to the AVISO

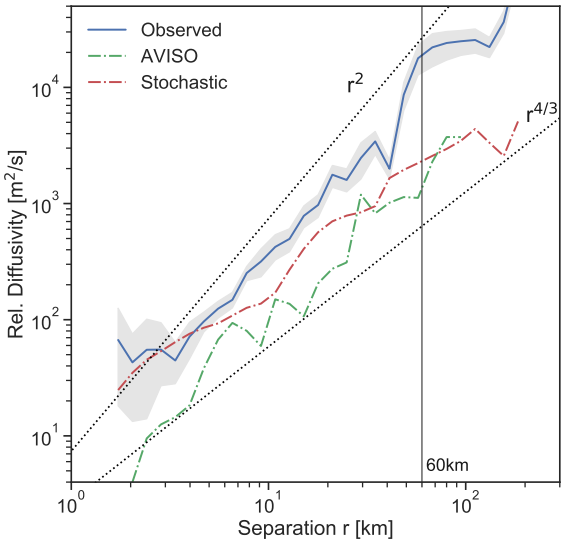

Figure 2-5: Relative diffusivity, the time derivative of the relative dispersion (Figure 2-3), as a function of separation r. The blue, green and, red curves denote the observed, AVISO-advected, and stochastic (AVISO-advected with stochastic closure) drifter trajectories, respectively. The shaded area is the bootstrapped 95% confidence interval of the relative diffusivity. The dotted lines indicate r^2 (expected in non-local regimes) and $r^{4/3}$ (expected in local regime).

drifters which is particularly pronounced at small scales below 5 km. Curve fitting results suggests that the AVISO drifters follow r^2 more closely, whereas the stochastic drifters follow $r^{4/3}$. At the largest scales, the stochastic and AVISO drifters have a diffusivity that is an order of magnitude smaller than the observed, despite the expectation that all three datasets should converge to the same diffusivity. This might be a result that is caused by a strong reduction of available pairs at these scales and the fact that the simulated drifters experiment might not have reached saturation over the duration of the observed drifter experiment.

2.3.2 Finite-size Lyapunov exponent

The observed FSLEs (Figure 2-6) are largest for the smallest separations. The associated e-folding time is about one day which is close to the e-folding time estimated from the initial phase of the relative dispersion. Due to limited number of pairs available, however, uncertainties are large at these smallest scales. With the number of data points available, it is difficult to validate, whether the FSLE is constant over a range of scales as predicted for exponential pair dispersion. At intermediate scales, below L_D, the FSLEs scale like $r^{-2/5}$. The equivalent slope of the relative dispersion is 5, indicating a rapid timescale of

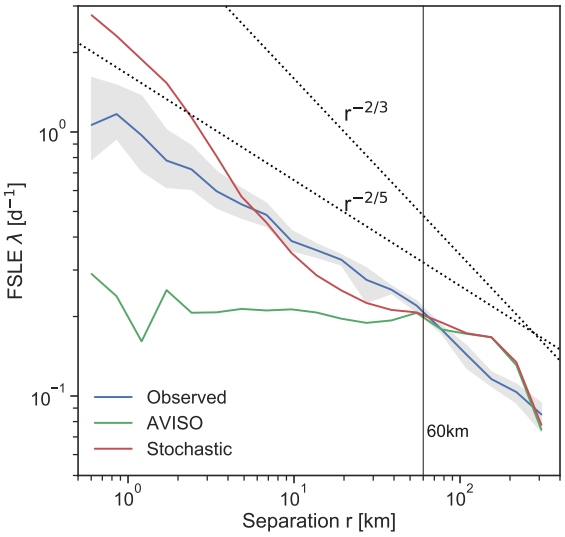

Figure 2-6: Finite-Si Lyapunov Exponent (FSLE) as a function of separation r. The blue, green and, red curves denote the observed, AVISO-advected, and, stochastic (AVISO-advected with stochastic closure) drifters, respectively. The shaded area is the bootstrapped 95% confidence interval of the FSLE. Dotted lines denote power law dependencies.

separation. In agreement with the relative dispersion and diffusivity, we find a change of behavior at the deformation radius. For separations larger than L_D, FSLEs fall off like $r^{-2/3}$, which is the prediction for a Richardson-like dispersion with $D^2 \sim t^3$.

The AVISO drifters show a constant FSLE from about 1 km to the deformation radius. If the FSLE is constant across a range of scales, the e-folding time is constant, and pairs separate exponentially fast. The smallest scales below 1 km, however, suffer from large uncertainty. Above the L_D, the FSLE fall off more slowly than for the observed drifters. The stochastic noise generates FSLE that are larger than the observed FSLE for scales from 0.1 to 10 km. The effect of the noise decreases with increasing r, such that the stochastic drifters behave like the AVISO drifters above L_D. The large initial FSLE suggest faster separation rates of the stochastic trajectories than the observed trajectories, which is in agreement with the relative dispersion results. Yet, this increase in separation rates is a function of the magnitude of the stochastic noise (Section 2.2.4).

Since time resolution is important in the computation of FSLE and the sea level anomaly data is updated daily, it is expected that FSLE estimates from AVISO-advected drifters cannot resolve the e-folding time scale of 1-2 days below 5 km. Similarly, the 30 min resolution of the observed drifters might not be able to resolve the true maximum FSLE.

Table 2.1: Estimated parameters for the theoretical pair separation PDFs.

	Observed			AVISO			Stochastic		
Separation r_0 [km]	1	3	5	1	3	5	1	3	5
κ (Rayleigh) [km^{2}day^{-1}]	398	793	1300	20	40	55	148	161	165
T (Lundgren) [day^{-1}]	7.7	15.2	19.6	22.2	30	26.1	4.7	18.8	22.9
β (Richardson) [km$^{2/3}$day^{-1}]	0.51	0.41	0.52	0.2	0.28	0.40	0.74	0.45	0.51

2.3.3 Pair separation PDFs

The pair separation PDFs (at $t = 3$ days) are shown for three different initial separations in Figure 2-7. We choose separation classes that are centered at $r_0 = 1$ km, 3 km, and 5 km, each of which are 2 km wide (for example for the first class 0 <r_0<2 km). These initial separations are selected because they are in the range or scales for which FSLEs are large and relative dispersion indicates exponential growth.

Consider first the observed drifters (Figure 2-7a). Separations in the smallest separation class ($r_0 = 1$ km) are associated with the most peaked PDF. The two larger initial separation classes ($r_0 = 3$ km and $r_0 = 5$ km) are less peaked. The theoretical PDFs whose parameters are estimated from the relative dispersion curves (see Section 2.2 and Table 2.1) are calculated corresponding to the three initial separations r_0 at $t = 3$ days. The (non-local) Lundgren regime and the (local) Richardson regime are both close to the observed data in 1 km class. The theoretical curve for the Richardson regime and the estimated curve from kernel density estimation of the observed data are not significantly different. The larger the initial separation, the lower the predictive power of the theoretical PDFs.

The PDFs for the AVISO separations (Figure 2-7b) occupy a much smaller range of scales. It is evident that the Lundgren distribution is the best fit for all three initial separation classes. The stochastic drifters, however, behave differently from the two other datasets. The stochastic noise causes a fast widening of the PDFs, such that both Lundgren and Richardson solutions fail to predict the distribution. The widening of the PDF is caused by uncorrelated motions and is comparable to the Rayleigh dispersion. Since we estimate the diffusion coefficient from the late-time behavior (t>10 days) of the relative dispersion, this diffusivity is not captured. The fast dispersion of the stochastic drifters at small scales (r<10 km) has also been observed in the relative diffusivity (Figure 2-5) and the FSLE (Figure 2-6). The character of this dispersion is different from Lundgren, Richardson as well as the late-time Rayleigh regime.

The theoretical solution for the Rayleigh regime, i.e., dispersion by uncorrelated pair velocities, does not describe any of the datasets. This is expected for these small initial

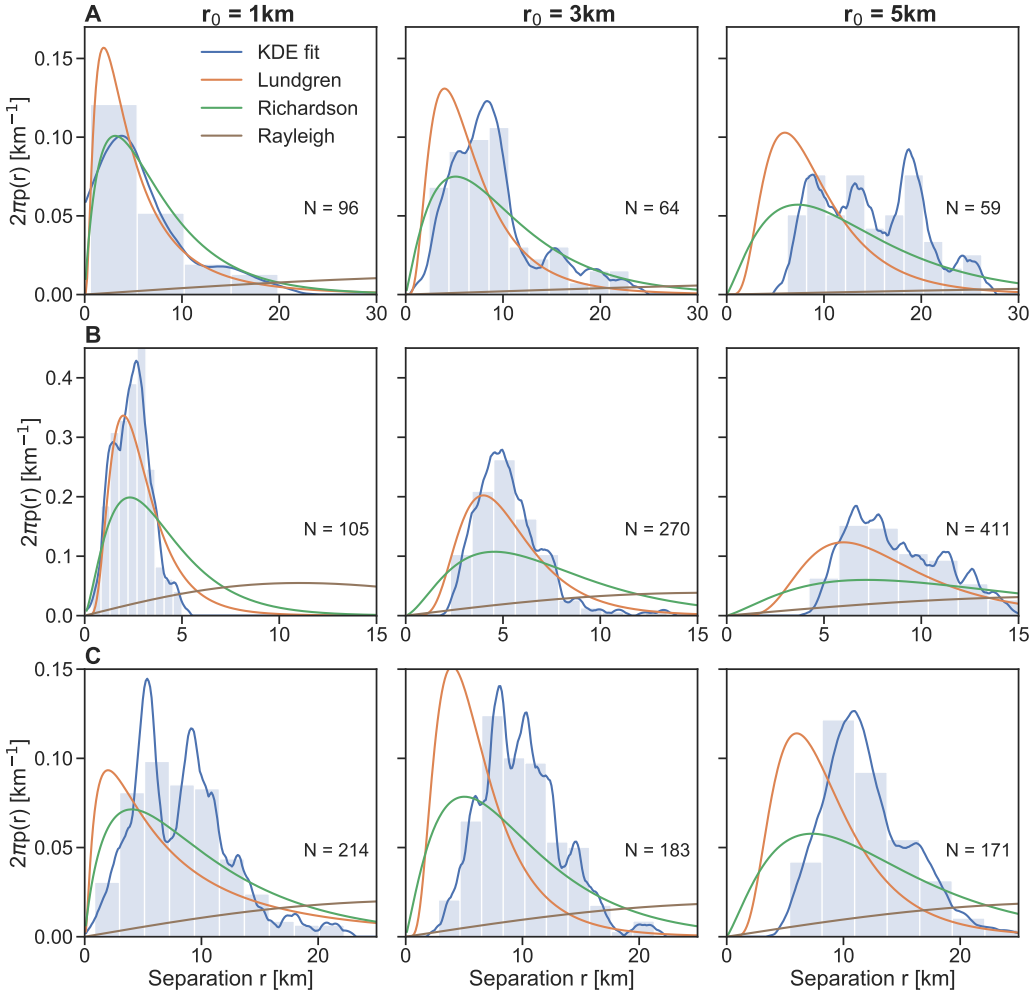

Figure 2-7: Pair separation PDFs at $t = 3$ days for different initial separations r_0 for each of the three datasets: A) observed, B) AVISO-advected, and C) and stochastic (AVISO-advected with stochastic closure) drifters. The theoretical PDFs are shown in color, for the non-local Lundgren (orange), local Richardson (green), and uncorrelated Rayleigh (brown) regime. The histogram and kernel density estimation of the measured distributions is in blue.

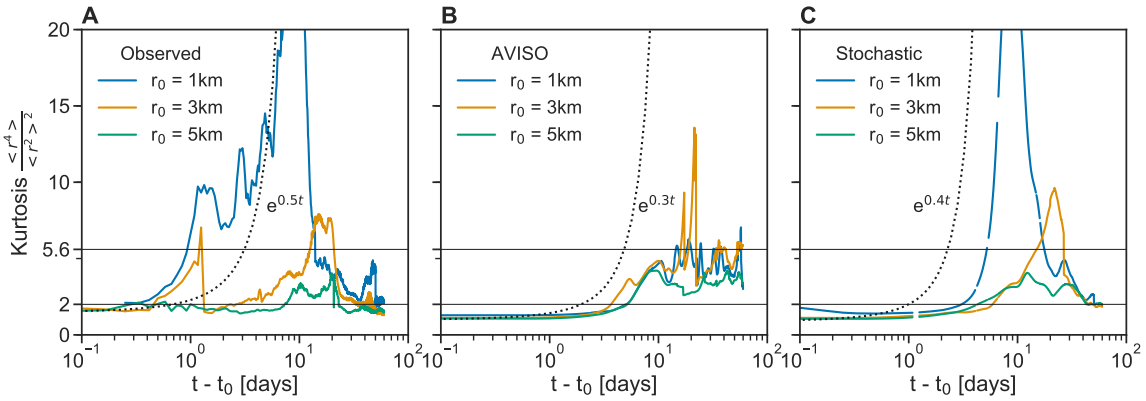

Figure 2-8: Kurtosis of the pair separation PDFs as a function of time for A) the observed, B) AVISO-advected, and C) stochastic drifters (AVISO-advected with stochastic closure). Colors indicate the three classes of initial pair separation r_0. Dotted lines indicate the values expected in the asymptotic limit of the Lundgren regime ($\sim e^t$), the Richardson regime (5.6), and the Rayleigh regime (2).

separations and after 3 days, in particular, because the diffusivity for the Rayleigh regimes is estimated from the late time relative dispersion. As we see in the velocity cross correlation (Figure 2-4), the velocities are correlated below the deformation radius L_D. Since all drifters are deployed in the same region, we expect that pairs likely sample the same features in all three datasets. Additionally, it is unclear if the diffusion coefficient κ_2 can be determined accurately from the relative dispersion curves for two reasons: a) As the late-time behavior is covered by fewer pairs, the uncertainties are relatively large, and b) the relative dispersion curve does not unambiguously reach the linear growth regimes that are expected for uncorrelated motions.

The kurtosis, the fourth moment of the PDFs, is a metric to quantify the peakedness of a distribution. We group the data into the three classes of initial separation r_0 and evaluate the kurtosis for each of those groups as a function of time (Figure 2-8).

In case of the observed drifters (Figure 2-8a), pairs that are initially close ($r_0 = 1$ km) generate an exponentially growing kurtosis that reaches a maximum value of 32 (not shown), clearly suggesting non-local behavior of the dispersion. Pairs with larger initial separation grow more slowly and reach a smaller maximum kurtosis (yet larger than the maximum value 5.6 expected for the Richardson regime). Interestingly, the kurtosis quickly falls off to values between 1 and 5 after about 15 days. It is somewhat surprising that values decrease so quickly, given that the energy-containing eddy size is clearly mesoscale and $\mathcal{O}$(60 km). A possible explanation for this is the sensitivity of the kurtosis to the tails of the pair separation PDFs. Pairs in the tails of the distribution develop quickly and could

decrease the kurtosis.

The kurtosis is affected by the number of points available in each distance bin. The number of points available can be controlled by widening the bins but that will artificially decrease the kurtosis of the distribution. Since there are different numbers of pairs for the AVISO, stochastic, and observed drifters, the width of the bins can affect the kurtosis and is likely the reason why the stochastic drifters have a larger kurtosis than the AVISO drifters.

The AVISO drifters (Figure 2-8B) produce less of an exponential growth (at least at these initial separation scales) with maximum values that are larger than 5.6. The late-time asymptotic behavior of the AVISO drifters could be identified as Richardson-like, as values oscillate around 5.6. Interestingly, and opposed to the observed drifters, values are larger than 2, suggesting that a Rayleigh regime can be ruled out.

Contrary to the AVISO drifters, the stochastic drifters generate an exponentially growing kurtosis (Figure 2-8C). Particularly the smallest separation class grows to a maximum value of 25, which can clearly be attributed to non-local behavior. The difference between AVISO drifters and stochastic drifters suggests that the stochastic noise facilitates faster separation. The exponential growth of the kurtosis also occurs at a later time than for the observed drifters which is an artifact of the resolution of the AVISO currents.

2.3.4 Structure functions

The structure functions S_2 for the observed drifters are shown in Figure 2-9A as a function of separation r. At intermediate scales, 10–100 km, S_2 approximately follows a $r^{2/3}$ power law. From scaling arguments, we know that $S_2 \sim r^{2/3}$ is the expectation for an energy spectrum with $E \sim k^{-5/3}$. At small scales (r<10 km) and at large scales (r>100 km), S_2 flattens to $r^{1/3}$ and $r^{1/2}$, respectively.

Low-pass filtering the trajectories affects S_2 such that it has less energy than the unfiltered dataset below 100 km. It can be argued that the filtered S_2 steepens relative to the unfiltered dataset between 10 and 100 km. In this range of scales, the power law is closer to r^1, which would be predicted for an energy spectrum of $E \sim k^{-2}$. As expected, the structure functions for the AVISO and stochastic drifters are smaller at scales below the resolution of the AVISO-derived currents (Figure 2-9A). S_2 from the AVISO drifters clearly follows a r^2 power law from 1 to 100 km and flattens above. This is expected since the energy spectrum for the AVISO currents $E \sim k^{-\alpha}$ is steep with $\alpha > 3$. The noise in the velocity of the stochastic drifters causes S_2 to be flat at scales below 30 km. Above that, S_2

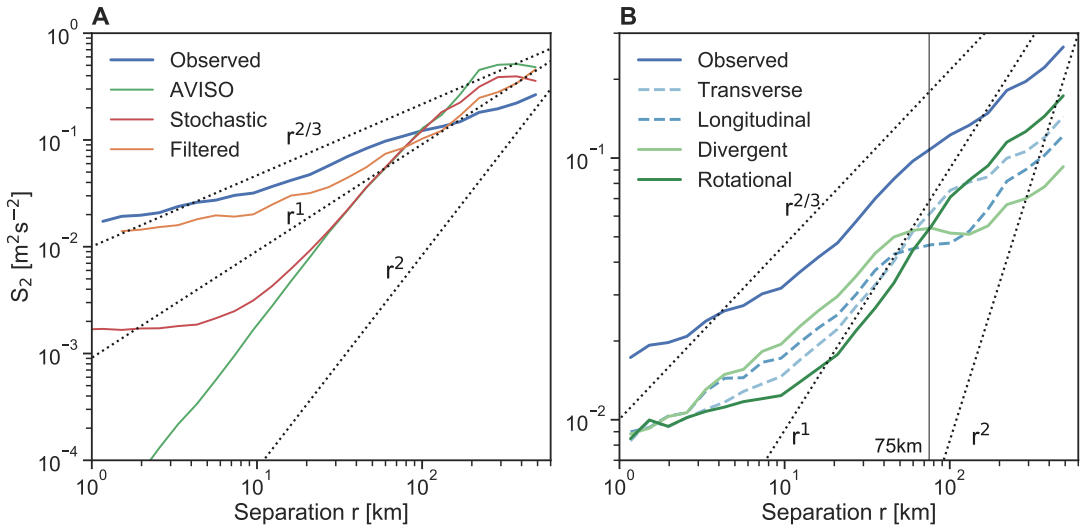

Figure 2-9: A) Second order velocity structure functions as a function of separation r for the observed, AVISO-advected, stochastic (AVISO-advected with stochastic closure), and low-pass filtered trajectories. B) Velocity structure functions after decomposition into longitudinal and transverse, and rotational and divergent components. The total observed structure function is the same in A) and B). The solid vertical line indicates the length scale at which the rotational component becomes dominant. The dotted lines indicate the theoretical slopes of non-local ($S_2 \sim r^2$), local ($S_2 \sim r^{\frac{2}{3}}$), and frontal energy spectra ($S_2 \sim r^1$).

from the stochastic drifters behaves similarly to S_2 from AVISO drifters.

It is evident in Figure 2-9B that the rotational component and the divergent component cross at approximately 75 km, which is close to the local deformation radius $L_D = 60$ km. S_d is dominant below 75 km and approximately determines the slope of S_2. Likewise, S_r is dominant above 75 km and approximately determines the slope of S_2 at large scales. The longitudinal and transverse components also cross but at slightly smaller scales (about 50 km). S_l is dominant below 50 km and S_t becomes dominant above. S_l grows like $r^{2/3}$ up to 50 km, consistent with a local energy spectrum, and flattens above.

The ratio of transverse to longitudinal components S_t/S_l (Figure 2-10A) of the observed drifters is constant at about 0.9 for r<50 km and increases to about 1.5 for r>75 km. S_t/S_l behaves the same way for the filtered drifter, while generally being larger. The AVISO drifters, however, generate a S_t/S_l that is larger than 3. S_t/S_l for the stochastic drifters increases from 1 at the smallest scales to about 3.2 above 75 km.

The ratio of rotational to divergent component S_r/S_d (Figure 2-10b) confirms the general pattern evident in the components of the structure function. S_r/S_d for observed drifters is dominated by the rotational component for r>75 km. Filtering removes energy

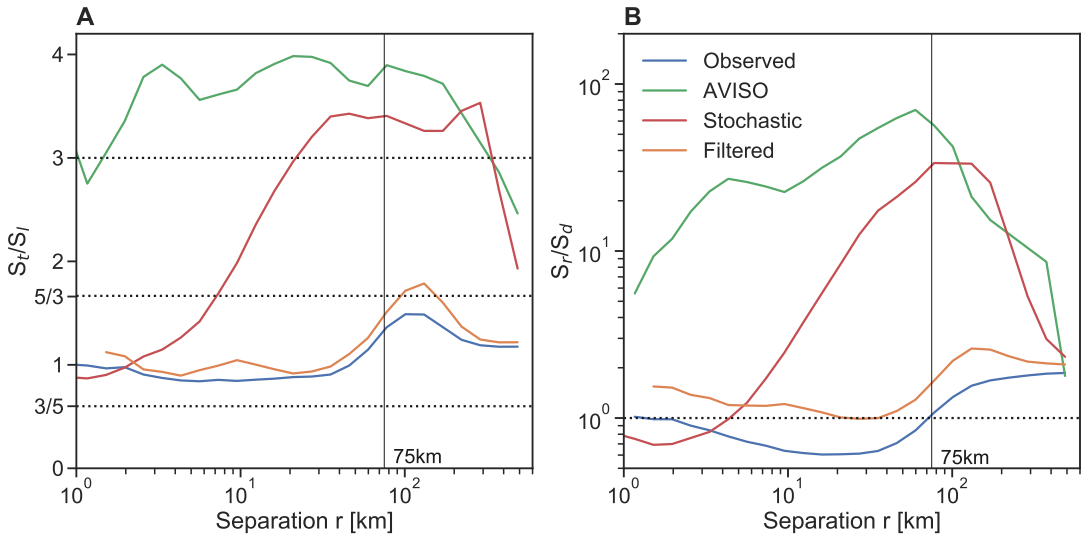

Figure 2-10: A) Ratio of the transverse and longitudinal component of the velocity structure function (S_t/S_l) as a function of separation r. B) Ratio of the rotational and divergent component of the velocity structure function after Helmholtz decomposition (S_r/S_d) as a function of separation r. Colors denote the observed, AVISO-advected, stochastic (AVISO-advected with stochastic closure), and low-pass filtered datasets. Horizontal dotted lines are for reference.

predominantly from the rotational component and shifts S_r/S_d to higher values. It appears that S_r/S_d for the filtered drifters is greater or equal to 1 at all times. In the cases of the AVISO drifters and the stochastic drifters, the rotational component is larger than the divergent component by at least an order of magnitude. At small scales, however, the divergent, stochastic noise dominates the stochastic S_r/S_d.

In the limit of divergence-dominated flow (r<10 km), the ratios agree with the theoretical expectations. The total structure function of the observed drifters has a slope of $m = 1/3$ or flatter (Figure 2-9a) which would predict S_t/S_l to be about 3/4. Similarly, in the limit of rotation-dominated flow, the total structure function has a slope of $m = 1/2$ which would predict S_t/S_l to be 1.5. For the AVISO field, for which $S_r/S_d > 1$ at all scales, the total structure function has a slope of $m = 2$ which predicts S_t/S_l to be 3.

The finding that motions are divergent at small scales suggests that two-dimensional, geostrophic dynamics are no longer dominant. Candidates for divergent motions could be the internal wave field, inertial oscillations, Langmuir turbulence as well as the horizontally divergent submesoscale flow.

Table 2.2: Dispersion regimes in Lagrangian statistics at submesoscales, $\mathcal{O}$(0.1-10km).

	Richardson (local)	Lundgren (non-local)	Observed
E(k)	$k^{-5/3}$	k^{-3}	-
S_2(r)	$r^{2/3}$	r^2	$r^{2/3}$
λ(r)	$r^{-2/3}$	const	$r^{-2/3}$
D^2(t)	t^3	e^t	e^t
κ_{rel}(r)	$r^{4/3}$	r^2	r^2
kur(t)	5.6	e^t	e^t

2.4 Discussion

2.4.1 Dispersion regimes

The results of the dispersion statistics (relative dispersion and diffusivity, FSLE, pair separation PDFs, and kurtosis) describe the dispersion characteristics of the flow in the Bay of Bengal. The combination of distance-averaged and time-averaged metrics allows for a more complete description of the flow. Additionally, the structure functions contribute to the understanding of the distribution of energy across scales. In the absence of knowledge about the energy spectra, this can be useful despite the fact that structure function can be affected by non-dispersive modes, which are part of the true, observed flow.

The drifter-derived relative dispersion and FSLE (for pairs with $r_0 < 3$ km) agree qualitatively on small scales and at the deformation radius L_D (Table 2.2). These suggests a non-local growth below 20 km and a local regime above the deformation radius L_D. However, the metrics disagree quantitatively: The e-folding timescale predicted by the FSLE is half as large as for the relative dispersion and the regime shift from exponential to power-law growth is at 20 km (Figure 2-6) as opposed to 10 km shown in the relative dispersion (Figure 2-3). The relative diffusivity is consistent with this result and grows like r^2, however, the transition from non-local to local is less pronounced. The general result agrees with previous results (Koszalka et al., 2009; LaCasce and Ohlmann, 2003). The difference between FSLE and relative dispersion can be attributed to the quality of the data (particularly the position error) (Haza et al., 2014; Poje et al., 2010) but can also be affected by the fact that different subsets of pairs are used in the calculation (LaCasce and Bower, 2000).

The pair separation PDFs and their kurtoses suggest that a Lundgren distribution is the best fit for initially close pairs ($r_0 = 1$ km) and for the first 10 days of the drift (Table 2.2). The rate of strain field of the mesoscale eddies is a logical candidate for the non-local dispersion of small drifters pairs. Furthermore, the kurtosis of the pair separation PDFs

grows exponentially in time for small initial separations and for the first 10 days. The large kurtosis values are a clear indication for non-local pair dispersion. Larger initial separations ($r_0 > 5$ km), however, are well described by the Richardson solution to the PDF and kurtosis. The kurtosis suggests that the pair separations are uncorrelated for pairs that are larger than 5 km which is a much smaller length scale than the dominant eddy size.

On the contrary, structure functions show a $r^{2/3}$ power law for separation distance below the deformation radius L_D suggesting a $k^{-5/3}$ energy spectrum and local dispersion (Table 2.2). The local character of the energy spectrum inferred from structure function also contains motions that do no affect pair dispersion like internal waves (Babiano et al., 1990). Even after filtering inertial oscillations with a low-pass filter, however, structure functions indicate a local regime and do not steepen significantly. This findings is different from results in the Gulf of Mexico (Beron-Vera and LaCasce, 2016), where the removal of near-inertial energy caused structure function to steepen from an apparent $r^{2/3}$ power law to a r^2 which is in line with the pair dispersion statistics.

The decomposition of structure functions indicates that motions are divergent at scales below 75 km and the ratio between divergent and rotational motions S_r / S_d is less than one. These divergent motions can be attributed to the internal wave field as well as to ageostrophic submesoscale flows that would have an energy spectrum of k^{-2} or shallower. However, the hypothesized transition from local to non-local dispersion at the submesoscale cannot be supported with the data available here. Neither the dispersion statistics (relative dispersion, diffusivity, FSLE, PDFs), nor the structure functions, seem to reflect a regime change at the mixed layer deformation radius estimated at 5-10 km. Pair dispersion statistics as well as structure functions consistently indicate a regime shift close to the deformation radius $L_D = 60$ km.

Energy at small scales that causes the structure function to indicate a local regime can likely not be explained by inertial oscillations, which begs the question as to which processes are responsible for the variability at those scales. We find that motions become increasingly divergent below the deformation radius and clearly deviate from two-dimensional, quasi-geostrophic dynamics below 20 km. The kurtosis supports this at scales above 5 km quickly fall to a value of 2 (as the Rayleigh asymptotic limit). The ratios between longitudinal and transverse structure functions, and between rotational and divergent structure functions, further suggest that those motions are weakly rotational; a property that applies to the internal wave continuum as well as to balanced dynamics that

have a considerable ageostrophic component.

2.4.2 Consequences of stochastic noise

While at global or basin scale, AVISO-advected drifters can reproduce observed relative dispersion, they are not sufficient to model dispersion on the regional scale, $\mathcal{O}(10)$ km. Our results suggest that the mesoscale circulation dominates pair dispersion and is therefore qualitatively captured by the AVISO-derived, geostrophic currents. However, small-scale perturbations, even if they are in the form of a simple first order stochastic model, drastically alter trajectories. The first-order stochastic trajectories are a better representation of the observed trajectories and can reproduce the long-time dispersive behavior in the relative dispersion and FSLE.

The first-order model implemented on the AVISO-advected trajectories has two primary effects, both of which are illuminating when interpreting the dispersion of observed drifters. First, diffusive growth tends to be faster than exponential spreading at early times. The dominant driver for pair separations is, thus, the uncorrelated motions due to the stochasticity in the velocity. This can most clearly be seen in the pair separation PDFs that resemble dispersion due to uncorrelated velocities (Figure 2-7), the diffusive growth of the relative dispersion (Figure 2-3) as well as the flattening of structure functions at the smallest scales. Second, random motion in a constant shear flow leads to a relative dispersion that grows like t^3. The added noise on the velocity of the stochastic drifters can cause them to disperse in a shear dispersion manner. Since the small-scale PDFs seem to indicate Rayleigh-type distributions but the relative dispersion and diffusivity suggest t^3 growth, shear dispersion is a likely candidate for the quick dispersion of the stochastic drifters.

While we show in this study that the removal of NIO does not significantly affect the steepness of structure function, supporting that NIO are not the only process contributing to the velocity variance at scales below 10 km, we do not show what the impact of the addition of NIO to the AVISO trajectories would be. (Beron-Vera and LaCasce, 2016), however, perform this analysis and get to the same result.

The subgrid-scale noise has an effect on scales much larger than the noise scale. In fact, FSLE and structure functions suggest that the stochastic noise affects drifter motions at scales up to 10 km. This scale can be identified by comparing the stochastic drifters with the AVISO drifters. Haza et al. (2014) found that uncertainty in the drifter position can affect the dispersion statistics at scales up 6 times the magnitude of the position error.

2.4.3 Limitations of the dataset

The results have to be interpreted taking into account the shortcomings of each metric and the limitations of the dataset itself. Since drifters were drogued at 15 m depth, mixed layers were possibly shallower than that during the first month (Hormann et al., 2016), and submesoscale turbulence decays away from the surface, we expect that the drifters measure less small-scale variability and steeper spectra than they would at the very surface. The fact that the drogue is deeper than the mixed layer, furthermore, reduces a bias due to surface wave motions, and most likely reduces the effect of convergent flow such as Langmuir circulation on the distribution of drifters. These convergent flows otherwise tend to align drifters and bias the regions they sample.

Additionally, a sampling bias occurs because of the choice of deployment site. Certain features in the flow are sampled more extensively, rather than a representative sampling of the velocity field. The release location causes drifters to be entrained in a cyclonic eddy for the first 10 days. During this period, drifters traveled as a coherent cluster, reducing the degrees of freedom of our statistics due to dependent pairs.

The energy at the mesoscale might also overshadow any coherent small-scale motion and result in a non-local dispersion. This has severe consequences when inferring the energy spectrum from dispersion statistics. Additionally, as our results suggest, there is a large uncertainty associated with the largest scales. Particularly at large scales, a limited number of drifters samples the mesoscale eddies, providing only a limited number of realizations.

2.5 Conclusion

The dispersion study presented here identifies a contradiction between pair dispersion statistics (relative dispersion, FSLE, pair separation PDFs) and an analysis of structure functions. Pair dispersion statistics consistently identify a non-local dispersion regime at scales below 20 km that is associated with an exponential rate of pair separation, and predicted by energy spectra that follow a k^{-3} behavior. Structure functions, however, and their decomposition, suggest a local regime at scales below the deformation radius, associated with a power law growth of pair separations and predicted by energy spectra that are $k^{-5/3}$ or flatter. This discrepancy can be explained by a) processes that contribute to the energy spectrum of a flow, but not significantly to the dispersion, or b) uncertainties at the smallest scales, such as uncertainties in the position data.

To answer the question we posed in the title, submesoscale flows are possible to observe from pair dispersion statistics, however, the interpretation of the data can be difficult due to the richness of processes occupying the same spatiotemporal band. In particular, we find that there are motions such as near-inertial oscillations and tides that affect the energy spectrum, but are inefficient at dispersion. Theoretical predictions for the submesoscale range, therefore, do not hold for the observed data. The limitations of our dataset further constrains our ability to resolve the submesoscale range.

Our findings are relevant when studying drifter dispersion at submeso-scales, especially in the presence of an energetic mesoscale circulation, as they question the ability of pair dispersion statistics to capture submesoscale flows. Alternatively, in a region of thin mixed layers, submesoscale flows could be inefficient at the dispersion of drifters as there is less available potential energy to be extracted by mixed layer instabilities.

The finding that relative dispersion in the submesoscale range is largely governed by mesoscale eddies can have two explanations: 1) The mesoscale circulation is too energetic, such that non-local dynamics dominate dispersion even at the smallest scales. 2) Submesoscale flows are inefficient at dispersion and their associated eddy diffusivity is small. The former is conceivable because drifters sample the flow at 15 m depth, which could mean that submesoscale flows are weaker than at the surface, particularly if mixed layers were shallow in general. The latter is subject to active debate because it is unclear if pure submesoscale dispersion has been observed in drifter pair dispersion. Both are difficult to separate because, at least conceptually, submesoscale flows are thought to be energized by frontogenesis by the mesoscale strain. This would imply that submesoscale are organized by the mesoscale flow in a way that they always occur in the regions of strongest non-local influence.

Since dispersion statistics are often not conclusive in inferring an energy spectrum from pair statistics, particularly at small scales, more information about the flow field is needed. Multiple drifter statistics and clusters can help to map velocity gradient properties to further characterize the kinematics of a flow field. Velocity gradient properties are especially important in submesoscale flows, where the local Rossby number becomes $\mathcal{O}(1)$. Analyses of groups and clusters of drifters have not been fully exploited in oceanography despite their potential, often due to a lack of suitable clustered experiments.

Chapter 3

HORIZONTAL DISPERSION IN SUBMESOSCALE VERTICAL SHEAR

Abstract

In the ocean, vertical velocity gradients can be orders of magnitude larger than horizontal velocity gradients. At surface submesoscale fronts, and in filaments, the vertical shear of the horizontal velocity is particularly large as it is largely in thermal wind balance with the lateral buoyancy gradient ∇b, which is continuously intensified by frontogenesis. As dye experiments and numerical simulations suggest, vertical shears are efficient at dispersing tracers. In fact, due to their large magnitude, vertical shears can be more potent at separating drifters than those due to lateral strain. Conventional, depth-keeping drifters, however, are not affected by vertical shear, as they are not separated vertically and, hence, will be ignorant of the associated dispersion. These findings suggest that depth-keeping drifters might underestimate the true, horizontal dispersion that Lagrangian fluid parcels experience in the mixed layer.

This chapter is in preparation for submission to Ocean Modeling with co-authors M Dever and A Mahadevan. SE performed the research and wrote the manuscript under the supervision of AM. MD developed the offline particle tracking code.

3.1 Introduction

Submesoscale currents in the ocean, occupying horizontal scales of $\mathcal{O}$(1-10 km), stir and disperse oceanic tracers, and provide a pathway for tracer variance to the dissipative scales (Thomas et al., 2008; McWilliams, 2016). Thriving in narrow regions around density gradients, submesoscale currents are known to strain out and elongate patches of tracers into streaks with horizontal widths of $\mathcal{O}$(0.1-1 km). These flows intensify tracer gradients and can thus lead to enhanced lateral mixing. Intricate spatial structure, such as sharp, elongated filaments, fronts, and spiraling eddies, are characteristic of submesoscale turbulence and can now be observed from satellites in temperature and chlorophyll imagery (Munk et al., 2000; McWilliams, 2016; Mahadevan, 2016).

The stirring of tracers can theoretically be understood by the velocity gradients acting on a distribution of tracer. The velocity gradients are conventionally expressed as the lateral strain, $\gamma = \sqrt{(u_x - v_y)^2 + (v_x + u_y)^2}$, and divergence, $\delta = u_x + v_y$, which are particularly large in submesoscale fronts and eddies where they often reach $\mathcal{O}$(f), with the Coriolis parameter f. The majority of elongation at submesoscales is likely caused by frontogenesis, a concept that describes the rapid intensification of tracer gradients owing to horizontal strain (Hoskins, 1982). In case of a non-diffusive, passive tracer, the magnitude of the tracer gradients grows exponentially fast, reaching a discontinuity in finite-time. The growth of gradients is then arrested by diffusivity at the smallest scales.

Pairs of drifters, afloat with a surface buoy and drogued at a fixed depth, sample lateral velocity differences that cause them to converge or separate. It has been shown, for example, that drifters accumulate quickly in regions of convergence (D'Asaro et al., 2018; Choi et al., 2017) and, therefore, sample these regions of the flow more frequently. Recently, drifter experiments showed that submesoscale currents modify the turbulent dispersion that would otherwise be controlled by the energetic, mesoscale circulation (Chapter 2, Poje et al., 2014). The energy spectra at submesoscales is still subject to active debate but often thought to follow approximately $E \sim k^{-2}$, where $k = (k_x^2 + k_y^2)^{1/2}$ is the horizontal wavenumber. This less red energy spectrum alters the character of turbulent dispersion of pairs of drifters, such that eddies of the same size as the pair separations dominate the dispersion, rather than the largest, most energetic eddies (see Chapter 2).

Since submesoscale currents are energized by frontogenetic processes (Hoskins, 1982; Stone, 1966), which intensify lateral buoyancy gradients at the surface, $M^2 = |\nabla_H b|^2$, their kinetic energy is typically surface-intensified and decays exponentially with depth

below the mixed layer (ML) (Thomas et al., 2008; McWilliams, 2016). In thermal wind balance, the lateral buoyancy gradient is balanced by a vertical shear of the horizontal velocity $S = \mathbf{u}_z$, but, since the Rossby number $R_0 = \zeta/f$ is order one at submesoscales, ageostrophic motions make a non-negligible contribution (Pedlosky, 1987). For this reason, in submesoscale flows, the vertical shear S can be two orders of magnitude larger than the horizontal strain γ and locally exceeds $\mathcal{O}(100\ f)$, equivalent to a rapid change in velocity $\Delta\mathbf{u}$ of 0.1 m/s over 10 m depth. It has been suggested that vertical shear becomes particularly important in submesoscale filaments and eddies (Lapeyre and Klein, 2006a), where it may become the largest term responsible for the spreading of tracers.

Previously, dye experiments revealed that vertical shear plays an essential role in the dispersion of tracers (e.g., Sundermeyer and Ledwell, 2001). An important consequence of this vertical shearing mechanism is that vertical tracer gradients intensify and, thus, the effective vertical diffusivity increases (Taylor, 1953). So-called shear dispersion, as first described by Taylor (1953) in laminar pipe flow, has also been observed in the ocean (e.g., Sundermeyer and Ledwell, 2001; Steinbuck et al., 2011). Since the largest vertical shears in the ocean are in oscillatory currents, shear dispersion has mostly been discussed for tides and near-inertial waves (e.g., Young et al., 1982). Furthermore, only a few studies have suggested that sheared currents in the ocean can also enhance the horizontal diffusivity in a similar way (Bowden, 1965; Okubo, 1971, 1968).

While turbulent dispersion has been studied extensively in the ocean, a Lagrangian perspective on drifter dispersion due to vertically-sheared currents is largely undocumented, in particular, because the depth-keeping drifter design prohibits vertical separation (e.g., Davis, 1991; LaCasce, 2008). Using subsurface floats at about 1000 m depth, LaCasce and Bower (2000) conclude that diffusivity due to the mesoscale vertical shear is small compared to the horizontal eddy diffusivity generated by the mesoscale circulation. While this study focuses on the mesoscale circulation at depth, it contrasts more recent numerical simulations in the surface ocean by Lanotte et al. (2016) suggesting that, if submesoscale vertical shear is resolved, it can significantly affect the dispersion statistics inferred from drifters, such as relative dispersion and finite-scale Lyapunov exponents.

If we define relative dispersion as the separation of two neighboring drifters subject to the ocean currents $D^2 = \langle r^2 \rangle$ (e.g., LaCasce, 2008), it will be affected by both the vertical and horizontal velocity gradients. Considering that relative velocities between drifters due to vertical shear can be orders of magnitude larger than due to the horizontal strain, it is conceivable that sheared velocities have a significant influence on relative dispersion, partic-

ularly in submesoscale flows for the reasons stated above. Vertically-separated drifters, just like continuous concentrations of dye, are subject to differential advection by the currents at different depth, and, therefore, separate faster than horizontally-separated drifters. This hypothesis has significant consequences, particularly when assuming that drifter-derived relative diffusivity is used as an estimate for Lagrangian diffusivity. If particles are permitted to move vertically, they will separate vertically, and, consequently, be affected by the vertical shear of the velocity. Horizontal diffusivity sampled by depth-keeping drifters will therefore likely underestimate the horizontal diffusivity that three-dimensional fluid parcels experience. The goal of this study is to characterize how vertical shear impacts the horizontal dispersion of drifters, assuming that they are vertically separated, and to examine if vertical shear introduces bias in horizontal dispersion estimates from depth-keeping drifters. To address the hypothesis, we contrast dispersion of horizontally-separated drifter pairs with vertically-separated drifter pairs. Drifter behavior is simulated by conducting particle-tracking experiments in the submesoscale-resolving Process Study Ocean Model (PSOM Mahadevan et al., 1996a,b). These idealized numerical simulations are characterized by active submesoscale turbulence in a shallow, energetic mixed layer that develops strong front region with large vorticity ζ, lateral strain γ, and vertical shear S. Synthetic drifters mimicking real drifters are deployed at fixed depths and only advected using horizontal velocities.

This chapter is structured as follows. In section 3.2 and 3.3, we introduce the numerical model and the offline particle-tracking code used to calculate drifter trajectories. Characteristics of the numerical simulation are presented in section 3.4, with an emphasis on the vertical shear and horizontal strain of the horizontal velocity. In section 3.5, we quantify the impact of vertical shear on dispersion using vertically-separated pairs of drifters. The role of submesoscale filaments and eddies is examined in section 3.6. Finally, a summary and conclusion are offered in section 3.7.

3.2 Numerical model

3.2.1 Process Study Ocean Model (PSOM).

A three-dimensional ocean model (Mahadevan et al., 1996a,b) was used to simulate a fully developed submesoscale eddy field [1]. This model has been used extensively in studies of submesoscale processes in the mixed layer (Badin et al., 2011; Jaeger and Mahadevan, 2018;

[1]The Process Study Ocean Model (PSOM) is available at `www.github.com/PSOM/V1.0.git`.

Mahadevan et al., 2012). It has been shown to generate good estimates of vertical velocity (e.g., Mahadevan and Tandon, 2006) and was used to study the import of nutrients into the mixed layer, as well as the export of carbon below the mixed layer (e.g., Omand et al., 2015; Mahadevan, 2016) .

The non-hydrostatic Boussinesq equations are solved in a 192×320 km horizontal domain set up in a channel configuration with periodic boundaries in the zonal x-direction and no-slip boundary conditions in meridional y-direction. The horizontal grid is rectangular with a resolution of $\Delta x = \Delta y = 1$ km, whereas the vertical grid is stretched in 48 layers with higher resolution in the uppermost cells (about 1 m) and lower resolution at depth (about 50 m). In order to allow for mesoscale structures to develop and avoid bottom boundary effects, the domain is 1000 m deep with a flat bottom. We use a constant horizontal diffusivity of $\kappa_h = 1\ m^2/s$; the vertical diffusivity κ_v is constant and equal to κ_h in the mixed layer and linearly decreasing below.

3.2.2 Model setup.

The model is initialized with a temperature and a salinity section measured by an Underway CTD (UCTD) in the Bay of Bengal in 2013 (Figure 3-1). The initial condition sets up a meridional buoyancy gradient with lighter water in the north and denser water in the south of the domain. Additionally, the UCTD section captures multiple strong density fronts with lateral buoyancy gradients of $\mathcal{O}(10^{-6}\ \mathrm{s}^{-2})$ superposed on the large-scale, meridional buoyancy gradient. The water column is capped by a shallow, mixed layer (MLD $\sim$ 20 m) that is separated from the interior by a strong pycnocline ($N^2 \sim 10^{-6}\ \mathrm{s}^{-2}$). The first baroclinic Rossby radius of deformation in the mixed layer is therefore on the order of $\sim$ 60 km, about a third of the model domain's width.

The simulation is forced with a realistic, uniform wind stress and heat flux measured at a mooring located at 18°N in the Bay of Bengal. The heat flux is low-pass filtered to remove the diurnal cycle and is predominantly positive throughout the duration of the simulation. We apply an artificial, sinusoidal, meridionally-varying heat flux anomaly in order to preserve the large-scale density gradient. The meridional heat flux anomaly integrates to zero across the domain and has an amplitude of 15 Wm^{-2}. The wind stress is in south-west direction and has a component in the negative along-front direction. The resulting Ekman buoyancy flux is expected to further destabilize the mixed layer. Ekman transport at the solid boundaries leads to upwelling and downwelling and is a potential mechanism for surface convergence and vertical velocity.

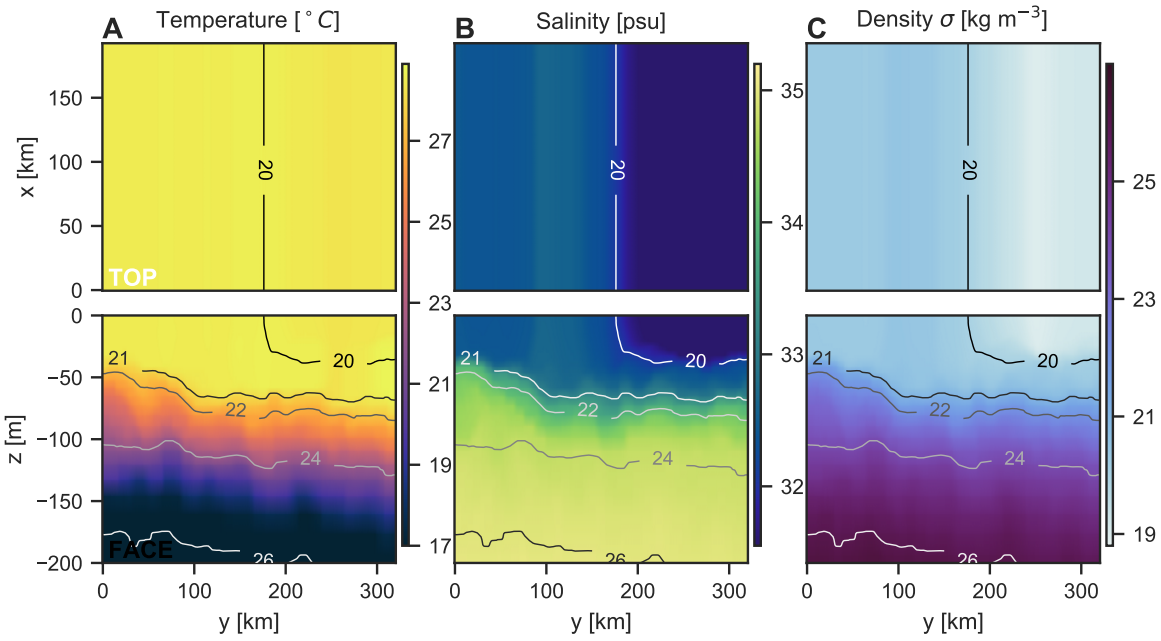

Figure 3-1: Zonally-homogeneous initial conditions generated from an Underway CTD section. The upper row of each panel shows the top view of the three-dimensional model domain (x,y-plane), the lower row shows the front face of the domain (y,z-plane). Temperature (A), salinity (B), and density anomaly, $\sigma = \rho - \rho_0$ from the reference density $\rho_0 = 1027 kg/m^3$, (C) are shown in color. Contours denote surfaces of constant density anomaly.

The simulation is spun up for 50 days from the initial condition until the total kinetic energy integrated over the model domain as well as the average mixed layer depth stabilize. We choose a 20-day period during which kinetic energy and mixed layer depth remain relatively constant to conduct the Lagrangian particle tracking experiments.

3.3 Offline particle tracking

3.3.1 Particle advection.

An offline particle tracking code was developed to integrate the particle position forward in time using the three-dimensional velocity field from the numerical model [2]. It is inspired by the algorithm used in TRACMASS (Döös et al., 2013) but custom-built for model output generated with PSOM.

The velocity at the particle position x can we written as a linear interpolation between the model velocity at the western, u_{i-1}, and eastern, u_i, walls of the associated grid cell

[2]The offline particle tracking code is available at `www.github.com/sessink/offline_particle_tracking.git`.

(Döös et al., 2013):

$$u(x) = u_{i-1} + \frac{(x - x_{i-1})}{\Delta x}(u_i - u_{i-1}). \tag{3.1}$$

where $\Delta x = (x_i - x_{i-1})$. Defining the parameters $\beta = (u_i - u_{i-1})/\Delta x$ and $\delta = -u_{i-1} - \beta x_{i-1}$ (Döös et al., 2013), (3.1) can be rewritten as the following ordinary differential equation:

$$\frac{\partial x}{\partial t} + \beta x + \delta = 0 \tag{3.2}$$

where $\beta \neq 0$. This differential equation has a known analytical solution that takes the form

$$x_{t_1} = \left(x_{t_0} + \frac{\delta}{\beta}\right) \exp^{-\beta(t_1 - t_0)} - \frac{\delta}{\beta}. \tag{3.3}$$

By replacing the positions of the cell walls for x_{t_1} and solving 3.3 for t_1, we evaluate the time it would take for the particle to travel to either of the six grid cell walls. If this time t_1 is shorter than the advective time step, the particle is advected for a sub-time step t_1, and the procedure is repeated with the adjacent grid cells until the particle has been advected for the full advective time step. Analogous to the two-dimensional problem, we can solve for the new position in a three-dimensional model domain.

While this implementation is in low-resolution with residuals scaling like $\mathcal{O}(\delta$ x), it has the advantage of being analytically solvable. Therefore, it is possible to integrate the trajectories in forward and backwards time, leading to complete reversibility within a small margin of uncertainty.

We step the particles forward with an advective time step of 15 min, which is well-below the temporal resolution of the model output (3 hours), and comparable to the temporal resolution that contemporary drifters are able to provide. Since the model fields are interpolated linearly in time, trajectories will be smooth and linear below 3 hours. In this implementation, we do not account for subgrid effect acting on the trajectories which tend to have a strong impact from what we have found in Chapter 2. The model velocity, however, is not purely advective and includes a velocity associated with the model diffusivity. A constant particle diffusivity is equivalent to a random walk with constant step length.

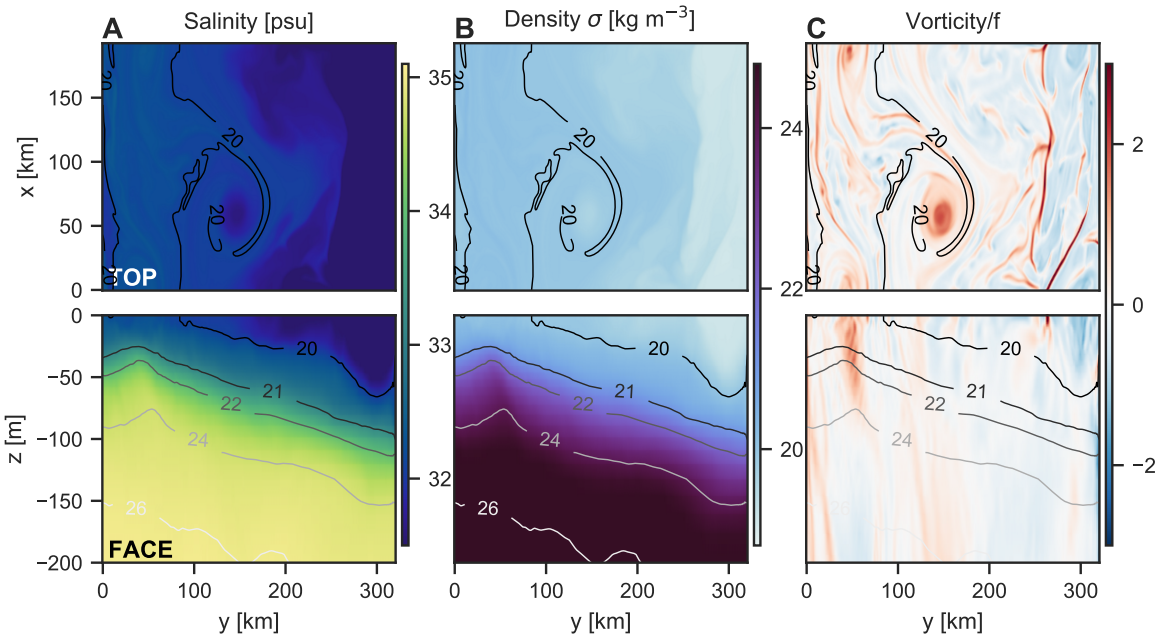

Figure 3-2: Fully spun-up model simulation after 50 days showing A) salinity, B) density, C) vorticity ζ normalized by the Coriolis parameter f. The upper row of each panel shows the top view of the three-dimensional model domain (x-y plane), the lower row shows the front face of the domain (y-z plane). Only the upper 200 m of the domain are shown.

3.4 Model results

3.4.1 Model spin-up.

The model spins up from the initial condition until lateral buoyancy gradients are approximately in thermal wind balance with the vertical shear. The flow is to good approximation geostrophic, with a mean geostrophic jet in y-direction. Frontogenesis intensifies lateral buoyancy gradients which accelerate the geostrophic flow, which eventually become unstable to a range of instabilities, most prominently mixed layer baroclinic instability. The instabilities break up the front into baroclinic eddies which merge until the maximum eddy wavelength is reached, approximately corresponding to 1/3 of the model domain size in the y-direction ($\sim$100 km; Figure 3-2). As frontogenesis continues to act on density gradients, energetic jets along filaments and strong vorticity structures, $\frac{\zeta}{f} > 1$ are generated that last for multiple days in the simulations.

3.4.2 Horizontal and vertical shear.

Figure 3-3 shows the vertical structure of horizontal shear and strain, vertical shear, and lateral buoyancy gradients in the upper 200 m of the water column. It is striking that the

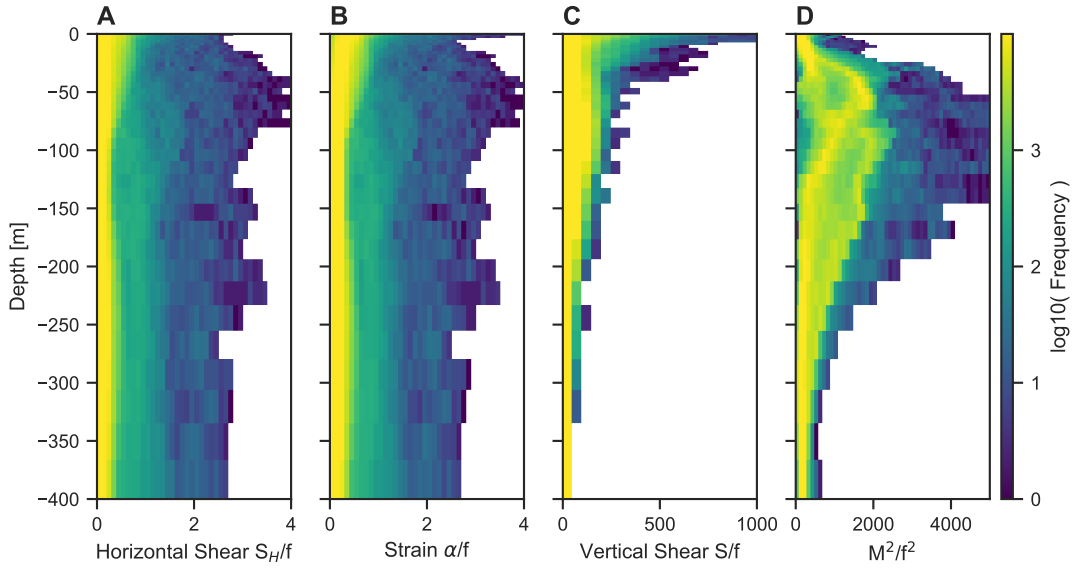

Figure 3-3: Histograms of the model fields as a function of depth showing A) the horizontal shear S_H and B) the lateral strain α, C) the vertical shear S of the horizontal velocity and D) the lateral buoyancy gradients M^2. All variables are normalized by the Coriolis parameter f. The colors indicate the frequency of occurrence.

vertical shear S is two orders of magnitude larger than the horizontal shear S_H and strain γ, which are both $\mathcal{O}$(f). S_H and γ behave similarly, suggesting that γ is mostly controlled by shear. γ decays with with depth, particularly below the shallow mixed layer of $\mathcal{O}$(10 m), however, not as rapidly as the vertical shear S. The largest vertical shears are found near the surface and throughout the mixed layer. Although lateral buoyancy gradient M^2 are expected to be uniform across the mixed layer, they do not seem to balance the large values of vertical shear, suggesting that ageostrophic motions play a role in setting the magnitude of S. The magnitude and vertical structure of the vertical shear generated by the model is comparable to observations reported in Ramachandran et al. (2018) that are based on ADCP measurements in a neighboring region in the Bay of Bengal.

Furthermore, in horizontal maps of the surface, it is evident that vertical shear as well as lateral strain is concentrated in regions of strong vorticity $|\zeta|$ and aligns with ridges in the lateral buoyancy gradients M^2 (Figure 3-4). This is expected since fronts and filaments are largely in thermal wind balance and associated with strong frontal jets. In filaments, the vorticity reaches $\mathcal{O}$(3f), lateral strain of $\mathcal{O}$(f), and vertical shear of $\mathcal{O}$(300f). This is reflected more quantitatively by the fact that the root mean square values are one order of magnitude larger than the mean values. In regions where the vertical shear S is larger than

M^2/f^2, we expect a deviation from geostrophic dynamics. Since in filaments the Rossby number $R_0 > 1$, it is likely that rotation loses influence.

By performing a linear regression between the vertical shear S and the lateral buoyancy gradients M^2, we test to which degree buoyancy gradients are in thermal wind balance. In thermal wind balance, it is expected that those relate such that $\partial_z \mathbf{u} \sim \nabla_H b/\mathrm{f}$. At the very surface, vertical shear exceeds the thermal wind prediction and has a significant ageostrophic component of about 5-15%. At depth, as expected, the vertical shear is in thermal wind balance. The horizontal strain is correlated with the vertical vorticity. The horizontal shear has a component attributed to the vertical component of vorticity ζ. The largest values in the horizontal strain γ, therefore, coincide with large values of ζ.

3.5 Vertically and horizontally separated drifters

In the spun-up model simulation (see Section 3.2), we release 20,000 drifters at four different depths: At the near-surface (1 m), within the mixed layer (5 and 15 m), and below the mixed-layer depth (50 m; Figure 3-5). At each depth, initially, drifters are uniformly distributed but drifters at different depths are exactly co-located horizontally.

As expected in this surface-intensified flow field, drifters at the surface move faster than drifters at depth (Figure 3-5). The mean speed is approximately 0.8 ms^{-1} at 1 m depth and 0.6 ms^{-1} at 15 m depth. The fastest velocities are at the center of the jet, which is approximately in the region of the largest meridional buoyancy gradient (see Figure 3-2).

Furthermore, small-scale velocity variability is more prominent in the surface than at depth, since larger horizontal feature decay more slowly with depth. As a consequence (Figure 3-5), the drifters are stirred by eddies more effectively at the surface, such that groups of drifter wrap around eddies or get strained out along filaments. The deepest drifters (at 50 m depth) travel as a continuous cloud throughout the first 5 days. As time progressed, after about 14 days (Figure 3-5C), drifters are clearly forming elongated structures that tend to become more concentrated and linear. These linear structure can be an effect of both the lateral strain γ as well as the horizontal divergence δ as observationally described in D'Asaro et al. (2018).

It is worth noting that drifters at different depth seem to sample the same features, although at different intervals after the release. This suggests the validity of the frozen turbulence hypothesis and the possibility that the relative diffusivity of drifters at different levels might not vary significantly.

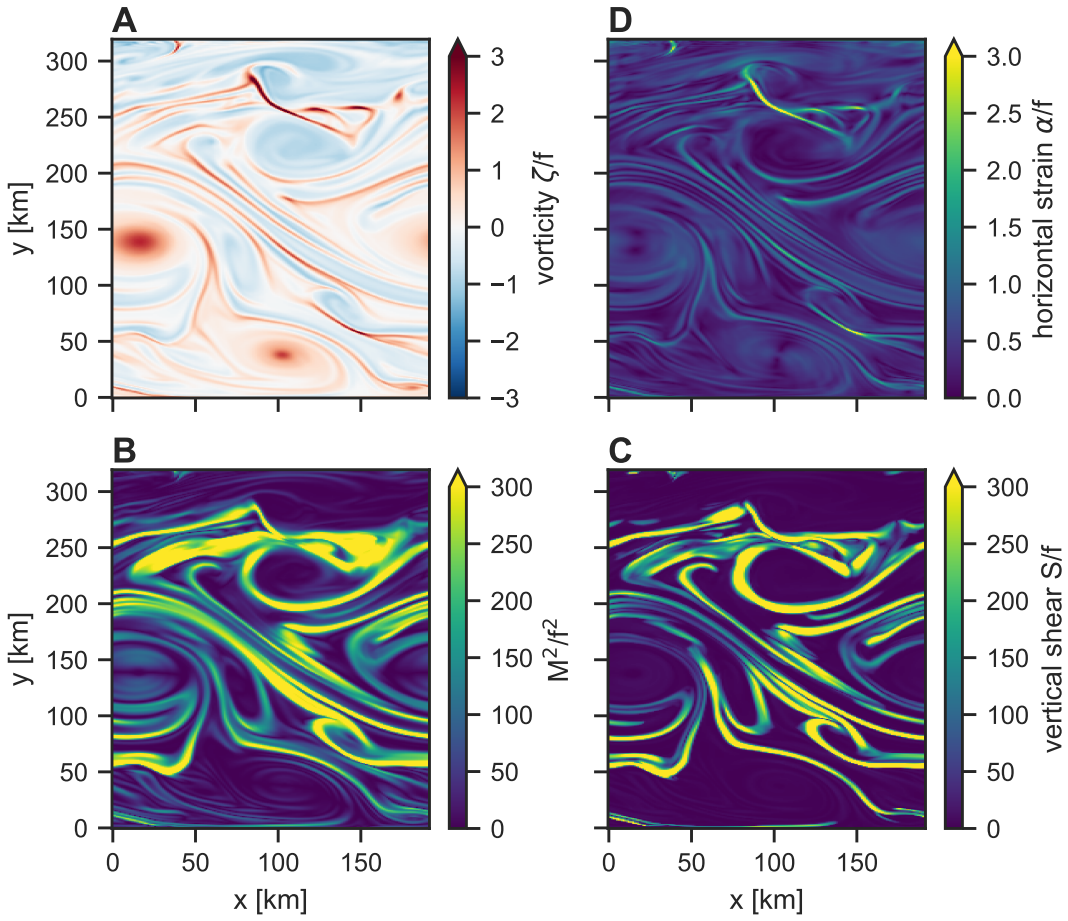

Figure 3-4: Surface snapshot of (A) vertical component of the relative vorticity, $\zeta = k \cdot \nabla \times \mathbf{u} = v_x - u_y$, normalized by the Coriolis parameter f, (B) the lateral buoyancy gradient M^2 normalized by f^2, (C) the vertical shear S normalized by f, and (D) the horizontal shear S_H normalized by f.

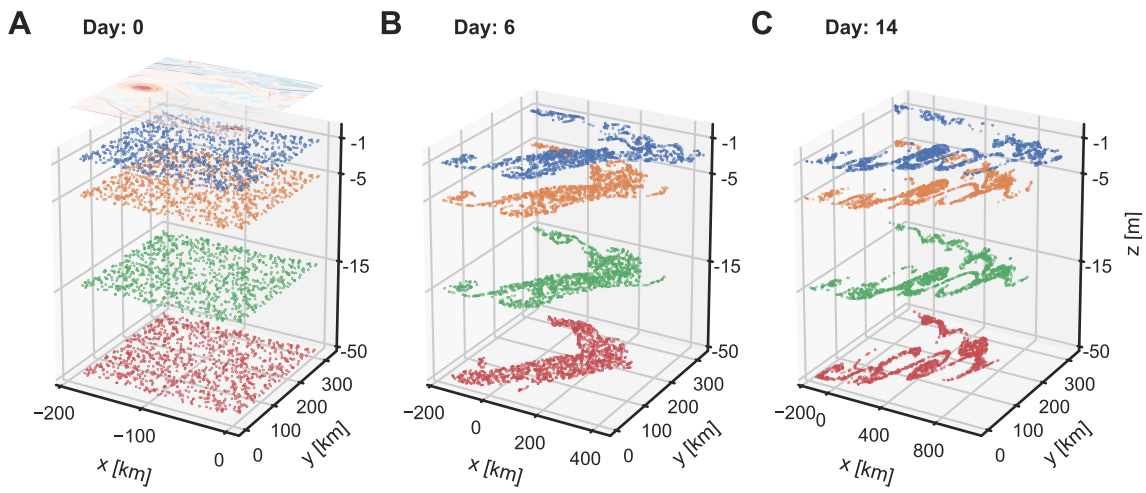

Figure 3-5: Three-dimensional rendering of the initial particle seeding at $t = 0d$ (A) and snapshots of the particle positions at $t = 6d$ (B), and $t = 14d$ (C). Model fields of density and vorticity are overlaid. Three horizontal sheets of randomly distributed pairs are laid down at four different depth: a) 1 m, b) 5 m, c) 15 m, and d) 50 m. The first two sheets are located within the mixed layer, the third one is located below the mixed layer.

By contrasting two groups of drifter pairs that 1) have a vertical separation, from now on labeled vertical pairs, and 2) pairs that no vertical separation, from now on labeled horizontal pairs, we investigate how the vertical shear S affects horizontal pair dispersion of drifters and how important S is compared to horizontal strain α. In each of the following analyses, we compare how the pair dispersion of these two groups behaves. While vertical pairs will develop a horizontal separation, neither of the two groups of drifters will change their vertical separation.

Horizontal pairs are initially separated by a horizontal distance only ($r_x = 0.25$ km and $r_z = 0$). This initialization mimics how drifters in the ocean are deployed and pair dispersion estimates are expected to compare with the observations and theory laid out for drifters in two dimensions. Due to the model resolution, if pair separations are smaller than the grid scale Δx =1 km, the relative velocity between drifters varies linearly with separation distance, which is a result of the linear interpolation of the velocity field within a grid cell.

Vertical pairs are initially separated by a vertical distance only ($r_x = 0$ km and $r_z \neq 0$). These pairs are formed using drifters that are in the same horizontal position, but separated by a vertical distance r_z. The initial pair separation distances r are, hence, set by the vertical spacing between the release depths; for example, the vertical distance between the first two uppermost depth, (z_i, z_j) = (1 m,5 m), will be 4 m and similarly for the other depths.

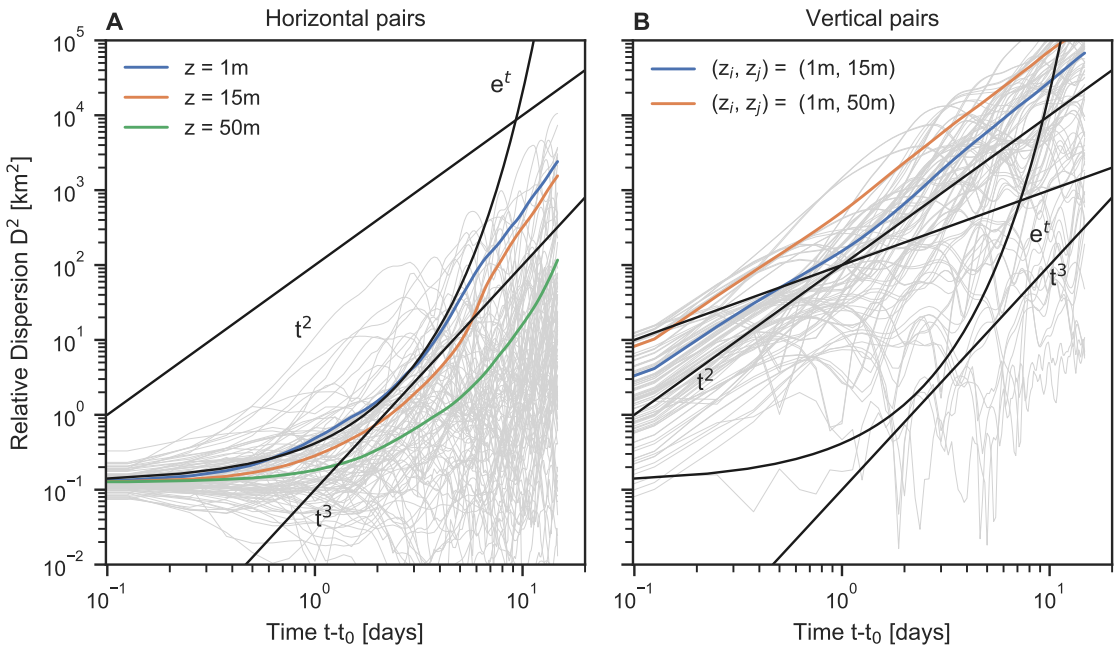

Figure 3-6: Relative dispersion D^2 for the horizontally-separated pairs released at four different depths (A) and the vertically-separated pairs released with three different vertical separations r_z (B). The individual squared separations r^2 are shown in gray in the background. Black guidelines indicate the different theoretical functional forms: the ballistic regime ($\sim t^2$), the Richardson regime ($\sim t^3$), and the non-local regime ($\sim e^t$)

Since turbulent flows have the property of separating neighboring fluid parcels on average that originate in approximately the same location, the separation of pairs of drifters implies the stirring of two neighboring water masses. A common metric to capture this is the relative dispersion, defined as $D^2(t) = \langle(\mathbf{x_i} - \mathbf{x_j})^2\rangle$, where $\langle\cdot\rangle$ denotes the ensemble average over pairs with the same origin (or equivalently, with a small initial separation). A closely related quantity is the relative diffusivity, $\kappa_{rel} = \frac{1}{2}\frac{dD^2}{dt}$, which can be understood as an effective eddy diffusivity that spreads out a group of drifters.

The relative dispersion of horizontal pairs grows exponentially in time for the first 5 days and transition to approximately a power law of three (Figure 3-6). The exponential growth is expected when the largest eddies in the domain dominate the spreading of pairs in a so-called non-local regimes. The associated energy spectra, $E \sim k^{-\alpha}$, are steep, with spectral slopes of $\alpha > 3$. The cubic growth is reminiscent of a Richardson regime in energy-cascading inertial range, where pairs separate mainly due to the stirring of eddies that are of the same size as the separation. Cubic growth, however, can also be generated by random motion in a large-scale shear.

The vertical pairs behave differently (Figure 3-6) and produce a relative dispersion

that is about one order of magnitude larger than for the horizontal pairs. Furthermore, the relative dispersion of vertical pairs follows a t^2 power law for the first 10 days which is suggestive of a super-diffusive dispersion or ballistic dispersion. The ballistic regime occurs when the pair velocities are strongly correlated and are usually (in horizontal, observational data) only found in the first few hours after deployment (e.g., LaCasce, 2008).

The ballistic regime here is a result of the vertical shear in the horizontal velocity Δv that remains correlated within the mixed layer. As the pair separation r is increased by the velocity difference between the two layers, their squared separations grow like $r^2 \sim (t\Delta v)^2$, where $Deltav$ is the velocity difference between particles at two different depths.

The velocity difference between two particles is what determines their separation. The relative dispersion curves, therefore, scales like Δv^2, so that a greater shear is reflected in a larger magnitude of the curve on a log-log scale. For the two depth ranges plotted in Figure 3-6B, this vertical shear is $\mathcal{O}(10^{-2}\ s^{-1})$. Interestingly, this value is larger than the spatial mean shear $\int S dA$, where A is the horizontal area of the model domain. The vertical shear associated with the ballistic relative dispersion is closer to the rms shear, $\mathcal{O}(10^{-1}\ s^{-1})$, which includes the spatial mean and standard deviation, and accentuates the role that outliers play in the distribution of vertical shear.

3.6 Impact of submesoscale filaments

In the previous section, we showed that the vertical shear enhances horizontal pair dispersion (Figure 3-6) and ballistic spreading overpowers turbulent dispersion for the vertical pairs. This section aims to identify the role that energetic filaments and eddies play for the dispersion as the ballistic regime above could not be explained by the spatial mean shear.

Submesoscale currents are often narrow jets, largely in geostrophic balance, that are associated with lateral buoyancy gradients M^2. As shown in Section 3.4, largely due to the thermal wind relationship, the vertical shear is large at fronts and filaments and aligns with ridges of the lateral buoyancy gradient (Figure 3-4). Ageostrophic components further increase the shear in the mixed layer, where it reaches maximum values of $\mathcal{O}(100\ f)$ (Figure 3-3).

The frontal regions of the flow, which can be eddies or filaments, are hot spots for dispersion because their strong jet-like currents are able to separate pairs of particles

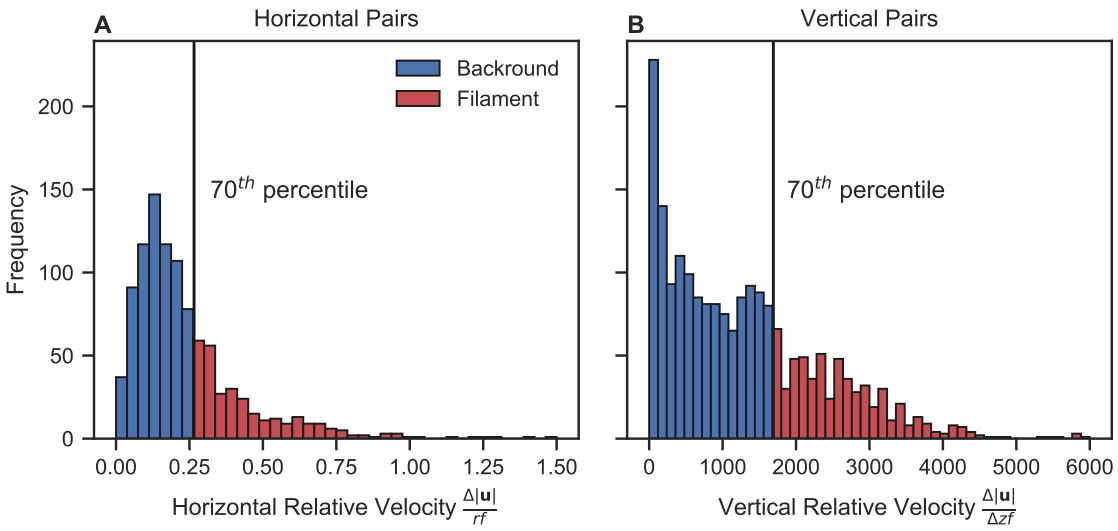

Figure 3-7: Categorization into pairs in filaments and the background. Horizontal pairs (A) are separated based on the horizontal velocity differences between drifters, vertical pairs (B) are separated based on the vertical velocity differences. The 70th percentile is used as the threshold value in both cases.

quickly. Both horizontal and vertical shear are increased in those regions compared to their spatial mean, but since the vertical shear is generally much larger than the horizontal shear and strain, we expect vertical shear to separate vertical pairs in a rapid ballistic way like described above.

To investigate the role that frontal regions play in the dispersion, we categorize vertical pairs based on the vertical shear S at their location three days after their release (Figure 3-7) and separate the set of drifters into drifters in filaments (S larger than 70th percentile) and drifters outside of filaments in the background (S smaller than 70th percentile). We chose the 70th percentile as a compromise between capturing the most intense shear and retaining enough pairs per category. Vertical shear S is used as a proxy for the vicinity of a frontal jet, assuming that the maximum shear will be close to the largest lateral buoyancy gradient.

The relative velocity between two drifters is ultimately what separates them. Velocity structure functions, $\langle (u_i - u_j)^2 \rangle$, are a way to describe the magnitude of relative velocity as a function of separation (Figure 3-8). The structure functions for the horizontal pairs in Figure 3-8A depend on separations like a r^2 power law indicating a non-local energy spectrum. The structure functions are thus dominated by the largest scales. For the vertical pairs in Figure 3-8B, however, structure functions show a 4/3-dependence on separation, which is close to the theoretical expectation for structure functions in frontogenesis r^1.

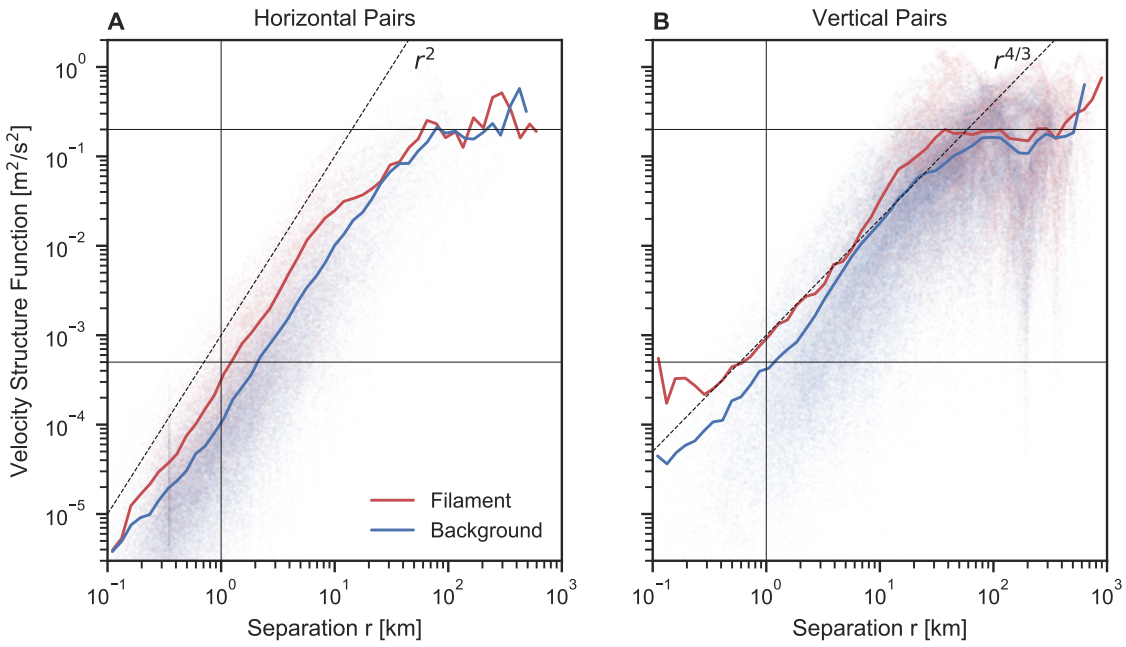

Figure 3-8: Second-order velocity structure function computed from horizontal (A) and vertical (B) pairs of drifters. Red curves indicate pairs in filaments, blue curves indicate pairs in the background. Individual data points a shown in the background. Guidelines are shown to visualize power laws dependencies.

Figure 3-9 shows that for both, the horizontally-separated pairs and the vertically-separated pairs, the relative dispersion is larger for pairs released in filaments. The magnitude of the difference is most pronounced at early times with t<5 days. In case of the horizontal pairs, we find an exponential growth of pair separations for the first 5 days. This is in agreement with the 2-power law structure functions in Figure 3-8A and suggests non-local relative dispersion. After approximately 5 days, the dispersion regimes shifts and resembles a t^3 power law. In case of the vertical pairs, pairs in filaments follow a t^2 dependence which we identified above as a characteristic of dispersion by the vertically-sheared currents. The background pairs grow more slowly up to about 5 days. The difference between filament and background pairs is less pronounced in case of the horizontal pairs. This might be due to the fact that the magnitude of horizontal shear is much smaller than vertical shear, such that pairs are separated less efficiently even when located in a filament.

It has previously described that drifters that are released in submesoscale flow are likely to be attracted to convergent regions and quickly align with the lateral buoyancy gradient (D'Asaro et al., 2018; Choi et al., 2017). As drifters and material move into

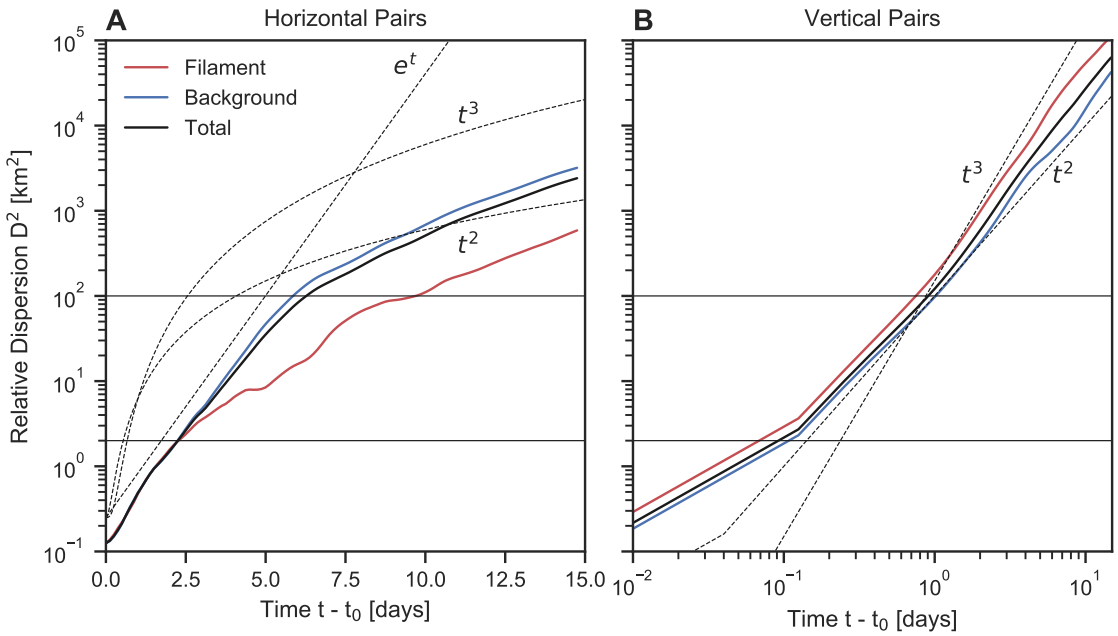

Figure 3-9: Relative dispersion of horizontal pairs (A) and vertical pairs (B). Red curves include pairs in filaments, blue curves include pairs in the background, black curves include all pairs. Black guidelines indicate the different theoretical functional forms: the ballistic regime ($\sim t^2$), the Richardson regime ($\sim t^3$), and the non-local regime ($\sim e^t$)

convergent regions, they are more likely to be sheared and strained by the vertical shear. It is conceivable that convergences therefore self-intensify the role that fronts and filaments play for the horizontal dispersion.

Since filaments are often surface intensified, these results are strongly dependent on the different depth of the drifters. In general, the larger the vertical separation between drifters, the larger the velocity difference, and the relative dispersion.

3.7 Summary and Conclusions

In this study, we have examined the impact of vertical shear of the horizontal velocity on the horizontal pair dispersion of semi-Lagrangian drifters. Although vertical shear is known to be essential for tracer dispersion (e.g., Young et al., 1982), few studies address the impact on Lagrangian dispersion, likely due to the surface-trapped design of drifters. For this purpose, we released two-dimensional, numerical drifters in a fully developed submesoscale eddy field and tracked their dispersion characteristics.

We find that vertically-separated drifters have an increased relative dispersion compared to pairs that only have horizontal separation. The increase can be attributed to the

velocity difference associated with the vertical structure of the velocity. The efficiency of this effect on vertically-separated drifters depends on the location in the water column. The magnitude of the vertical difference between two droguing depths is generally largest at the surface, where velocity magnitude as well as vertical decay are maximum.

Furthermore, we find that vertically-separated drifters separate in a ballistic manner with quadratic growth in time. This ballistic behavior outperforms the relative dispersion by the horizontal strain, particularly at small separations and early times, and leads to the fact that vertically separated pairs reach the long-term dispersive limit faster than horizontally separated shear. In the presence of vertical shear, turbulent dispersion regimes that would otherwise be expected due to the horizontal velocity field can not be observed. After about 10 days, it is expected that the vertical shear loses control and horizontal velocity gradients prevail. In our 15 day simulation, this hypothesis cannot be tested sufficiently.

The ballistic spreading of drifters can be thought of as a reversible straining of pairs of particles that, only in concert with vertical mixing, acts like shear dispersion in the sense of Taylor (1953). The vertical shear, therefore, actively contributes to the horizontal straining of a patch of tracer that can then be mixed vertically efficiently.

Submesoscale fronts and filaments are hot spots for this enhancement of horizontal dispersion because vertical shears become $\mathcal{O}(100\ f)$, where buoyancy gradients M^2 are sharp. The vertical shear in filaments and eddies is much larger than the background and can be identified as the driving force for the enhanced relative dispersion. We show that drifters that are released within a strong flow structure are likely to disperse ballistically with larger dispersion than drifters that are released outside of those regions. Drifters that are released in filaments, tend to stay in them for multiple days, likely reinforced by potential horizontal divergence that can be observed in the vicinity of density fronts.

Our findings suggest that depth-keeping drifters will likely underestimate horizontal dispersion of Lagrangian fluid parcels in the ML, since they miss the dispersion due to vertical shear. Unless the upper oceans turbulence can be represented accurately, it remains elusive to predict three-dimensional trajectories and the vertical shear impact on their dispersion. This result has important implications for the estimation of horizontal diffusivity and prediction of tracer spreading, particularly, because many quantities of interest, such as pollutants, nutrients, and organisms, are not buoyant. This study confirms that three-dimensional Lagrangian sampling strategies are necessary when studying processes in the oceanic mixed layer.

Since the vertical shear depends strongly on the dynamics of the upper ocean, the results presented here are specific to the model implementation based on observations from the Bay of Bengal and initialized with the specific UCTD section measured in 2015. The shallow mixed layers and energetic submesoscale turbulence that resulted from growing frontal instabilities are the major contributors to large vertical shear. It remains to be investigated, how the results change in a set of model simulations, in which mixed layer parameters like the mixed layer depth, lateral buoyancy gradients, and vertical mixing are systematically varied.

The logical extension of this problem is to track particles in three dimensions and compare their behavior with their two-dimensional counterparts. The difficulty with three-dimensional tracking, however, is to accurately predict the vertical velocity in the mixed. In the mixed layer, a variety of processes generate vertical velocity, often at horizontal and vertical scales that are difficult to resolve, such as convective and symmetric instability, wind driven mixing, and Langmuir turbulent. In the absence of these physics, which are likely dominant sources for vertical velocity, we are not able to predict three-dimensional particle trajectories.

Chapter 4

STATISTICS OF SUBMESOSCALE VELOCITY GRADIENTS FROM CLUSTERS OF DRIFTERS

Abstract

The velocity gradients describe the deformation and rotation of a fluid parcel. However, velocity gradients can become large in submesoscale dynamics, typically at length scales of $\mathcal{O}$(0.1-10 km), where the Rossby number, R_0, becomes $\mathcal{O}$(1). In the past, clusters of drifters have been used to estimate the two-dimensional velocity gradients of the surface oceanic flow field, but the results are prone to error and difficult to interpret. Here, we first use modeled drifters to evaluate 3 methods for estimating velocity gradients and systematically identify the sources of error, which are dominated by the geometry of drifter clusters. We then apply the most robust method to a drifter dataset from the Bay of Bengal. During the first three days of the drifter release experiment, we can identify submesoscale signatures in the velocity gradients, with vorticity, divergence, and strain of $\mathcal{O}$(f). The drifter cluster deformations are dominated by normal strain when the strain angle aligns with the direction of cluster stretching and the horizontal density gradients. Understanding the shortcomings of estimating velocity gradients from Lagrangian observations is crucial for designing future drifter experiments, particularly for observing two-dimensional divergence and vorticity in submesoscale flows.

This chapter is in preparation for submission to Journal of Geophysical Research with co-authors V Hormann, LH Centurioni and A Mahadevan. SE performed the research and wrote the manuscript under the supervision of AM. VH and LC planned and collected the drifter data.

4.1 Introduction

Velocity gradients are valuable to study the kinematics and dynamics of the ocean currents. They encapsulate information about the flow's deformations and rotations (e.g. Kirwan, 1975), material volumes (e.g. Haller, 2015), and intermittency (e.g. Meneveau, 2011). Furthermore, the large-scale circulation can readily be described by the evolution of velocity gradients such as vorticity and divergence, for instance in the quasi-geostrophic approximation (e.g. Vallis, 2006).

At submeso-scales, $\mathcal{O}(1-10\ km)$, where the Rossby number R_0 and the Richardson number R_i are $\mathcal{O}(1)$, these velocity gradients become leading order terms in the momentum equations (McWilliams, 2016). In the classical description, submesoscale dynamics are fueled by the frontogenetic mesoscale strain field that intensifies lateral buoyancy gradients and accelerates the geostrophic flow (Hoskins and Bretherton, 1972; Stone, 1966). In the last two decades, these currents have been studied in the surface ocean (e.g. Thomas et al., 2008) as well as recently in the abyss (e.g. Wenegrat et al., 2018), as they play an important role in the transition from two-dimensional to three-dimensional turbulence (Molemaker and McWilliams, 2005). In particular, submesoscale flows have been shown to be convergent and generating vertical velocities that are two orders of magnitude larger than at the $\mathcal{O}(100\ km)$ mesoscale (e.g. Mahadevan and Tandon, 2006; Klein and Lapeyre, 2009). These are crucial in linking the boundary layers with the interior ocean and vertically redistributing biogeochemically important tracers such as nutrient, carbon, and oxygen (Omand et al., 2015). It has further been suggested that submesoscale currents impact the horizontal distribution of tracers (Poje et al., 2014; Haza et al., 2016), possibly, because the lateral strain in frontal regions becomes as large as the vorticity. Typically, submesoscale turbulence tends to stretch out tracer patches, forming narrow filaments with sharp gradients that eventually cascade tracer variance to the scales at which it is mixed.

Despite their important role, submesoscale currents and their velocity gradients are difficult to observe synoptically because they evolve on timescales of hours to days over spatial extents of 1-10 km. These scales are challenging to capture from shipboard measurements, contemporary satellite sensors, and autonomous vehicles. In addition to insufficient spatial and temporal resolution, one-dimensional Eulerian measurements often do not allow calculation of the gradient of the velocity field, which tends to be highly anisotropic at fronts. Submesoscale velocity gradients have been observed by experiments

using multiple synchronous velocity measurements (Shcherbina et al., 2013). In coastal regions, high-frequency radar systems (Kirincich, 2016) and aerial imagery are promising technologies to capture submesoscale variability (e.g., Rypina et al., 2014a, 2016).

Targeted, clustered drifter releases are a valuable resource to better understand the velocity gradient evolution at submeso-scales. Lagrangian observations have the advantage of providing a fluid parcel's history while sampling individual submesoscale features. In the past, drifter clusters have been used to estimate velocity gradients. Saucier (1955) estimated atmospheric divergence from three data points of wind measurements based on the rate of change of the area that the triplet encounters. Likewise, after horizontally rotating the horizontal velocities, he estimated vorticity by the rate of change of the area that the triangle would experience with the rotated velocities. Molinari and Kirwan (1975) and Okubo and Ebbesmeyer (1976) furthered the methodology for oceanic drifters and described a linear least-square (LLS) method that computes a bivariate fit to the drifter velocities yielding the velocity gradients as the coefficients of the fit. Kawai (1985) computed vorticity by evaluating the circulation theorem (Thomson, 1867) around a cluster of drifters.

These methods are prone to error due to the geometry of the drifter cluster on which they are computed. Since submesoscale flows are convergent and associated with a large lateral strain, these methods lose accuracy quickly after clusters of drifters start to deform. Although drifter technology has improved dramatically since Molinari and Kirwan (1975), recent studies showed that the velocity gradient estimation is only valid for short times after deployment and for drifter clusters that are small compared to the velocity structure to be analyzed (Berta et al., 2016; Ohlmann et al., 2017; Paduan and Niiler, 1990). The deformation of triplets of drifters in two-dimensional flows has been described extensively in theory (e.g. Pumir et al., 2000) and in experiments (e.g. Merrifield et al., 2010). In oceanic flows, the deformation can be related to the turbulent dispersion of drifters (LaCasce and Ohlmann, 2003) and can thus theoretically be predicted when the kinetic energy spectrum (LaCasce, 2008) is known. In addition to the geometric constraints, it has been shown that Lagrangian observations in convergent flows are inevitably biased as drifters collect in the attracting convergent regions (Choi et al., 2017; D'Asaro et al., 2018). While these regions are often of interest as they are associated with the largest vorticity and vertical velocity, they also cause the strongest deformation and eventually result in the collinearity or alignment of neighboring drifter trajectories.

The primary objective of this manuscript is to measure the velocity gradient from clusters of

drifters at submeso-scales and systematically consider the error associated with the drifter clusters' geometry.

In this manuscript, we revisit the LLS method to estimate velocity gradients from clusters of drifters. Using a submesoscale-resolving model velocity field and artificial drifters, we study the error in the calculation as a function of cluster geometry. We vary the geometry of the artificial drifters and randomly sampling the velocity field in a bootstrap fashion. The idealized sensitivity study helps to constrain the sources of error and interpret the computed velocity gradients when working with observational drifter data. The study of artificial drifters serves as a valuable guide in the design of future Lagrangian experiments to study submesoscale flows.

We then analyze a large, high-resolution drifter dataset collected as part of the Air-Sea Interactions Regional Initiative (ASIRI) in the Bay of Bengal in 2015 (Lucas et al., 2014; Wijesekera et al., 2016). These drifters were deployed across a freshwater-dominated density front with the goal of better understanding the processes that disperse the freshwater (see Chapter 2, Hormann et al., 2016) that is input by major rivers in the north of the bay and intense precipitation during the monsoon (Mahadevan, 2016). Previous studies suggested that these freshwater fronts develop submesoscale dynamics (Ramachandran et al., 2018) that develop large R_0, high lateral strain rates, and possibly divergences of the same order of magnitude. Informed by our modeling study, we apply the LLS method to the drifter data to compute velocity gradients and identify submesoscale signatures. Since most of the drifters recorded both temperature and salinity just below the surface (Hormann et al., 2015, 2016), we have the opportunity to relate the velocity gradient to drifter-derived density gradients, which further corroborate the evidence for submesoscale features.

This study is structured as follows. First, in section 4.2, theoretical considerations of velocity gradients are given. In section 4.3, we introduce the observational and simulated datasets and define the method to compute velocity gradients. In section 4.4, we validate the method in the model and test its sensitivity to the geometry of drifter clusters. In section 4.5, we describe how the observed drifter clusters deform and present the estimated velocity gradient. We discuss in 4.6 and conclude in section 4.7.

4.2 Velocity gradients and their estimation

The four-component velocity gradient tensor $G_{i,j} = \frac{\partial u_i}{\partial x_j}$ of the horizontal velocity u_i can be decomposed into its symmetric ($G^{sym} = \frac{1}{2}(G_{ij} + G_{ji})$) and anti-symmetric ($G^{anti} =$

$\frac{1}{2}(G_{ij} - G_{ji})$) parts. The anti-symmetric part, the spin tensor, describes the rotations of a fluid parcel. Its components are twice the vertical component of the relative vorticity ζ. The trace of the symmetric part is the horizontal divergence, $\delta = G^{anti}_{i=j}$. The off-diagonal components $G^{anti}_{i\neq j}$ of the symmetric part are the shear and normal strain.

Following the naming convention (e.g. Kirwan, 1975), we define the vertical vorticity, horizontal divergence, shear and normal strain rate as follows $\zeta \equiv u_x - v_y$, $\delta \equiv u_x + v_y$, $S \equiv u_y + v_x$ and $N \equiv u_x - v_y$, respectively. As often useful in the oceanographic literature, we combine shear and normal strain rates into a lateral strain rate $\sigma \equiv \sqrt{S^2 + N^2}$ (e.g. Shcherbina et al., 2013). We define the angle between shearing and normal strain as the strain angle $\theta = \arctan(S/N)$ which describes the direction in which σ acts. If $\theta = 0$, the strain elongates in the x-direction and compresses in the y-direction.

The velocity gradient tensor dictates how fluid parcels are separated or brought together by the flow field, as by definition, it describes the velocity differences between two points in space. The eigenvalues of L denote the rate, at which two particles separate subject to the divergence, stretching and shearing of the flow. The sum of the eigenvalues is furthermore equal to the divergence δ. When assuming exponential spreading of neighboring trajectories, the largest, positive eigenvalue is often defined as the Lyapunov exponent λ. It is equivalent to the magnitude of the lateral strain and acts in the principal direction of the strain, $\lambda = |\sigma|$.

The area and shape of a fluid parcel will be unaltered by a pure rotation. Shear, strain, and divergence, however, are linear deformations that can alter the area and shape.

4.2.1 Estimation of the velocity gradients

In this manuscript, we test three multi-drifter approaches to calculate the velocity gradient. Saucier (1953) documented a method to estimate vorticity, strain, and divergence from at least three wind observations in space. These wind observations were hundreds of kilometers apart but separations were still closer than the length scale of atmospheric weather systems. In the 1970s and 1980s, Molinari and Kirwan (1975) and Okubo and Ebbesmeyer (1976) worked on calculating the deformation field from drifter trajectories with respectable success. Molinari and Kirwan (1975) compare Saucier's method with a LLS method and arrive at a good agreement given the limitations of the data. Others, like Kawai (1985), tried to use Kelvin's circulation theorem to estimate vorticity. The accuracy of these estimations suffered greatly from the spatial resolution of the data and the error associated with the position and velocity data. Even with state-of-the-art data,

most methods have shortcomings since they are prone to error resulting from the geometry of observations.

The Saucier (1955) method relies on the fact that, assuming incompressibility, the rate of change of the area of a polygon must be related to the horizontal divergence of the two-dimensional flow as $\delta \approx \frac{1}{T}\frac{A_0 - A}{A_0}$, where T is the time it takes area A_0 to deform into A. Disregarding that the polygon is not a perfect material contour, it is trivial to estimate divergence from clusters of drifters by evaluating the rate of change of the area. Saucier (1955) then applied simple transformations to the two-dimensional velocity vector to bring the vertical vorticity $v_x - u_y$ into a divergence-like form of the transformed horizontal flow, $\hat{u}_x + \hat{v}_y$ and similarly for the lateral strain. This elegant approach works approximately but an additional term would emerge if the coordinate transformation were done carefully on the position instead of the velocity.

Kawai (1985) applied Kelvin's circulation theorem to a polygon of drifters to estimate the area-integrated vorticity by integrating the velocity along a line around the polygon. Since drifter velocity is only known along the trajectories, an interpolation is need to determine the velocity at the center of each polygon side. The segments l of the line integral are then evaluated by $l\delta u$. This method is powerful because of its simplicity. However, as the polygon grows and deforms, the velocity interpolation becomes less accurate and the vorticity estimate erroneous.

A linear least square method to estimate the velocity gradient across a drifter polygon was first described by Molinari and Kirwan (1975) and Okubo and Ebbesmeyer (1976). As a linear estimator, this method's accuracy increases with the number of data points and can, therefore, be improved by taking more than three drifters into account. Furthermore, the estimate is not as sensitive to the cluster geometry as other methods described above.

The Taylor expansion of each drifter's velocity (u_i, v_i) about the center of mass $(\overline{x}, \overline{y})$ of a cluster of drifters gives the following system of equations

$$u_i = \overline{u} + \frac{\partial u}{\partial x}(x_i - \overline{x}) + \frac{\partial u}{\partial y}(y_i - \overline{y}) + \mathcal{O}((x_i - \overline{x})^2) \tag{4.1}$$

$$v_i = \overline{v} + \frac{\partial v}{\partial x}(x_i - \overline{x}) + \frac{\partial v}{\partial y}(y_i - \overline{y}) + \mathcal{O}((y_i - \overline{y})^2), \tag{4.2}$$

where (x_i, y_i) is each drifters position. The expansion is truncated at the first order with the error scaling like $\mathcal{O}(\Delta x^2)$. This remainder represents higher order terms and was attributed to turbulent motions in Molinari and Kirwan (1975). The expression can be rewritten in matrix form, using the vectors $A = (\overline{u}, \frac{\partial u}{\partial x}, \frac{\partial u}{\partial y})$ and $B = (\overline{v}, \frac{\partial v}{\partial x}, \frac{\partial v}{\partial y})$ and the

distance matrix $Q = (1, x_i - \overline{x}, y_i - \overline{y})$, containing the distances in x and y from the position of the center of mass,

$$U = QA + U' \tag{4.3}$$

$$V = QB + V', \tag{4.4}$$

where U' and V' now contain the $\mathcal{O}(\Delta x^2)$ terms representing all small-scale turbulence smaller than the polygon scale. If we assume the $\mathcal{O}(\Delta x^2)$ is small, which is only true for small polygons, U' and V' are small, and we can solve this system exactly by

$$A = (Q^T Q)^{-1} Q^T U \tag{4.5}$$

$$B = (Q^T Q)^{-1} q^T V. \tag{4.6}$$

Vectors A and B contain the spatial derivatives of the horizontal velocity and can be combined to form the vertical component of the vorticity ζ, the divergence δ and the lateral strain α.

4.3 Model-based Sensitivity Analysis

A numerical drifter simulation is used to calculate the velocity gradient tensor with the linear least-squares method on clusters of drifters, and evaluate the accuracy of the estimate against the model flow field, as a function of the cluster geometry.

4.3.1 Numerical model

The method is validated in a model flow field, for which the velocity gradient field is known. Here, we use a non-hydrostatic ocean model (Mahadevan et al., 1996a,b) that is initialized with a density front measured with an underway CTD in the Bay of Bengal in 2013 (Lucas et al., 2014) and forced with realistic wind stress and heat fluxes measured from a mooring at 18N in the Bay of Bengal (Weller et al., 2016). The model is in a channel configuration that is periodic in the east-west direction and has solid boundaries in the north-south direction. With a horizontal resolution (Δx=1 km), the model resolves vigorous submesoscale variability at scales of $\mathcal{O}$(1-20 km) owing to instabilities of the lateral buoyancy gradient. These eddies and filaments often reach vorticity, strain and, divergence of $\mathcal{O}(f)$. The model has been validated extensively with observations to resolve

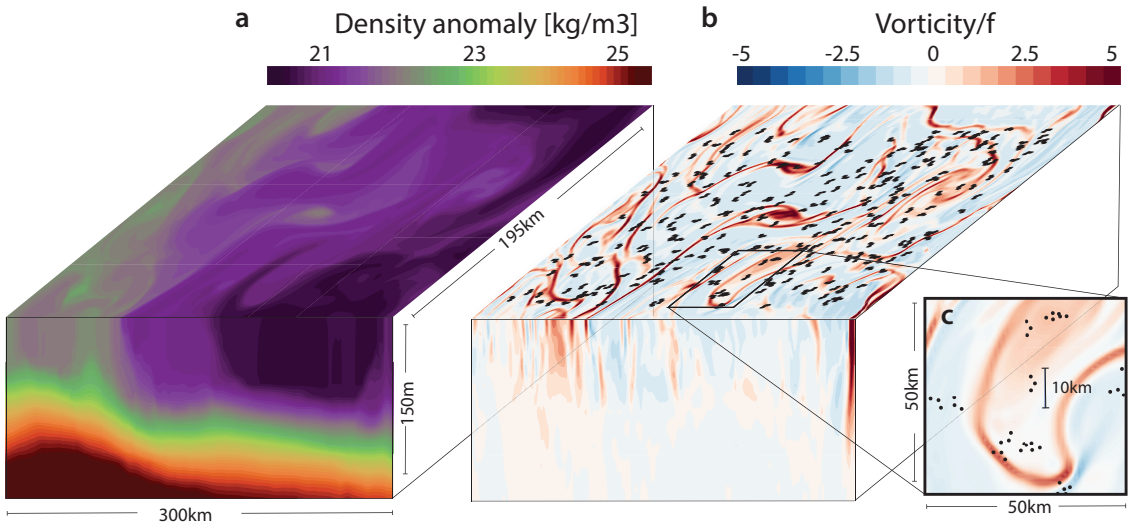

Figure 4-1: Three-dimensional rendering of the fully spun-up numerical simulation. Only the front face and the top face of the domain are shown. a) Density anomaly, $\sigma_0 = \rho - 1000$ kg/m^3, showing a mixed layer at 50 m depth and a lateral buoyancy gradient across the domain. b) Relative vorticity ζ normalized by the Coriolis frequency f. Strong filaments and eddies reach vorticity of up to 5f. Overlaid with dots is an example for 500 drifter clusters at random position. c) Zoom onto a filament with drifter clusters made up of three drifters.

submesoscale flows in various parts of the ocean (e.g. Jaeger and Mahadevan, 2018). We spin up the model until the total kinetic energy levels off to a constant value and use the output from the fully spun-up state.

For the calculation of velocity gradients, we use snapshots of the model fields. Simulated drifters are then seeded in clusters and allow us to estimate the velocity gradients. Note that the drifters are not advected by the flow and merely sample the model's velocity field. A cubic spline interpolation is used to find the velocity at each drifter's position. The initial configurations of drifters are varied to span a wide range of parameters, such as the number of drifter per cluster, and the drifter cluster geometry characterized by their aspect ratio, and length scales.

Since the flow does not affect the drifter positions, we can control the geometry of clusters of drifters. Drifters are thus not biased to sample convergent regions in the flow. Unlike in observational data, we are also avoiding the error associated with the drifter positions which affect the velocity and velocity gradient estimates.

To vary the dominant length scale of variability of the velocity field, we filter the model fields with a two-dimensional Gaussian filter with a radius of $r = 5$km and $r = 10$km. The resulting fields are smooth below the respective filter width $2r$.

4.4 Modeled drifter clusters

Despite an increase in Lagrangian observations in the ocean, there is a lack of analysis tools that utilize multiple drifters to understand the flow field (LaCasce, 2008). In this section, we calculate the velocity gradients from clusters of artificial drifters in a modeled velocity field. By varying the geometry of clusters, we investigate the sensitivity of the velocity gradient estimates.

4.4.1 Velocity gradient in a known flow field

We seed 2500 clusters of artificial drifters in the model, sample the velocity, and compute the velocity gradient using the linear least-squares method (see Section 4.3). Each cluster consists of 3 drifters that form a regular, isosceles triangle with a mean side length of $L = 0.5$ km.

The goodness of the estimates is tested by performing a linear regression between the true values and the estimates. In this section, we focus only on the estimation of vorticity, but the results are just as valid for shear strain, normal strain, and divergence. The coefficient of determination, the Pearson R^2 value, is a way to determine how much of the total variance is captured by the variance of the estimate. In all cases presented here, the R^2 values are significant which is reflected by p-values below 10^{-4}. The variance that is not captured, the residual of the linear regression, is a metric for the standard error.

Figure 4-2 shows the vorticity fields for the three test cases: The original model run, the 5 km filtered, and the 10 km filtered. The estimate for vorticity in all three cases is a good linear fit for the true vorticity field. The R^2 values range from 0.8 to 0.99. As the features in the flow become large relative to the cluster size, i.e., in the filtered cases, the linear fit improves.

In general, the linear least-square method generates good results and reproduce the distribution of vorticity values across the domain. The distribution of the velocity gradient components can only be captured accurately, if drifters are distributed uniformly across the model domain and if horizontal separations between them are small enough to resolve the variability at the model grid scale $\Delta x = 1$ km. The model velocity fields used here are smooth below the grid scale of 1 km. If there is variability at shorter length scales than the cluster scale, the estimates deteriorate as well.

For observational data (see Section 4.5), this poses a challenge since groups of drifters will always only sample a sub-region of the domain, are distributed sparsely, and collect

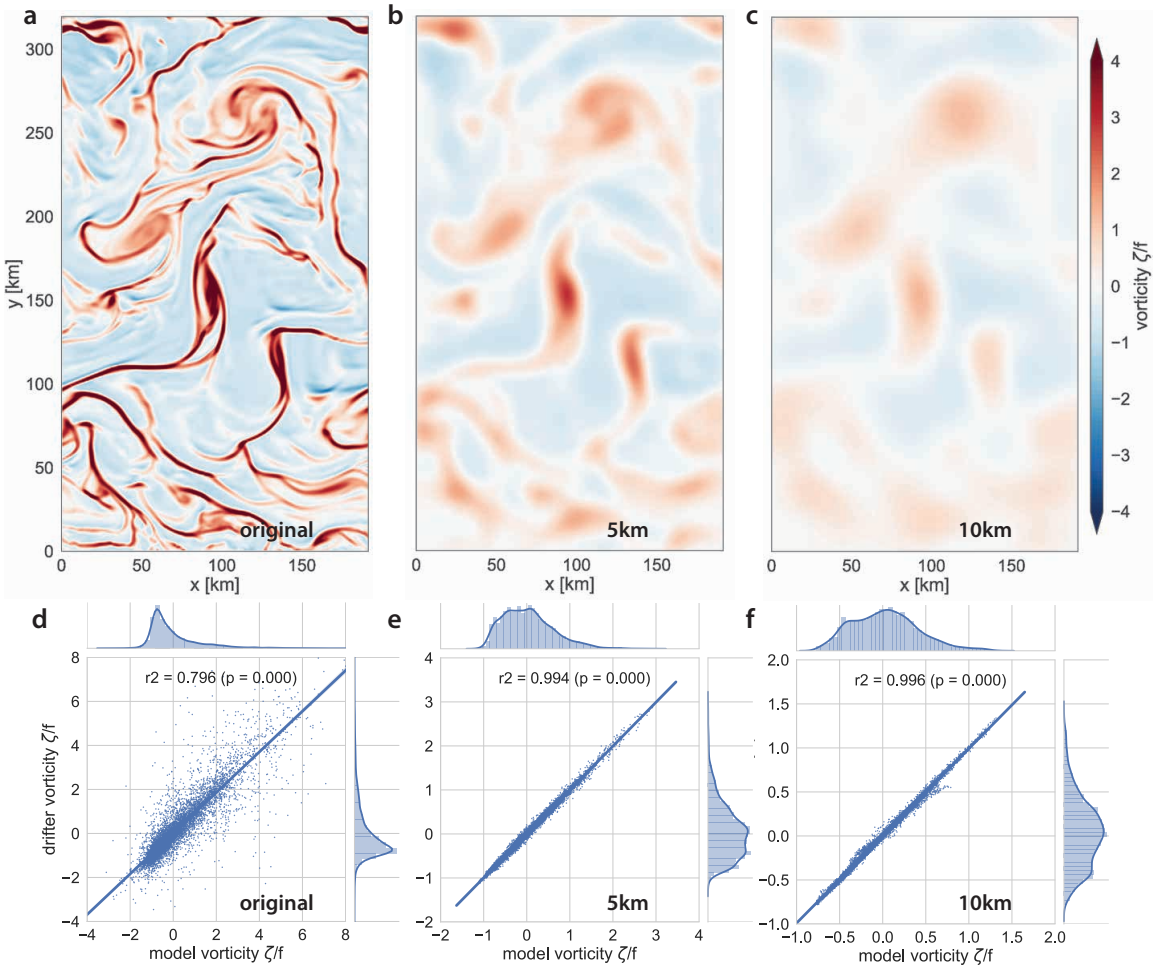

Figure 4-2: Panels a) - c) show vorticity field of the original model simulation, the 5 km Gaussian filtered, and the 10 km Gaussian filtered, respectively. Panels d) - f) present the performance of the vorticity estimation using drifters in the original, 5 km filtered, and 10 km filtered model fields. A linear regression between true model vorticity and the estimated vorticity is used to test the performance of the estimate.

in convergent regions of the flow. It is therefore expected that observational data like presented below will not be able to describe the full distribution of the velocity gradient accurately. Furthermore, observational drifter clusters are not regularly shaped polygons. The impact of their geometry on the goodness of the estimates is addressed in the next part.

4.4.2 Sensitivity of vorticity estimates

The geometry of clusters, their aspect ratio α and their length scale L, are important sources of error when estimating velocity gradients. Using $N > 3$ drifters in the linear least-square method helps to minimize the residual of the linear fit. The length scale L is important since the linear least-square method relies on the assumption of small separations between the cluster vertices (Equation 4.1). The error of the fit goes like $\mathcal{O}((x_i - \overline{x})^2)$. Here, we define the length scale of a cluster of drifters as the root mean square distance between all pairs of drifters $L \equiv \left\langle (\mathbf{x}_i - \mathbf{x}_j)^2 \right\rangle$. Furthermore, the coefficients of the planar fit are approximated at the centroid of the cluster, thus, as clusters become elongated, the velocity gradient at the centroid is no longer representative of the velocity gradient across the cluster. We define the aspect ratio as the ratio between the eigenvalues of the covariance matrix $\alpha = \lambda_{min}/\lambda_{max}$, with $\mathrm{cov}(X, X) = X \cdot X^T$ where X is the matrix of latitude and longitude positions (c.f. Choi et al., 2017). A circular cluster has an aspect ratio of 1, while an ellipsoidal cluster has $\alpha < 1$.

The sensitivity to the geometry can be explored using a bootstrap approach. By varying the geometric properties of the artificial drifter clusters, we thus study how the solution for the velocity gradient behaves as a function of three parameters: the number of drifters per cluster N, the length scale of drifter clusters L, and the aspect ratio α. Here, the velocity field of the model is sampled with 2500 randomly distributed artificial clusters, for which the velocity gradient is calculated and regressed against the true velocity gradient field (see Figure 4-2).

Figure 4-3 shows the results for the sensitivity study. The number of drifters N per cluster increases the accuracy of the estimate (Figure 4-3a). As N increases, the R^2 value increases rapidly and levels off above for the unfiltered model. The impact of N, however, is even more pronounced when the aspect ratio is low and the length scale is large as we will see below. It is worth noting that Okubo and Ebbesmeyer (1976) determined from an error analysis that at least 6 drifters are needed to yield reasonable results. Our bootstrap approach retrieves the same answer.

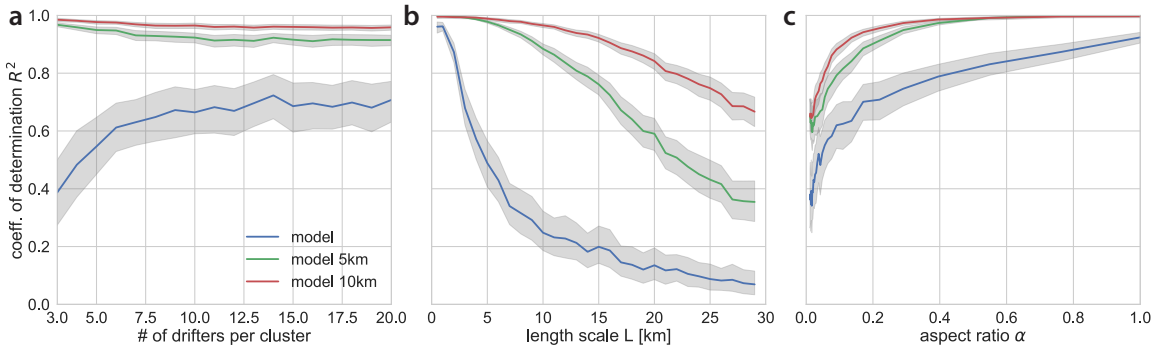

Figure 4-3: Sensitivity of the velocity gradient calculation measured by the coefficient of determination, R^2 between the model vorticity and the estimated vorticity. a) R^2 as a function of number of drifters per cluster (with $L = 1$km, $\alpha = 0.1$) b) R^2 as a function the length scale of drifter clusters (with 3 drifter/cluster, $\alpha = 1$), c) R^2 as a function of the aspect ratio of drifter clusters (with 3 drifter/cluster, $L = 1$km). Each panel shows the results for the original, the 5 km filtered, and the 10 km filtered model fields.

The length L is the best predictor for R^2 when calculating velocity gradients with the LLS method (Figure 4-3b). We normalize the length scale of clusters by the length scale of the flow L_u. We choose L_u by taking the Eulerian spatial correlation function of the horizontal velocity and determining a spatial decay scale from the average over the whole area. These two estimates for a length are not estimated over the same domain; L is a local estimate, while L_u is a global estimate using the entire two-dimensional domain.

Over a few tens of kilometers, R^2 drops from 1 to 0.1. For the original model field, R^2 approximately decreases like $1/L$. As soon as drifter clusters become larger than the dominant scale of variability in the flow (a few kilometers in the model), the estimates become meaningless. This relationship becomes clearer when considering the filtered velocity fields (Figure 4-2 and 4-3), for which there is no variability below the filter length scale of 5 and 10 km. The R^2 values decrease more slowly until the cluster sizes are comparable to the filter scale.

The aspect ratio α of drifter clusters affects the velocity gradient estimates (Figure 4-3c). If clusters are elongated, the estimates no longer represent the velocity gradient at the center of mass of the cluster. Again, the impact is most significant when the velocity field contains small-scale variability. For the filtered velocity fields, R^2 drops steeply below an aspect ratio of 0.2, which is equivalent to a factor 5 between the major and the minor axis of the cluster. In addition to the elongation of a cluster, the direction of elongation relative to the direction of the velocity gradient becomes important. If clusters are elongated perpendicular to the velocity gradient, we are unable to compute the gradient.

4.5 Drifter Analysis

We apply the least square method to a drifter dataset from the Bay of Bengal (Hormann et al., 2016). We compute the velocity gradients of the flow using hexagonal drifter clusters, whose geometry (aspect ratio and length scale) is tracked to estimate the error.

This sensitivity study provides a framework to compute velocity gradients from the drifter data in Section 4.5. To improve the overall estimate of the velocity gradient, we choose to proceed by working with clusters of 6 drifters, which is approximately where the sensitivity curve (Figure 4-3a) reaches its half-maximum R^2. This choice is furthermore a compromise between achieving higher accuracy and being able to form clusters that are still sufficiently small.

4.5.1 Bay of Bengal drifter data

The drifter data used in this study were collected in the Bay of Bengal in 2015 as part of the Air-Sea Interactions Regional Initiative (ASIRI) (Lucas et al., 2014; Wijesekera et al., 2016; Hormann et al., 2016). ASIRI's primary goal is to study processes in the upper ocean to better understand their role for air-sea fluxes and the monsoon system, eventually being able to improve monsoon predictions. This data was collected during the southwest monsoon during which heavy precipitation and freshwater input from major rivers in the north of the Bay of Bengal generate a thin, low-salinity layer that seasonally caps the water column (Figure 4-4).

As part of this campaign, 46 SVP-type surface drifters (one of which failed after deployment) were released in the northern bay at the edge of a strong cyclonic eddy and across a freshwater-dominated density front (Hormann et al., 2016) (Figure 4-4). SVP drifters were drogued at 15 meters depth, reducing the effects of Stokes drift by the surface gravity waves and minimizing wind slippage (Niiler et al., 1995; Maximenko et al., 2013). Since mixed layers were shallow (see Figure 4-4), the deep drogue could affect the extent to which mixed layer current are sampled.

All 46 drifters were equipped with a thermistor that measures temperature a few centimeters below the surface. 36 drifters had an additional conductivity sensor at about 0.5 m depth that allowed us to sparsely map the sea surface salinity structure (Hormann et al., 2015, 2016). The salinity measurements are of great use, since the density at the surface of the Bay of Bengal is controlled by the changes in salinity, rather than temperature, like it is only common in high-latitudes and some semi-enclosed seas.

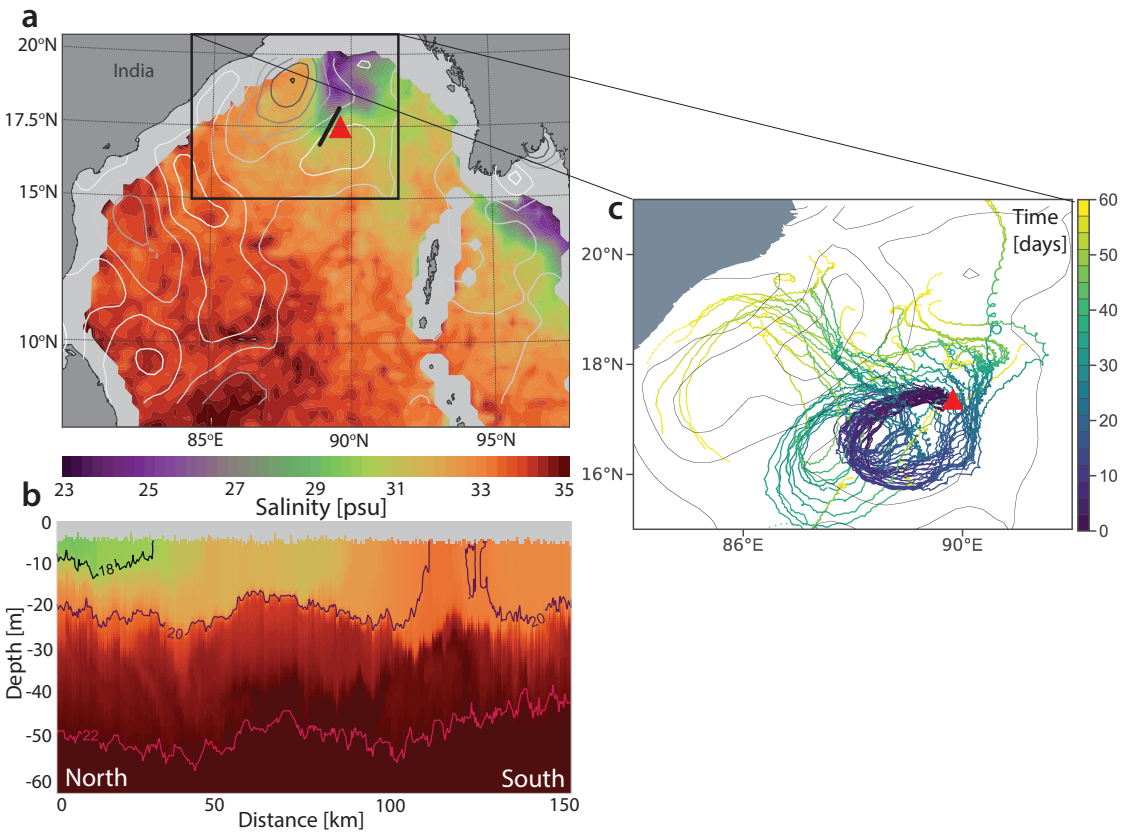

Figure 4-4: a) Map of the Bay of Bengal on September 23, 2015. Sea surface salinity from SMAP is shown in color (purple fresh, red salty). Sea level anomaly from delayed-time, gridded 1/4 degree AVISO is in indicated contours: Light lines are positive and dark colors are negative anomalies. The drifter release location is marked by the red triangle. The black line denotes the coordinates of a CTD section shown below. b) The section of salinity with contours of density anomaly, σ_0 kg/m^3, overlaid. The section is oriented from north to south. c) Drifter trajectories released at the red triangle for the first 2 months after deployment overlaid onto the AVISO sea level anomaly. The time in days after deployment are shown in color.

The drifters were programmed to report their positions at 5-minute intervals during the first month of deployment and at 30-minute intervals after that. This high temporal resolution is needed to resolve small-scale turbulence, like submesoscale dynamics, that evolve with timescales of $\mathcal{O}(1h - 1days)$. To resolve patterns in the flow field at scales ranging from 1 to 100 km, the drifters were released in tight clusters of 4-6 drifters, which were separated by $\mathcal{O}(1\ km)$. Those initial separations are sufficiently small to resolve submesoscale features that have been observed to have length scales of the order of $\mathcal{O}(1 - 10\ km)$ in this region. Ten of those clusters form a larger array spanning an area of about 30 km^2. The initial deployment strategy was therefore aimed at resolving a wide range of different scales in the flow field.

4.5.2 Cluster geometry

On average, drifter cluster sizes grow monotonically over the first month after deployment in the Bay of Bengal (Figure 4-5a). The mean length scale L grows rapidly initially (approximately as $e^{0.2t}$), then stagnates and transitions into a power law growth with $L \approx t^{1.6}$. Here, the most energetic motions are mesoscale eddies that are about 100 km in diameter, larger than the deformation radius $L_D = 60$km. The shaded region in Figure 4-5a shows the 75% confidence interval around the mean.

Compared to expectations from relative dispersion, the initial 3-4 days could reflect exponential growth, which is expected in a nonlocal regime of pair dispersion (see Chapter 2).

The e-folding time scale of L is longer than what was observed from relative dispersion in Chapter 2. This is somewhat surprising because we expect these to equivalent. In contrast to relative dispersion calculations, however, where pairs with short initial pair separation are considered, the mean length scale here is computed from clusters of all initial sizes. At a later time, however, when separations between pairs of drifters become comparable to the dominant eddies, the cluster length scale grows like $t^{1.6}$, which is expected from a Richardson type dispersion (see Chapter 2 LaCasce and Ohlmann, 2003).

Interestingly, as opposed to the mean sizes, the evolution of individual clusters (not shown) reveals that cluster length scales tend to shrink after only a few days, approximately coinciding with the fast decrease in the aspect ratio α. This pattern occurs, in particular, when drifters are traveling along the western edge of the mesoscale eddy during the first 10 days and are strained out along its perimeter.

The shrinking of individual clusters coincides with a minimum in the ensemble mean

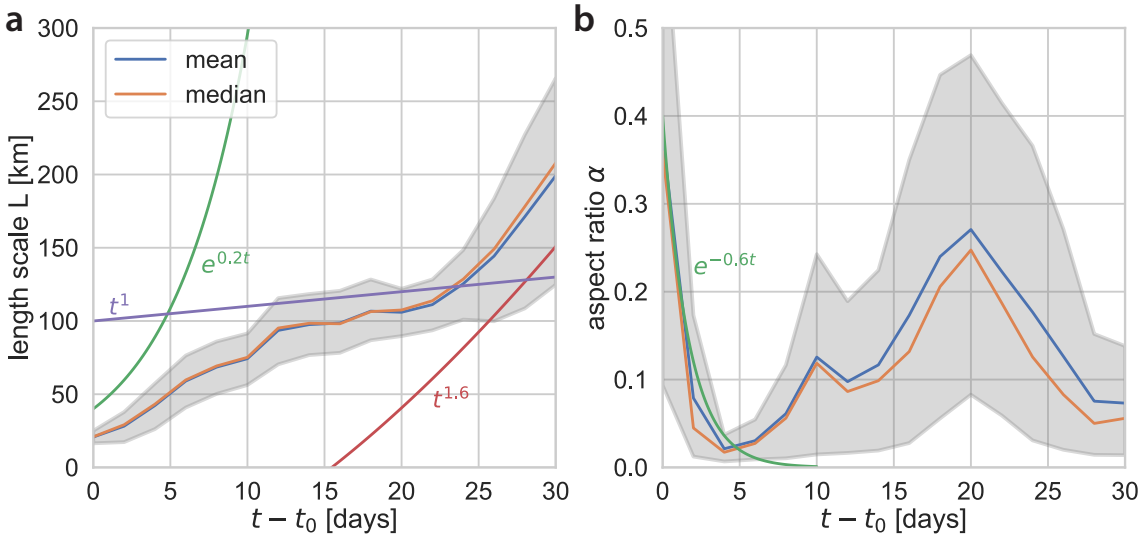

Figure 4-5: a) Evolution of the mean and median hexagon length scale L with time. b) Evolution of the mean and median hexagon aspect ratio α with time. The shaded region in a) and b) is between the 25th and 75th percentile of the distribution. Green, red, and magenta reference lines show visual fits for reference.

aspect ratio, which describes the elongation of clusters of drifters (Figure 4-5b). From their initial configuration at $t = 0$ days when a large fraction has an aspect ratio of 0.5 or greater, clusters are elongated dramatically. Within 2 days, clusters stretch out until at least 75% of the cluster has an aspect ratio of $\alpha < 0.1$. This is equivalent to a major axis 10 times as large as the minor axis. The exponential e-folding time with which this occurs is about 2 days. After $t = 10$, as cluster sizes become comparable to the dominant eddies, the aspect ratio increases again, indicating that clusters become more regular again. However, the variability of the late-time behavior increases significantly as well.

LaCasce and Ohlmann (2003) observed a similar change in cluster aspect ratio. Their aspect ratio, defined as the ratio of base and height of a triangle, becomes order 10 (approximately inverse of α used here) within a couple of days. After 10 days, it settles back toward isosceles triangles with aspect ratio 1, similar to our results here.

As can be seen in the drifter trajectories (Figures 4-4 and 4-6), the drifters are quickly distributed around the perimeter of the mesoscale eddy. During this time, the aspect ratios tend towards zero, and cluster length scales increase rapidly. Only when the drifters leave the influence of the eddy, break up into small groups, the cluster aspect ratios grow and become increasingly regular.

The array of drifters show clear evidence of the wrapping around the eddy (Figure 4-6a). We estimate a two-dimensional histogram in aspect ratio-length scale space (Figure

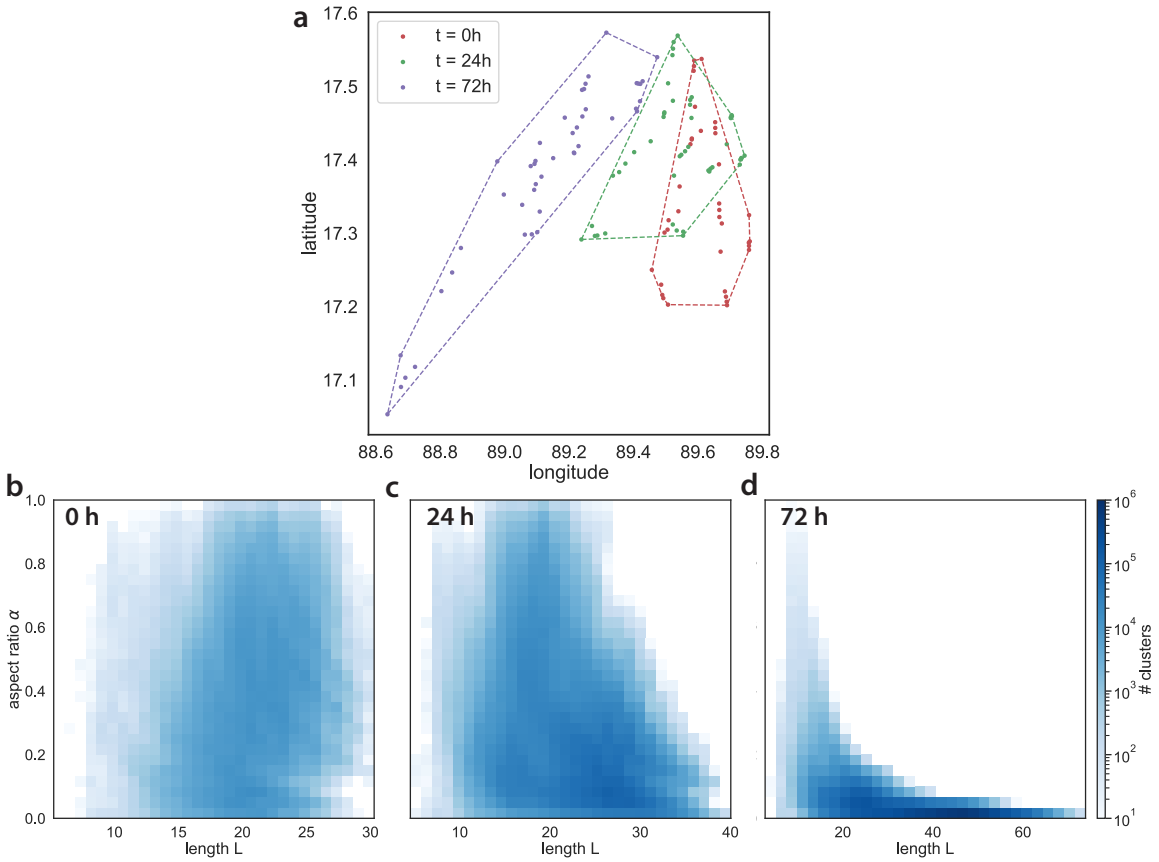

Figure 4-6: a) Drifter locations for 0h (red), 24h (green), and 72h (blue) after deployment. Two-dimensional histograms of cluster aspect ratios α and length scales L of all possible hexagon formed with 45 drifters are shown for a) 0h, b) 24h, and c) 72h after deployment. The color coding is logarithmic.

4-6) to elucidates the distribution around the mean shown in Figure 4-5. The distributions of L suggests that the entirety of hexagons shifts towards larger length scale but also increases its standard deviation around the mean. The confidence interval grows much more quickly from day 1 to 5 than from day 5 to 10 and even more rapid after day 20 (Figure 4-5a).

Judging from the sensitivity study in section 4.4, the ensemble mean length scales and aspect ratios predict low coefficient of determination R^2 between estimated velocity gradients and the true velocity gradient. Furthermore, since the model fields are smooth below 1 km (5 km and 10 km in the filtered cases), we expect the real data to have substantially more noise, which is an additional source of error. It becomes clear that the estimation of velocity gradients can only be successful at short times after deployment (0-3 days), or at a later time, when the aspect ratio increases again (after 20 days). After 20 days, the length scales have already grown to about 100 km on average, which is as large as the dominant mesoscale eddies. We use the knowledge about the deformations in length scale-aspect ratio space to interpret the velocity gradient estimates in Section 4.5.3.

The early time limit for the estimation of velocity gradients can additionally be rationalize by considering the velocity correlation. As described in Chapter 2, we expect pairs of drifters to decorrelate as their separation becomes larger than the dominant eddy size (Figure 2-4). Accordingly, after about 15 days, pairs will start sampling uncorrelated velocities which will render any estimation of velocity gradients futile. Furthermore, velocities can also become decorrelated if drifter clusters become too large for which the analogous argument applies.

4.5.3 Statistics on velocity gradients

Here we focus on the first 2 days of deployment, where length scale L and aspect ratio α are still favorable for the velocity gradient calculation, and drifter velocities are still correlated. We compute the velocity gradients for all possible hexagons ($N = 6$), which for 45 drifters yield 46 choose 6 combinations, adding up to over 8 million hexagons. We average the velocity gradients for each of those hexagons over two hourly snapshots. Based on the results in Section 4.4, we also filter the results by excluding data with $\alpha < 0.1$ (Figure 4-3).

The probability density functions for the vorticity ζ, divergence δ, and strain rate σ are shown in Figure 4-7. The associated length scales and aspect ratios can be found in Figure 4-6. It is evident that the vorticity reaches several times f, particularly at short times after

deployment. When the aspect ratio decreases, e.g., at 3 days, the vorticity increases again to values greater than f. The skewness of the vorticity distribution is positive and large at the beginning, becomes close to Gaussian at day 1, and then increases again as the aspect ratio decreases. The divergence is $\mathcal{O}(f)$ as well (Figure 4-7b,e,h). Similar patterns are evident that we have seen in the estimates for vorticity, however, positively skewed vorticity does not co-occur with negatively skewed divergence. Interestingly, at $t = 0$ h, we find strong divergence which is in contrast with recent observations that reported a dominance of convergent regions on the drifter trajectories. Our results here suggest the opposite behavior and drifters that are pushed apart. The distribution of the lateral strain rate σ has tails that are larger than f throughout the first 3 days, clearly demonstrating that large vorticity and lateral strain coincide (Figure 4-7c,f,i). As the aspect ratios decrease, the strain rate decreases as well. The drifter-derived vorticity, divergence, and strain vary strongly in time over timescales of hours. The tails of the distributions are dominated by small and elongated clusters that tend to generate the largest values. The distribution of vorticity and divergence for large clusters L>20 km shows maximum values of 0.1 f and is symmetric around zero.

In Figure 4-8, vorticity, divergence, and strain are plotted as a function of aspect ratio and length scale. For small aspect ratios, the velocity gradients are a weak function of scale. For large aspect ratios, the velocity gradient approximately falls off like $1/L$. Small aspect ratio and small length scales predict large values in the velocity gradients. At early times (t=0 h), the velocity gradients are associated with variability that is mostly driven by the small scales L<20 km. At later times and larger scales, the velocity gradients become more homogeneous in aspect ratio-length scale space.

We can identify features that occur in vorticity as well as in the lateral strain. Those are particularly strong for L<20 km and aspect ratios of α<0.3. The minimum values of divergence only coincide with large values of vorticity and strain where the aspect ratio is less than 0.2. It can be expected that those values have considerable uncertainty. As the aspect ratio decreases after 72 h, the negative divergence reaches their minimum values. While this might be evidence for convergent regions that drifters collect in, it is likely those extreme values are a consequence of using elongated clusters in the LLS method.

The strain rate is the ultimate driver for the deformation of drifter cluster. By comparing the direction in which clusters are elongated with the strain angle (Section 4.2), the direction in which the lateral strain acts, we can analyze how much control the strain field has on the geometry of drifter clusters. We determine the direction in which a cluster is elongated

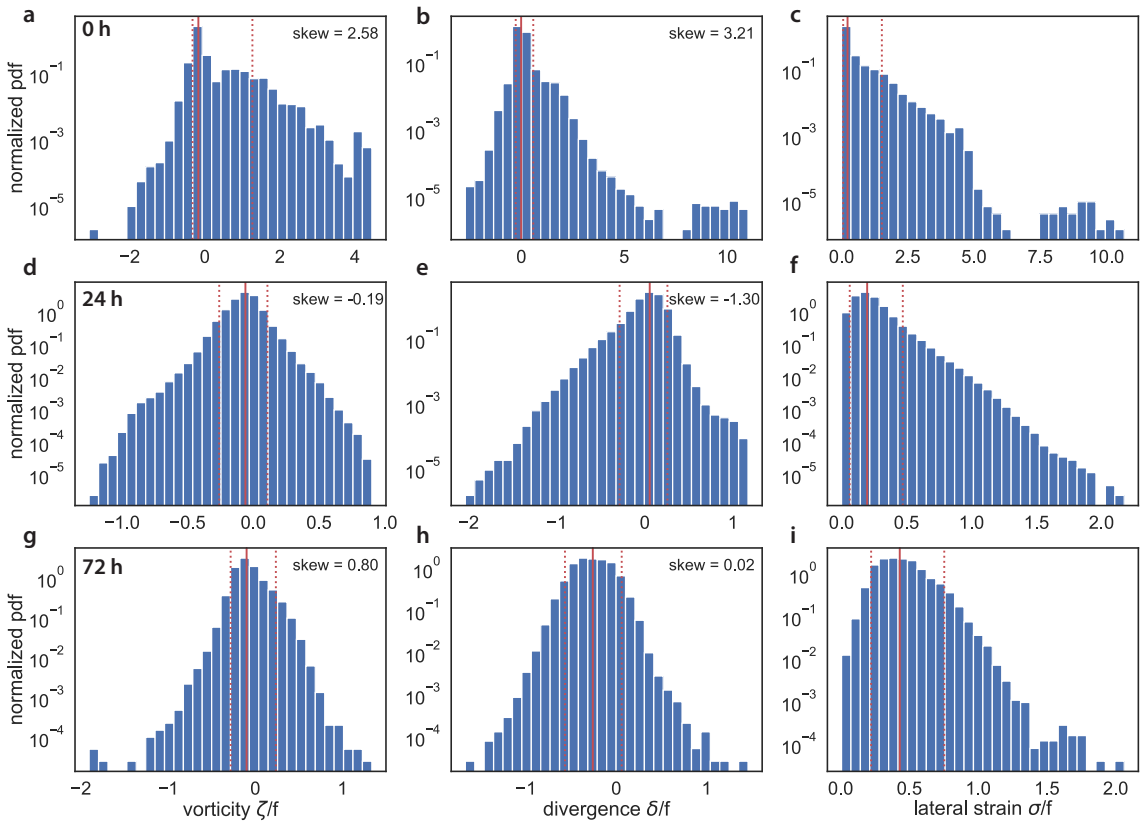

Figure 4-7: Histograms of normalized vertical vorticity ζ/f, divergence δ/f, lateral strain rate σ/f at three instances after deployment: a) 0 h, b) 24 h and c) 72 h. The skewness of the distribution is indicated for the vorticity and divergence. The red lines show the median (solid) and the 5th and 95th percentile of the distribution (dotted). Note that the y-axis is logarithmic.

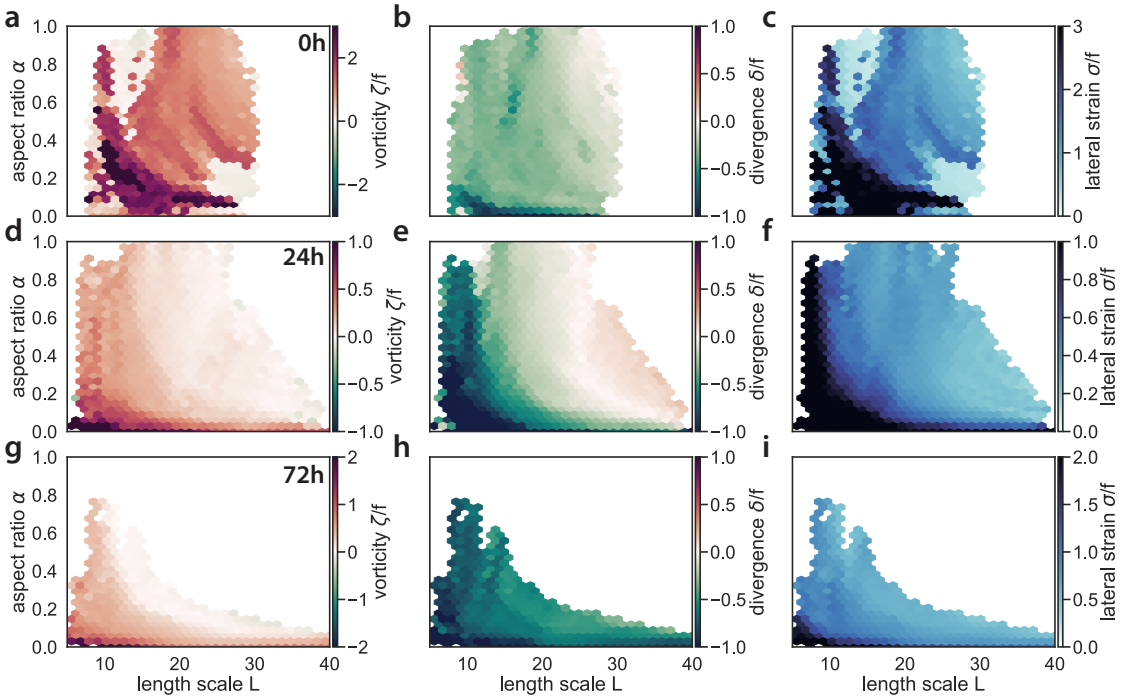

Figure 4-8: Vorticity ζ/f, (a,d,g) divergence δ/f (b,e,h), and strain rate σ/f (c,f,i) as a function of length scale L and aspect ratio α. The top row is 0 h, the middle row 24 h, and the bottom row is 72 h after deployment. Plotted are the 95th percentile of the vorticity and strain rate values (the maximum 5%) and the 5th percentile of the divergence values (the minimum 5%) in each bin. Each bin contains at least 20 data points.

by measuring the angle between its major axis and the x-axis. Its major axis is computed by the largest eigenvalues and associated eigenvector of the covariance matrix (c.f. Section 4.4.2). Figure 4-9 shows the binned and averaged angles for the cluster deformations, and the strain angles. Both datasets have variability, particularly at early times and for small scales, however, consistent patterns are evident in both datasets and all three days. Most of the clusters, initially, are oriented in the north-east direction, which is consistent with the overall orientation of the drifter array (Figure 4-6). These patterns show that the angle of deformation is approximately 90 degrees out of phase with the strain angle.

4.6 Discussion

4.6.1 Estimating velocity gradients in the ocean

The results in Section 4.4 suggest that even slight deformations of drifter clusters have a significant impact on the velocity gradient estimates. Further, we find that as soon as drifter clusters become larger than the scale of variability, estimates of the velocity gradients deteriorate quickly. These results (except for the filtered cases) have been analyzed for a flow field that is characterized by highly energetic, ageostrophic submesoscale flows with Rossby number of $5f$. If submesoscale flows are weak, it can be expected that the error decreases (a bias towards convergent regions is weaker as well).

In the ocean (at least in numerical simulations), the velocity gradients tend to have a blue spectrum at small scales which has been suggested by high-resolution numerical modeling (Barkan et al., 2017). The length scale with which cluster can measure velocity gradient accurately is the front width or the diameter of mixed layer eddies (Fox-Kemper et al., 2008), which is $\mathcal{O}(1)$ km for typical mixed layer values. Operationally, this is hard to achieve for longer periods, unless drifters are release repeatedly in the same region.

The analysis here further suggests that variability below the drifter cluster scale induces a significant error to the calculation. The model we used here is smooth below a scale of 1 km but the ocean currents transition from two-dimensional to three-dimensional turbulence at these scales. Other processes like winds, near-inertial oscillation, surface gravity waves, and Langmuir turbulence can act on small-scales and create a noise in the velocity gradient calculation. Filtering those in time and space is difficult as their timescales often overlap with the timescales of the submesoscale flows.

Submesoscale flows with R_0 of order 1 generate strong convergences that are often associated with large vertical velocities (Mahadevan and Tandon, 2006). These convergent

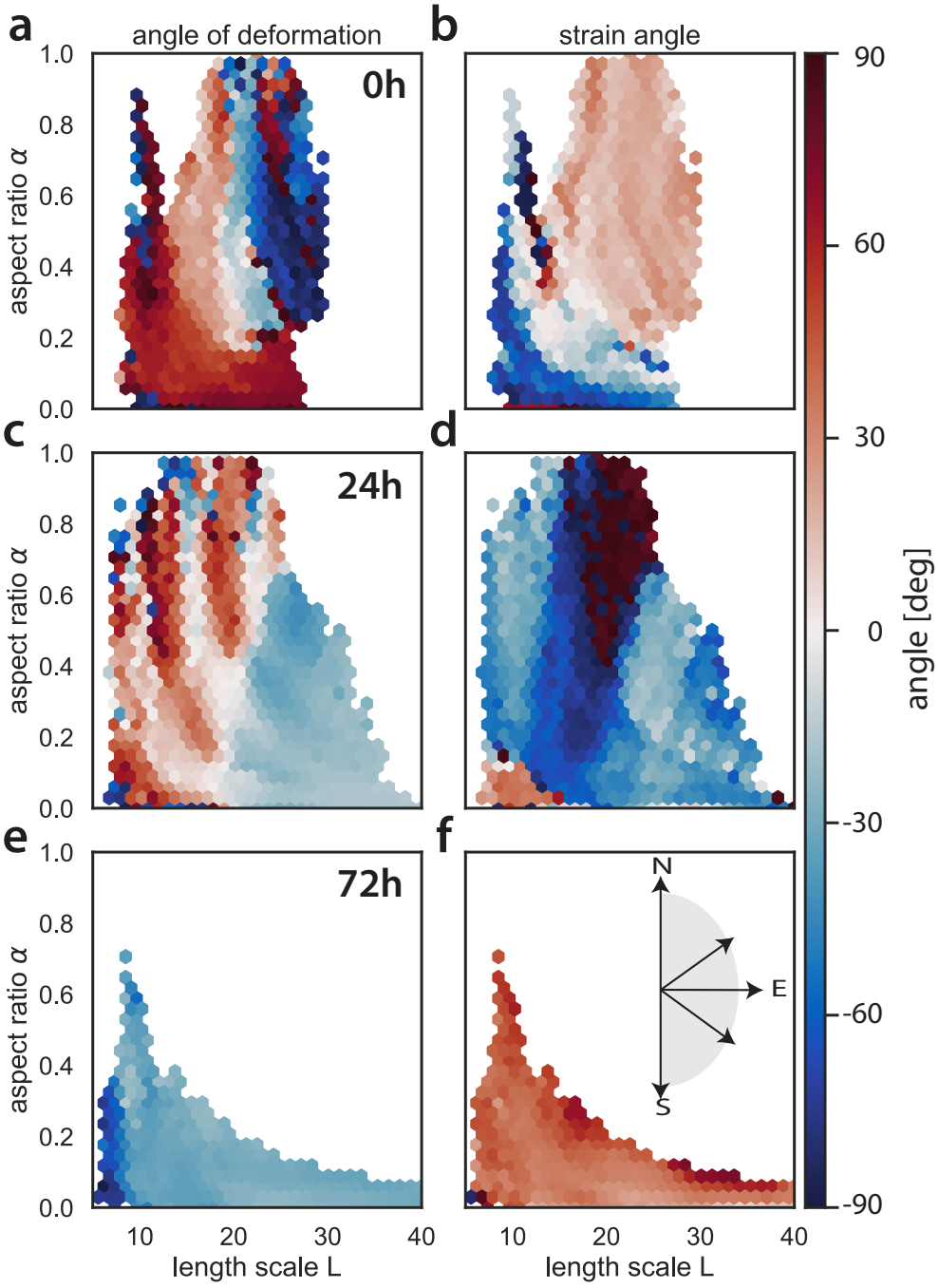

Figure 4-9: The angle relative to the zonal direction for a),c),d) the direction in which clusters of drifters are elongated, and b),d),f) the direction in which the strain rate σ acts. Zero degrees are parallel to the zonal direction, 90 (-90) degrees are directed north (south). Plotted is the circular mean of all values in those bins that contain at least 20 data points.

flows attract drifters and thus bias how they are distributed in space (D'Asaro et al., 2018). In fact, the smaller the length scale, the more three-dimensional the flow is expected to be, which will only increase this effect. Interestingly, our analysis suggest the opposite behavior: strong divergences at the smallest scales that are able to separate pairs of drifters. This is in contrast with observations in the Golf of Mexico and is possibly related to a different set of dynamics, in which submesoscale flows do not develop as strong an eddying field. This result also points out that drifter behavior at the submesoscale might be more complex than the seemingly clear results from the Golf of Mexico suggest.

Although the divergence is a vital quantity to compute in geophysical flows, it is even more difficult to estimate from drifter observations than the vorticity and strain because the divergence is often an order of magnitude smaller. Since the absolute error is the same as in the result shown here, the relative error on the divergence is much larger.

4.6.2 Velocity gradient statistics at submesoscale

Our results show clear indications for submesoscale flows during the first few days of the deployment. Vorticity, divergence, and strain rate reach $\mathcal{O}(f)$, suggesting that the flow departs from geostrophic balance, break its two-dimensional constraints, and develops substantial vertical velocities (that we cannot measure here).

These findings compare well with studies in the Bay of Bengal that used shipboard measurements and numerical simulation to identify submesoscale dynamics. Jaeger and Mahadevan (2018) find that submesoscale re-stratification can explain the compensation of density front at scales of $\mathcal{O}(1)$ km. Ramachandran et al. (2018) analyze the potential vorticity in shipboard observations and numerical simulations to infer that submesoscale processes influence the vertical structure of shallow salinity front in the Bay of Bengal at scales of $\mathcal{O}(1)$ km.

Although not as pronounced as in other recent work (e.g. D'Asaro et al., 2018), we find positive skewness in the vorticity distribution at early times which can be attributed to the asymmetry in the potential vorticity equation. Since f is positive, it reinforces positive vertical vorticity and counteracts negative vertical vorticity. Furthermore, negative potential vorticity is subject to rapid symmetric instability which further shifts the balance towards positive vorticity, and increasing the lifetime of features of positive vorticity.

Compared to other studies that attempt to use drifters to calculate the velocity gradients (Berta et al., 2016; Ohlmann et al., 2017), our results only yield moderately large values and do not reach vorticity and strain rate of $>3f$. This difference might partly be because

the SVP drifters used here are drogued at 15 m depth which is substantially deeper than the drifters used in Berta et al. (2016) and Ohlmann et al. (2017). We also strictly filter clusters with aspect ratios of $\alpha < 0.1$ and use 6 drifters per cluster, which affects the smallest clusters. The same is true for divergences which were reported recently to reach $6f$ (D'Asaro et al., 2018) and were negatively skewed in high-resolution numerical simulations (Choi et al., 2017).

4.6.3 Relationship of deformation and velocity gradients

Intuitively, the measured velocity gradients are directly related to the deformations of drifter clusters and alter their size and aspect ratio. While purely rotational flows do not change these properties, the divergence and strain field deform clusters. The area that those cluster described is conserved by shearing and stretching but not in convergent and divergent regions.

Here, the largest values for strain and divergence occur at the perimeter of the mesoscale cyclone (Figure 4-4) that the drifters were entrained in during the first 10 days. It is likely that the density gradients generated by freshwater were also oriented by the mesoscale strain field. It is striking how fast the majority of clusters collapsed to an aspect ratio of $\alpha < 0.1$ while traveling around the eddy. The squeezing of a regular hexagon with $L = 20$ km from $\alpha = 1$ to $\alpha = 0.1$, requires a ten-fold elongation in one direction, assuming the perpendicular direction remains unchanged. To achieve this in 2 days, a strain rate of about $\cdot 10^{-5}$ 1/s is needed which is of $\mathcal{O}(f)$.

Conceptually, submesoscale flows are expected to be energized by the large-scale strain field that intensifies lateral buoyancy gradients (Hoskins and Bretherton, 1972; McWilliams, 2016), such that the flow accelerates and departs from geostrophic balance. We expect submesoscale flows, therefore, to occur in those regions of large strain.

4.7 Conclusions

The estimation of velocity gradients from drifters in the Bay of Bengal revealed evidence for submesoscale flows. Those have positively-skewed vorticity with maximum values of 3f, negatively-skewed divergence with minimum values of -3f, and co-located lateral strain with maximum values of 3f. While clusters with small aspect-ratio ($\alpha < 0.1$) are inflicted with the largest error, those are also the ones with the smallest length scales that generate the tails of the velocity gradient distributions. To further unravel which velocity

gradients are real, even when the aspect ratio is small, it is necessary to take the orientation of skewed clusters relative to the direction of the velocity gradient (principal strain axes) into account.

Our analyses show that the LLS method proposed by Okubo and Ebbesmeyer (1976) and Molinari and Kirwan (1975) is the most accurate (of the three methods evaluated) for calculating velocity gradients from drifters. However, the uncertainty in the estimate becomes large once the drifter-formed clusters start to grow and deform. The error associated with the geometry is expected to be largest in frontal regions and at the submeso-scale where large velocity gradients, create convergence and lateral strain and deteriorate the estimate of velocity gradients themselves. An additional bias of drifter sampling towards convergent regions only increases this error. It is a challenge for future experiments to overcome this error, potentially by repeat-sampling individual features in the flow or increasing the number of drifters and re-seeding the flow.

This study complements the insights gained from pair dispersion statistics in the submesoscale subrange (Chapter 2) and reveals additional constraints that could not be established from studying pairs of drifters alone. In fact, the velocity gradient estimates give information about the dynamics at these scales that are elusive in pair dispersion statistics.

Since uncorrelated noise in the velocity (of order 1 cm) impacts the velocity gradient estimate by contributing an error of up to 10%, it can be expected that higher accuracy in the GPS fix of drifters will improve our ability to do this calculation. It also suggests that velocity gradients from near-surface drogues will be significantly noisier than the 15 m drogued drifters used here because of the effects of winds and surface waves.

Chapter 5

CONCLUSIONS

Submesoscale flows are known for producing intricate spatial structure in tracers distributions owing to their complex deformation field, namely their divergence, lateral strain, and vorticity of $\mathcal{O}(f)$. Furthermore, as submesoscale flows are energized at the boundary by frontogenesis of lateral buoyancy gradients, submesoscale flows are strongly surface-intensified and decay rapidly with depth, generating vertical shears of $\mathcal{O}(100f)$. Both intensified horizontal and vertical velocity gradients at submesoscales have the potential of separating pairs of particles and, thus, impact lateral diffusivity and transport.

This thesis focuses on three aspects of the behavior of Lagrangian particles in submesoscale flows that are addressed using drifter observations and simulated trajectories in a numerical model.

- Investigating the turbulent dispersion of pairs of drifters in the submesoscale range in the presence of energetic mesoscale eddies (Chapter 2).
- Identifying the influence of the vertical structure of the velocity field on the horizontal pair dispersion, presuming that Lagrangian particles have a vertical separation (Chapter 3).
- Developing and assessing analytical methods to exploit information from cluster experiments of drifters to estimate the local velocity gradient (Chapter 4).

In this chapter, I will review the major findings of each chapter in the context of the current literature. I will then conclude by giving an outline of the outstanding questions and the future direction that this dissertation provoked.

5.1 Summary

In Chapter 2, we investigate the pair dispersion of drifters in the submesoscale range. A careful analysis of SVP-drifter data reveals that the classic pair dispersion statistics, e.g., relative dispersion and Finite-Scale Lyapunov Exponents, agree with a nonlocal dispersion regime (Lundgren, 1981) even in the submesoscale range of motions, suggesting that relatively steep energy spectra in the mesoscale range dominate pair dispersion down to the kilometer-scale. This finding was in contrast with other hydrographic surveys in the region that showed active, energetic submesoscale currents and provoked the hypothesis that drifter dispersion might be controlled by local, submesoscale eddies (Richardson, 1926). Submesoscale eddies are supported by an analysis of the second order structure functions, with which we can identify a range of scales below 10 km that weakly deviates

from geostrophic balance and indicates, at least theoretical, that local dispersion should be expected.

Although nonlocal dispersion is identified as the controlling regime, we fail to reproduce trajectories by using altimetry-derived, geostrophic currents, which are lacking small-scale variability. The geostrophic currents at best reproduce the qualitative, large-scale picture. Using a tuned first-order stochastic model in superposition with those currents, however, enables us to approximately reproduce some of the pair dispersion statistics that the observations produce. Particularly, the relative diffusivity of particles with stochastic noise becomes more realistic results.

In contrast to other recent drifter observations in the submesoscale range (e.g., Poje et al., 2014; D'Asaro et al., 2018), our dataset was not able to unambiguously capture the submesoscale characteristics. Consequently, we cannot support the claim that an energy cascade could be observed at scales below 100 km. Furthermore, our dataset was biased by near-inertial oscillation. However, low-pass filtering did not steepen our structure functions significantly (e.g., Beron-Vera and LaCasce, 2016). Interestingly, the small-scale energy capture by structure functions must then be a process that is energetic but does not substantially affect pair dispersion.

We identify the depth at which the SVP drifters are drogued (15 m) as one of the major limitations of the dataset, particularly, because the mixed layer depth was $\mathcal{O}(15\ m)$ as well. Assuming that submesoscale motions are strongest within the mixed layer and decay quickly below, it is unclear if the SVP drifters were able to sample them accurately. It is conceivable that the drifters escaped and re-entered the mixed layer in an unpredictable way and there sampled the local energy spectrum intermittently. It is impossible to reproduce the location within the mixed layer post-experiment, even when using temperature and salinity sensors located in the buoy.

In Chapter 3, motivated by the shortcomings of Chapter 2, we model simulated trajectories to understand the role that various droguing depths and vertical shear plays in the horizontal dispersion. Vertical shear has long been identified as an important driving mechanism for dispersion (Sundermeyer and Ledwell, 2001), also in the context of shear dispersion that subsequently enhances horizontal mixing (e.g., Taylor, 1953), however, it did not enter the discussions about drifter dispersion because of their surface-trapped design. An important consequence is that, if drifters are used to infer horizontal diffusivity, they might not represent the diffusivity of three-dimensional fluid parcels, mainly because of the effect of vertical shear.

In a numerical simulation of submesoscale turbulence, we show that the vertical velocity gradients are indeed orders of magnitude larger than the horizontal velocity gradients, indicating a much larger potential to separate pairs of particles. We not only find that the relative dispersion of pairs of particles is larger due to the vertical shear, but, that the time dependence of the process is ballistic. In the presence of the ballistic regime, the turbulent dispersion regimes, for instance the Richardson and Lundgren regimes found in Chapter 2, are no longer observable because they are overpowered by the effect of vertical shear. This is an effect primarily observed at the early times of the experiments, which also coincides with time scales associated with submesoscale flow.

Furthermore, we find that most of the vertical shear is concentrated in regions of filaments and eddies. As opposed to the energetic wave field that contains much of the vertical shear in the ocean, filaments persist longer and pose an important mechanism for particles separating along the major axis of density fronts. While it is known that velocity gradients are intensified at fronts and in filaments, this work demonstrates that vertical gradients in velocity have even larger magnitude.

In Chapter 4, we compute the velocity gradient from clusters of drifters as a function of separation scale. These velocity gradients become $\mathcal{O}(f)$ at submesoscales and are largest at fronts and in filaments. Previously described methods that use least-square bilinear fits to the drifter velocities (Molinari and Kirwan, 1975; Okubo and Ebbesmeyer, 1976) or the rate of change of the area enclosed by a group of drifters (Saucier, 1955, 1953) are simple tools to achieve estimates, however, our analyses suggest that they are highly sensitive to the geometry of drifter clusters. The problem therefore becomes more difficult with time as the desired properties, the divergence, vorticity, and strain, lead to more distorted, elongated clusters that then lose their predictive power of the velocity gradient itself.

Using particles released in a numerical model, we explore the parameter space of cluster area and cluster aspect ratio to quantify the error in the estimation. It is evident that due to the deformations and the fast growth of clusters, the window for estimating statistics on the velocity gradient in the submesoscale range is short. Further complicating is the fact that small amounts of noise on the location or velocity data can have a dramatic effect on the velocity gradient prediction. This is particularly troublesome considering the range of processes that shares the same spatio-temporal band as submesoscale currents.

Even though the estimates of velocity gradients are affected by large errors, they are in many situations the only estimates available in the submesoscale range since other technologies are also severely limited by spatial and temporal resolution.

5.2 Implications

The scale-dependent energy spectrum, which fully predicts the turbulent dispersion regimes, is an elusive quantity in the ocean, particularly at scales below the deformation radius L_D (e.g., Balwada et al., 2016). Current measurement technology does not allow a higher spatial resolution than a few kilometers and is oftentimes only available in along-track direction. One of the major questions this thesis attempts to answer is how to characterize the flow at submesoscale length scales using Lagrangian observation. Lagrangian observation are promising to reach higher spatial resolution because satellite technology is now able to report GPS fixes in 5-minute intervals or less, which grants high along-trajectory resolution. Furthermore, drifter experiments are often laid out in clusters, such that neighboring pairs provide initial separations of a few hundred meters or less.

Theoretical expectation for the shape of the energy spectrum at submesoscale predict flat spectral slopes, ranging from -2 for step function-like velocity fields in frontogenetic flows (Hoskins and Bretherton, 1972) or $-5/3$ for surface quasi-geostrophy (Blumen, 1978). Validating the accurate model in observations is complex, not only because of limitations in resolution, but also because of the high intermittency and locality of submesoscale turbulence.

The results of this thesis reflect the difficulty of capturing submesoscale flows, particularly in Lagrangian observations. Since submesoscale flows are often energized by mesoscale strain, their impact on trajectories is difficult to separate from the mesoscale. Furthermore, the question if submesoscale energy spectra cause local dispersion at the smallest scales remains unanswered and the observations and numerical simulations here are not sufficient to test this hypothesis. Chapter 2, however, suggests that the nonlocal subrange in the energy spectrum dominates at the smallest scales, despite of the presence of flatter energy spectra at those scales.

Furthermore, the small-scale band occupies similar time and space scale as wave motions, such as inertia-gravity waves. While those are expected to have a small impact on Lagrangian dispersion, they will influence the energy spectrum at these scales. What is needed to accurately predict the dispersive properties of the submesoscale band, is a band-stop filtered energy spectrum in which processes that are inefficient at dispersion are removed. Our results in Chapter 2 and Chapter 4 suggest that convergent motions at the smallest scales can drastically affect estimates of structure functions and velocity gradients and therefore need to be taken into account.

On the contrary, when modeling trajectories at the submesoscales, the small-scale parameterizations tend to have a much larger effect on the dispersion statistics than their spatial wavelength would suggest. In Chapter 2, we find that random velocity perturbations of $\mathcal{O}(1\ cm/s)$ impact the pair dispersion statistics; the signal of these perturbations even propagate up-scale up to $\mathcal{O}$(20 km). Likewise, similar perturbations render the velocity gradient estimates in Chapter 4 useless because velocities become decorrelated much faster. Capturing the correct spatial and temporal decorrelation scales at these scales, is a major challenge that needs to be resolved, in order to represent submesoscale dispersion in regional models.

The results of horizontal dispersion due to vertical shear in Chapter 3 are not surprising from the standpoint of dye and lab experiments, since it has been known for decades that the velocity decays faster vertically than horizontally and, thus, velocity gradients are stronger vertically as well. However, in the context of drifter observations, the question of dispersion due to the vertical shear has not been discussed by the community because most Lagrangian platforms are two-dimensional.

Since vertical shear is so much larger than horizontal strain, particularly at submesoscales, it is the dominant mechanism that disperses properties horizontally. Furthermore, most properties of interest, such as plankton, organic carbon, and nutrients, do not behave like drifters but will be advected vertically. The effective horizontal diffusivity is therefore different than the diffusivity diagnosed by drifters - an important piece of information when informing models and trying to predict trajectories.

The implications of the dispersion by vertical shear on biological communities could be manifold. It is conceivable that filaments and front provide complex horizontal transport pathways that motile organisms might be able to use by vertical movement in order to control their horizontal movement. Fronts and filaments can also be considered as transport barriers, such that community composition will vary in the cross-front direction. This begs the question if a two-dimensional picture of the hydrography is sufficient, or if there are transport barriers in the vertical that can divide communities in the vertical in regions of strong vertical shear.

Studying the three-dimensional motion in the mixed layer is limited by our ability to model the vertical velocity. While high-resolution numerical simulation can reproduce submesoscale patterns in vertical velocity accurately, various other source for vertical velocity remain elusive, such as convective overturning, Langmuir circulation, and vertical velocity associated with internal waves.

5.3 Outlook

Submesoscale flows challenge the conventional theories for particle dispersion because they are strongly divergent. If trajectories, indeed, collapse into a line as it was described by D'Asaro et al. (e.g., 2018), degrees of freedom are lost when computing statistics about the flow. Our velocity gradient calculations seem to show strongly divergent flows at small scales, which would have the opposite effect. Furthermore, the concept of relative dispersion is based on monotonously growing pair separations in an ensemble-mean sense. Pair dispersion statistics are challenging to interpret if most of the trajectories become collinear. Similar arguments can be made for structure functions and velocity gradients estimated from clusters of drifters that aggregate in convergent regions of the flow. More work needs to be done to understand the bias in data collection due to convergent flows and to reconcile existing data analysis techniques with submesoscale flows.

The evolution of patches of fluid cannot be described by two-particle statistics alone, and, especially in the anisotropic submesoscale turbulence, two-particle statistics are not sufficient to understand how fluid parcels deform. Multi-particle methods need to be refined to extract higher order information about the flow and its two-dimensional geometry. Contemporary experiments develop in the direction of releasing many drifters, often in complex spatial configuration to allow triangulation. Unless the same feature is sampled with multiple realizations, it is difficult to derive statistics on the velocity gradients. Repeated experiments in the same regions of the flow give promising results and allow for cross-comparison of multiple drifter clusters.

BIBLIOGRAPHY

Artale, V., Boffetta, G., Celani, A., Cencini, M., and Vulpiani, A. Dispersion of passive tracers in closed basins: Beyond the diffusion coefficient. *Physics of Fluids*, 9(11):3162–3171, 1997.

Aurell, E., Boffetta, G., Crisanti, A., Paladin, G., and Vulpiani, A. Predictability in the large: an extension of the concept of Lyapunov exponent. *Journal of Physics A: Mathematical and General*, 30(1):1–26, Jan. 1999.

Babiano, A., Basdevant, C., Le Roy, P., and Sadourny, R. Relative dispersion in two-dimensional turbulence. *Journal of Fluid Mechanics*, 214:535–557, 1990.

Badin, G., Tandon, A., and Mahadevan, A. Lateral mixing in the pycnocline by baroclinic mixed layer eddies. *Journal of Physical Oceanography*, 41(11):2080–2101, Nov. 2011.

Balwada, D., LaCasce, J. H., and Speer, K. G. Scale-dependent distribution of kinetic energy from surface drifters in the Gulf of Mexico. *Geophysical Research Letters*, 43(20): 10,856–10,863, Oct. 2016.

Barkan, R., McWilliams, J. C., Shchepetkin, A. F., Molemaker, M. J., Renault, L., Bracco, A., and Choi, J. Submesoscale dynamics in the northern Gulf of Mexico. part i: Regional and seasonal characterization and the role of river outflow. *Journal of Physical Oceanography*, 47(9):2325–2346, 2017.

Batchelor, G. K. *The theory of homogeneous turbulence*. Cambridge university press, 1953.

Bennett, A. *Lagrangian statistics*. Cambridge University Press, Cambridge, 2006.

Bennett, A. F. Relative dispersion: Local and nonlocal dynamics. *Journal of the Atmospheric Sciences*, 41(11):1881–1886, 1984.

Bennett, A. F. A Lagrangian analysis of turbulent diffusion. *Reviews of Geophysics*, 1987.

Beron-Vera, F. J. and LaCasce, J. H. Statistics of simulated and observed pair separations in the Gulf of Mexico. *Journal of Physical Oceanography*, 46(7):2183–2199, July 2016.

Berta, M., Griffa, A., Özgökmen, T. M., and Poje, A. C. Submesoscale evolution of surface drifter triads in the Gulf of Mexico. *Geophysical Research Letters*, 43(22):11,751–11,759, 2016.

Blumen, W. Uniform potential vorticity flow: Part i. theory of wave interactions and two-dimensional turbulence. *Journal of Atmospheric Sciences*, 35(5):774–783, May 1978.

Boccaletti, G., Ferrari, R., and Fox-Kemper, B. Mixed layer instabilities and restratification. *Journal of Physical Oceanography*, 37(9):2228–2250, Sept. 2007.

Bowden, K. F. Horizontal mixing in the sea due to a shearing current. *Journal of Fluid Mechanics*, 21(1):83–95, Jan. 1965.

Bühler, O., Callies, J., and Ferrari, R. Wave–vortex decomposition of one-dimensional ship-track data. *Journal of Fluid Mechanics*, 756:1007–1026, Oct. 2014.

Callies, J. and Ferrari, R. Interpreting energy and tracer spectra of upper-ocean turbulence in the submesoscale range (1–200 km). *Journal of Physical Oceanography*, 43(11):2456–2474, Nov. 2013.

Callies, J., Ferrari, R., Klymak, J. M., and Gula, J. Seasonality in submesoscale turbulence. *Nature Communications*, 6:6862, Apr. 2015.

Centurioni, L., Horányi, A., Cardinali, C., Charpentier, E., and Lumpkin, R. A global ocean observing system for measuring sea level atmospheric pressure: Effects and impacts on numerical weather prediction. *Bulletin of the American Meteorological Society*, 98:231–238, Feb. 2017.

Centurioni, L. R. Drifter technology and impacts for sea surface temperature, sea-level pressure, and ocean circulation studies. In *Observing the Oceans in Real Time*, pages 37–57. Springer, Cham, Cham, 2018.

Charney, J. G. Geostrophic turbulence. *Journal of the Atmospheric Sciences*, 28(6):1087–1095, 1971.

Chelton, D. B., deSzoeke, R. A., Schlax, M. G., El Naggar, K., and Siwertz, N. Geographical variability of the first baroclinic Rossby radius of deformation. *Journal of Physical Oceanography*, 28(3):433–460, Mar. 1998.

Choi, J., Bracco, A., Barkan, R., McWilliams, J. C., Molemaker, J. M., and Shchepetkin, A. F. Submesoscale dynamics in the northern Gulf of Mexico. part iii: Lagrangian implications. *Journal of Physical Oceanography*, 47(9):2361–2376, Sept. 2017.

D'Asaro, E. A., Shcherbina, A. Y., Klymak, J. M., Molemaker, J., Novelli, G., Guigand, C. M., Haza, A. C., Haus, B. K., Ryan, E. H., Jacobs, G. A., Huntley, H. S., Laxague, N. J. M., Chen, S., Judt, F., McWilliams, J. C., Barkan, R., Kirwan, A. D., Poje, A. C., and Özgökmen, T. M. Ocean convergence and the dispersion of flotsam. *Proceedings of the National Academy of Sciences*, 115(6):1162–1167, Feb. 2018.

Davis, R. E. Lagrangian ocean studies. *Annual Review of Fluid Mechanics*, 23(1):43–64, 1991.

Döös, K., Kjellsson, J., and Jönsson, B. TRACMASS—a lagrangian trajectory model. In *Preventive Methods for Coastal Protection*, pages 225–249. Springer International Publishing, Heidelberg, 2013.

Ducet, N., Le Traon, P. Y., and Reverdin, G. Global high-resolution mapping of ocean circulation from TOPEX/Poseidon and ERS-1 and -2. *Journal of Geophysical Research: Oceans*, 105(C8):19477–19498, 2000.

Er-El, J. and Peskin, R. L. Relative diffusion of constant-level balloons in the Southern Hemisphere. *Journal of the Atmospheric Sciences*, 38(10):2264–2274, 1981.

Foussard, A., Berti, S., Perrot, X., and Lapeyre, G. Relative dispersion in generalized two-dimensional turbulence. *Journal of Fluid Mechanics*, 821:358–383, May 2017.

Fox-Kemper, B., Ferrari, R., and Hallberg, R. Parameterization of mixed layer eddies. Part I: Theory and diagnosis. *Journal of Physical Oceanography*, 38(6):1145–1165, Dec. 2008.

Garrett, C. and Munk, W. Space-time scales of internal waves. *Geophysical Fluid Dynamics*, 3(1):225–264, Jan. 1972.

Gon, Y. J., Yong, K. S., and Seong, K. H. Spectral descriptions of submesoscale surface circulation in a coastal region. *Journal of Geophysical Research: Oceans*, 123(0), 2018.

Graff, L. S., Guttu, S., and LaCasce, J. H. Relative dispersion in the atmosphere from reanalysis winds. *Journal of the Atmospheric Sciences*, 72(7):2769–2785, July 2015.

Griffa, A., Owens, K., Piterbarg, L., and Rozovskii, B. Estimates of turbulence parameters from Lagrangian data using a stochastic particle model. *Journal of Marine Research*, 53(3): 371–401, May 1995.

Haller, G. *Lagrangian coherent structures*, volume 47. ETH Zürich, Zurich ZH,, Switzerland, Jan. 2015.

Haza, A. C., Poje, A. C., Özgökmen, T. M., and Martin, P. Relative dispersion from a high-resolution coastal model of the Adriatic Sea. *Ocean Modelling*, 22(1-2):48–65, 2008.

Haza, A. C., Özgökmen, T. M., Griffa, A., Garraffo, Z. D., and Piterbarg, L. Parameterization of particle transport at submesoscales in the Gulf Stream region using Lagrangian subgridscale models. *Ocean Modelling*, 42:31–49, Jan. 2012.

Haza, A. C., Özgökmen, T. M., Griffa, A., Poje, A. C., and Lelong, M. P. How does drifter position uncertainty affect ocean dispersion estimates? *Journal of Atmospheric and Oceanic Technology*, 31(12):2809–2828, 2014.

Haza, A. C., Özgökmen, T. M., and Hogan, P. Impact of submesoscales on surface material distribution in a gulf of Mexico mesoscale eddy. *Ocean Modelling*, 107:28–47, 2016.

Held, I. M., Pierrehumbert, R. T., Garner, S. T., and Swanson, K. L. Surface quasi-geostrophic dynamics. *Journal of Fluid Mechanics*, 282:1–20, 1995.

Horányi, A., Cardinali, C., and Centurioni, L. The global numerical weather prediction impact of mean-sea-level pressure observations from drifting buoys. *Quarterly Journal of the Royal Meteorological Society*, 143(703):974–985, Jan. 2017.

Hormann, V., Centurioni, L. R., and Reverdin, G. Evaluation of drifter salinities in the subtropical North Atlantic. *dx.doi.org*, 32(1):185–192, Jan. 2015.

Hormann, V., Centurioni, L. R., Mahadevan, A., Essink, S., D'Asaro, E. A., and Praveen Kumar, B. Variability of near-surface circulation and sea surface salinity observed from Lagrangian drifters in the northern Bay of Bengal during the waning 2015 southwest monsoon. *Oceanography*, 29(2):124–133, June 2016.

Hoskins, B. J. The mathematical theory of frontogenesis. *Annual Review of Fluid Mechanics*, 14(1):131–151, 1982.

Hoskins, B. J. and Bretherton, F. P. Atmospheric frontogenesis models: Mathematical formulation and solution. *Journal of the Atmospheric Sciences*, 29(1):11–37, 1972.

Jaeger, G. S. and Mahadevan, A. Submesoscale-selective compensation of fronts in a salinity-stratified ocean. *Science Advances*, 4(2):e1701504–, Feb. 2018.

Kawai, H. Scale dependence of divergence and vorticity of near-surface flows in the sea. *Journal of the Oceanographical Society of Japan*, 41(3):157–166, 1985.

Kirincich, A. The occurrence, drivers, and implications of submesoscale eddies on the Martha's Vineyard Inner Shelf. *Journal of Physical Oceanography*, 46(9):2645–2662, 2016.

Kirwan, A. D. Oceanic velocity gradients. *Journal of Physical Oceanography*, 5(4):729–735, Oct. 1975.

Kirwan, A. D., McNally, G. J., Reyna, E., and Merrell, W. J. The near-surface circulation of the eastern North Pacific. *Journal of Physical Oceanography*, 8(6):937–945, 1978.

Klein, P. and Lapeyre, G. The oceanic vertical pump induced by mesoscale and submesoscale turbulence. *Annual Review of Marine Science*, 1:351–375, Dec. 2009.

Klein, P., Hua, B. L., Lapeyre, G., Capet, X., Le Gentil, S., and Sasaki, H. Upper ocean turbulence from high-resolution 3d simulations. *Journal of Physical Oceanography*, 38(8): 1748–1763, Aug. 2008.

Koszalka, I., LaCasce, J. H., and Orvik, K. A. Relative dispersion in the Nordic Seas. *Journal of Marine Research*, 67(4):411–433, July 2009.

Kraichnan, R. H. Inertial ranges in two-dimensional turbulence. *Physics of Fluids*, 10(7): 1417, 1967.

LaCasce, J. Estimating eulerian energy spectra from drifters. *Fluids*, 1(4):33, Oct. 2016.

LaCasce, J. H. Statistics from Lagrangian observations. *Progress in Oceanography*, 77(1): 1–29, Apr. 2008.

LaCasce, J. H. Relative displacement probability distribution functions from balloons and drifters. *Journal of Marine Research*, 68(3):433–457, May 2010.

LaCasce, J. H. Surface quasigeostrophic solutions and baroclinic modes with exponential stratification. *Journal of Physical Oceanography*, 42(4):569–580, 2012. doi: 10.1175/JPO-D-11-0111.1.

LaCasce, J. H. and Bower, A. Relative dispersion in the subsurface North Atlantic. *Journal of Marine Research*, 58(6):863–894, Dec. 2000.

LaCasce, J. H. and Ohlmann, C. Relative dispersion at the surface of the Gulf of Mexico. *Journal of Marine Research*, 61(3):285–312, May 2003.

LaCasce, J. H. and Wang, J. Estimating subsurface velocities from surface fields with idealized stratification. *Journal of Physical Oceanography*, 45(9):2424–2435, 2015. doi: 10.1175/JPO-D-14-0206.1.

Lanotte, A. S., Corrado, R., Palatella, L., Pizzigalli, C., Schipa, I., and Santoleri, R. Effects of vertical shear in modelling horizontal oceanic dispersion. *Ocean Science*, 12(1):207–216, Feb. 2016.

Lapeyre, G. and Klein, P. Impact of the small-scale elongated filaments on the oceanic vertical pump. *Journal of Marine Research*, 64(6):835–851, Nov. 2006a.

Lapeyre, G. and Klein, P. Dynamics of the upper oceanic layers in terms of surface quasigeostrophy theory. *Journal of Physical Oceanography*, 2006b.

Le Traon, P. Y., Nadal, F., and Ducet, N. An improved mapping method of multisatellite altimeter data. *Journal of Atmospheric and Oceanic Technology*, 15(2):522–534, 1998.

Lin, J.-T. Relative dispersion in the enstrophy-cascading inertial range of homogeneous two-dimensional turbulence. *Journal of the Atmospheric Sciences*, 29(2):394–396, 1972.

Lindborg, E. A Helmholtz decomposition of structure functions and spectra calculated from aircraft data. *Journal of Fluid Mechanics*, 762, Dec. 2014.

Lucas, A. J., Shroyer, E. L., Wijesekera, H. W., Fernando, H. J. S., D'Asaro, E., Ravichandran, M., Jinadasa, S. U. P., MacKinnon, J. A., Nash, J. D., Sharma, R., Centurioni, L., Farrar, J. T., Weller, R., Pinkel, R., Mahadevan, A., Sengupta, D., and Tandon, A. Mixing to monsoons: Air-sea interactions in the Bay of Bengal. *EOS*, 95(30):269–270, Jan. 2014.

Lumpkin, R. and Elipot, S. Surface drifter pair spreading in the North Atlantic. *Journal of Geophysical Research*, 115(C12), Dec. 2010.

Lundgren, T. S. Turbulent pair dispersion and scalar diffusion. *Journal of Fluid Mechanics*, 111:27–57, Oct. 1981.

Mahadevan, A. The impact of submesoscale physics on primary productivity of plankton. *Annual Review of Marine Science*, 8(1):161–184, Jan. 2016.

Mahadevan, A. and Tandon, A. An analysis of mechanisms for submesoscale vertical motion at ocean fronts. *Ocean Modelling*, 14(3-4):241–256, Jan. 2006.

Mahadevan, A., Oliger, J., and Street, R. A nonhydrostatic mesoscale ocean model. Part I: Well-posedness and scaling. *Journal of Physical Oceanography*, 26(9):1868–1880, 1996a.

Mahadevan, A., Oliger, J., and Street, R. A nonhydrostatic mesoscale ocean model. Part II: Numerical implementation. *Journal of Physical Oceanography*, 26(9):1881–1900, Jan. 1996b.

Mahadevan, A., D'Asaro, E., Lee, C., and Perry, M. J. Eddy-driven stratification initiates North Atlantic spring phytoplankton blooms. *Science*, 337(6090):54–58, July 2012.

Maximenko, N., Lumpkin, R., and Centurioni, L. Ocean surface circulation. In *International Geophysics*, pages 283–304. Elsevier, Jan. 2013.

McWilliams, J. C. Submesoscale currents in the ocean. *Proceedings of the Royal Society A: Mathematical Physical and Engineering Sciences*, 472(2189):20160117, May 2016.

Meneveau, C. Lagrangian dynamics and models of the velocity gradient tensor in turbulent flows. *Annual Review of Fluid Mechanics*, 43(1):219–245, 2011.

Merrifield, S. T., Kelley, D. H., and Ouellette, N. T. Scale-dependent statistical geometry in two-dimensional flow. *Physical Review Letters*, 104(25):254501, June 2010.

Molemaker, M. J. and McWilliams, J. C. Baroclinic instability and loss of balance. *Journal of Physical Oceanography*, 2005.

Molinari, R. and Kirwan, A. D. Calculations of differential kinematic properties from Lagrangian observations in the western Caribbean sea. *Journal of Physical Oceanography*, 5(3):483–491, July 1975.

Morel, P. and Larceveque, M. Relative dispersion of constant–level balloons in the 200–mb general circulation. *Journal of the Atmospheric Sciences*, 31(8):2189–2196, 1974.

Munk, W., Armi, L., Fischer, K., and Zachariasen, F. Spirals on the sea. *Proceedings of the Royal Society A: Mathematical Physical and Engineering Sciences*, 456(1997):1217–1280, Jan. 2000.

Nastrom, G. D., Jasperson, W. H., and Gage, K. S. Horizontal spectra of atmospheric tracers measured during the global atmospheric sampling program. *Journal of Geophysical Research: Oceans (1978–2012)*, 91(D12):13201–13209, Nov. 1986.

Niiler, P. Chapter 4.1 The world ocean surface circulation. In *Ocean Circulation and Climate - Observing and Modelling the Global Ocean*, pages 193–204. Elsevier, 2001.

Niiler, P. P., Sybrandy, A. S., Bi, K., Poulain, P. M., and Bitterman, D. Measurements of the water-following capability of holey-sock and TRISTAR drifters. *Deep-Sea Research Part I*, 42(11-12):1951–1955, Jan. 1995.

Ohlmann, J. C., Molemaker, M. J., Baschek, B., Holt, B., Marmorino, G., and Smith, G. Drifter observations of submesoscale flow kinematics in the coastal ocean. *Geophysical Research Letters*, 44(1):330–337, 2017.

Okubo, A. Some remarks on the importance of the "shear effect" on horizontal diffusion. *Journal of the Oceanographical Society of Japan*, 24(2):60–69, 1968.

Okubo, A. Oceanic diffusion diagrams. *Deep Sea Research and Oceanographic Abstracts*, 18 (8):789–802, 1971.

Okubo, A. and Ebbesmeyer, C. C. Determination of vorticity, divergence, and deformation rates from analysis of drogue observations. *Deep Sea Research and Oceanographic Abstracts*, 23(4):349–352, Apr. 1976.

Omand, M. M., D'Asaro, E. A., Lee, C. M., Perry, M. J., Briggs, N., Cetinić, I., and Mahadevan, A. Eddy-driven subduction exports particulate organic carbon from the spring bloom. *Science*, 348(6231):222–225, Apr. 2015.

Paduan, J. D. and Niiler, P. P. A Lagrangian description of motion in Northern California coastal transition filaments. *Journal of Geophysical . . .* , 95(C10):18095–18109, 1990.

Pedlosky, J. *Geophysical Fluid Dynamics*. Springer New York, New York, NY, 1987.

Pineda, J., Hare, J. A., and Sponaugle, S. Larval transport and dispersal in the coastal ocean and consequences for population connectivity. *Oceanography*, 20(3):22–39, Sept. 2007.

Poje, A. C., Haza, A. C., Özgökmen, T. M., Magaldi, M. G., and Garraffo, Z. D. Resolution dependent relative dispersion statistics in a hierarchy of ocean models. *Ocean Modelling*, 31(1-2):36–50, 2010.

Poje, A. C., Özgökmen, T. M., Bruce Lipphardt, J., Haus, B. K., Ryan, E. H., Haza, A. C., Reniers, A. J. H. M., Olascoaga, J., Novelli, G., Beron-Vera, F. J., Chen, S., Mariano, A. J., Jacobs, G., Hogan, P., Coelho, E., A D Kirwan, J., Huntley, H., and Griffa, A. Submesoscale dispersion in the vicinity of the Deepwater Horizon spill. *arXiv.org*, (35): 12693–12698, July 2014.

Poje, A. C., Ã-zgökmen, T. M., Bogucki, D. J., and Kirwan, A. D. Evidence of a forward energy cascade and kolmogorov self-similarity in submesoscale ocean surface drifter observations. *Physics of Fluids*, 29(2):020701, Feb. 2017.

Pumir, A., Shraiman, B. I., and Chertkov, M. Geometry of Lagrangian dispersion in turbulence. *Physical Review Letters*, 85(25):5324–5327, Dec. 2000.

Ramachandran, S., Tandon, A., Mackinnon, J., Pinkel, R., Nash, J., Farrar, J. T., Lucas, A. J., Waterhouse, A. F., Shroyer, E., Mahadevan, A., and Weller, R. A. Submesoscale processes at shallow salinity fronts in the Bay of Bengal: Observations during the winter monsoon. *Journal of Physical Oceanography*, 48(3):479–509, Feb. 2018.

Richardson, L. F. Atmospheric diffusion shown on a distance-neighbour graph. *Proceedings of the Royal Society A: Mathematical Physical and Engineering Sciences*, 110(756):709–737, Apr. 1926.

Richardson, L. F. and Stommel, H. Note on eddy diffusion in the sea. *Journal of Atmospheric Sciences*, 5(5):238–240, Oct. 1948.

Rypina, I. I., Jayne, S. R., Yoshida, S., Macdonald, A. M., Douglass, E., and Buesseler, K. Short-term dispersal of Fukushima-derived radionuclides off Japan: modeling efforts and model-data intercomparison. *Biogeosciences*, 10(7):4973–4990, July 2013.

Rypina, I. I., Kirincich, A. R., Limeburner, R., and Udovydchenkov, I. A. Eulerian and Lagrangian correspondence of high-frequency radar and surface drifter data: Effects of radar resolution and flow components. *Journal of Atmospheric and Oceanic Technology*, 31 (4):945–966, 2014a. doi: 10.1175/JTECH-D-13-00146.1.

Rypina, I. I., Llopiz, J. K., Pratt, L. J., and Lozier, M. S. Dispersal pathways of American eel larvae from the Sargasso Sea. *Limnology and Oceanography*, 59(5):1704–1714, Aug. 2014b.

Rypina, I. I., Kirincich, A., Lentz, S., and Sundermeyer, M. Investigating the eddy diffusivity concept in the coastal ocean. *Journal of Physical Oceanography*, 46(7):2201–2218, 2016. doi: 10.1175/JPO-D-16-0020.1.

Sarkar, S., Pham, H. T., Ramachandran, S., Nash, J. D., Tandon, A., Buckley, J., Lotliker, A. A., and Omand, M. M. The interplay between submesoscale instabilities and turbulence in the surface layer of the Bay of Bengal. *Oceanography*, 29(2):146–157, 2016.

Saucier, W. Principles of meteorological analysis. Technical report, 1955.

Saucier, W. J. Horizontal deformation in atmospheric motion. *Eos, Transactions American Geophysical Union*, 34(5):709–719, Oct. 1953.

Scott, R. K. Local and nonlocal advection of a passive scalar. *Physics of Fluids (1994-present)*, 18(11):116601, Nov. 2006.

Shcherbina, A. Y., D'Asaro, E. A., Lee, C. M., Klymak, J. M., Molemaker, M. J., and McWilliams, J. C. Statistics of vertical vorticity, divergence, and strain in a developed submesoscale turbulence field. *Geophysical Research Letters*, 40(17):4706–4711, Sept. 2013.

Shroyer, E. L., Rudnick, D. L., Farrar, T., Lim, B., Venayagamoorthy, K., St Laurent, L. C., Garanaik, A., and Moum, J. N. Modification of upper-ocean temperature structure by subsurface mixing in the presence of strong salinity stratification. *Oceanography*, 29, June 2016.

Steinbuck, J. V., Koseff, J. R., Genin, A., Stacey, M. T., and Monismith, S. G. Horizontal dispersion of ocean tracers in internal wave shear. *Journal of Geophysical Research: Oceans (1978–2012)*, 116(C11):695, Nov. 2011.

Stone, P. H. Frontogenesis by horizontal wind deformation fields. *Journal of Atmospheric Sciences*, 23(5):455–465, Sept. 1966.

Sullivan, P. J. Some data on the distance-neighbour function for relative diffusion. *Journal of Fluid Mechanics*, 47(3):601?607, 1971.

Sundermeyer, M. A. and Ledwell, J. R. Lateral dispersion over the continental shelf: Analysis of dye release experiments. *Journal of Geophysical Research*, 106(C5):9603–9621, May 2001.

Swallow, J. C. The Aries current measurements in the western North Atlantic. *Philosophical Transactions of the Royal Society of London A: Mathematical, Physical and Engineering Sciences*, 270(1206):451–460, Nov. 1971.

Taylor, G. Dispersion of soluble matter in solvent flowing slowly through a tube. In *Proceedings of the Royal Society of London. Series A*, pages 186–203, Aug. 1953.

Thomas, L. N., Tandon, A., and Mahadevan, A. *Submesoscale Processes and Dynamics*, volume 177 of *Geophysical Monograph Series*. American Geophysical Union (AGU), Washington, D. C., 2008.

Thomson, W. On vortex atoms. *The London, Edinburgh, and Dublin Philosophical Magazine and Journal of Science*, 34(227):15–24, 1867.

Vallis, G. K. *Atmospheric and Oceanic Fluid Dynamics*. Cambridge University Press, Cambridge, U.K., 2006.

van Sebille, E., Griffies, S. M., Abernathey, R., Adams, T. P., Berloff, P., Biastoch, A., Blanke, B., Chassignet, E. P., Cheng, Y., Cotter, C. J., Deleersnijder, E., Döös, K., Drake, H. F., Drijfhout, S., Gary, S. F., Heemink, A. W., Kjellsson, J., Koszalka, I. M., Lange, M., Lique, C., MacGilchrist, G. A., Marsh, R., Mayorga Adame, C. G., McAdam, R., Nencioli, F., Paris, C. B., Piggott, M. D., Polton, J. A., Rühs, S., Shah, S. H. A. M., Thomas, M. D., Wang, J., Wolfram, P. J., Zanna, L., and Zika, J. D. Lagrangian ocean analysis: Fundamentals and practices. *Ocean Modelling*, 121:49–75, Jan. 2018.

Weller, R. A., Farrar, J. T., Buckley, J., Mathew, S., Venkatesan, R., Lekha, J. S., Chaudhuri, D., Kumar, N. S., and Kumar, B. P. Air-sea interaction in the Bay of Bengal. *Oceanography*, 29(2):28–37, 2016.

Wenegrat, J. O., Callies, J., and Thomas, L. N. Submesoscale baroclinic instability in the bottom boundary layer. *Journal of Physical Oceanography*, 0(0):null, 2018.

Wijesekera, H. W., Shroyer, E., Tandon, A., Ravichandran, M., Sengupta, D., Jinadasa, S. U. P., Fernando, H. J. S., Agrawal, N., Arulananthan, K., Bhat, G. S., Baumgartner, M., Buckley, J., Centurioni, L., Conry, P., Thomas Farrar, J., Gordon, A. L., Hormann, V., Jarosz, E., Jensen, T. G., Johnston, S., Lankhorst, M., Lee, C. M., Leo, L. S., Lozovatsky, I., Lucas, A. J., Mackinnon, J., Mahadevan, A., Nash, J., Omand, M. M., Pham, H., Pinkel, R., Rainville, L., Ramachandran, S., Rudnick, D. L., Sarkar, S., Send, U., Sharma, R., Simmons, H., Stafford, K. M., Laurent, L. S., Venayagamoorthy, K., Venkatesan, R., Teague, W. J., Wang, D. W., Waterhouse, A. F., Weller, R., and Whalen, C. B. ASIRI: An ocean-atmosphere initiative for Bay of Bengal. *Bulletin of the American Meteorological Society*, 97(10):1859–1884, Oct. 2016.

Young, W. R., Rhines, P. B., and Garrett, C. J. R. Shear-flow dispersion, internal waves and horizontal mixing in the ocean. *Journal of Physical Oceanography*, 12(6):515–527, June 1982.

Zhang, H. M., Reynolds, R. W., Lumpkin, R., Molinari, R., Arzayus, K., Smith, T. M., and Johnson, M. An integrated global observing system for sea surface temperature using satellites and in situ data: Research to operations. *Bulletin of the American Meteorological Society*, 90(1):31–38, Jan. 2009.